X-660-76-54

PREPRINT

NASA TM X- 71085

ON THE AGE OF COSMIC RAYS AS DERIVED FROM THE ABUNDANCE OF ^{10}Be

(NASA-TM-X-71085) ON THE AGE OF COSMIC RAYS AS DERIVED FROM THE ABUNDANCE OF Be-10 Ph.D. Thesis - Maryland Univ. (NASA) 200 p HC $7.50 CSCL 03B

N76-20058

Unclas

G3/93 22153

FRANK ANDREW HAGEN

MAR 1976
RECEIVED
NASA STI FACILITY
INPUT BRANCH

FEBRUARY 1976

GSFC

GODDARD SPACE FLIGHT CENTER
GREENBELT, MARYLAND

For information concerning availability
of this document contact:

Technical Information Division, Code 250
Goddard Space Flight Center
Greenbelt, Maryland 20771

(Telephone 301-982-4488)

"This paper presents the views of the author(s), and does not necessarily reflect the views of the Goddard Space Flight Center, or NASA."

ON THE AGE OF COSMIC RAYS AS DERIVED FROM THE ABUNDANCE OF ^{10}Be*

by
Frank Andrew Hagen

Dissertation submitted to the Faculty of the Graduate School
of the University of Maryland in partial fulfillment
of the requirements for the degree of
Doctor of Philosophy
1976

*Supported in part by NASA Grant NGL21-002-033

APPROVAL SHEET

Title of Thesis: On the Age of Cosmic Rays as Derived from the Abundance of ^{10}Be

Name of Candidate: Frank Andrew Hagen
Doctor of Philosophy, 1976

Thesis and Abstract Approved: Frank B. McDonald

Dr. Frank B. McDonald
Professor
Physics and Astronomy

Date Approved:

VITA

ORIGINAL PAGE IS
OF POOR QUALITY

Name: Frank Andrew Hagen.

Permanent address: 1102 South 120th Street, Tacoma, Washington 98444

Degree and date to be conferred: Ph.D., 1976

Date of birth: [redacted]

Place of birth: [redacted]

Secondary education: Franklin Pierce High School,
Tacoma, Washington, 1965.

Collegiate institutions attended	Dates	Degree	Date of Degree
Pacific Lutheran University	1965-1969	B.S.	1969
University of Maryland	1969-1974	M.S.	1974
University of Maryland	1974-1976	Ph.D.	1976

Major: Astrophysics.

Minor: General Physics.

Publications: Hagen, F. A., and Tang, K. T., "Index of Refraction and Verdet Constant of Atomic Helium", 1970, J. Opt. Soc. Am. 60, 365.

Crannell, C. J., Gearhart, R. A., Hagen, F. A., Jones, W. V., Kurz, R. J., Ormes, J. F., Price, R. D., Silverberg, R. F., and Simnett, G. M., "Electron Calibration of a High-Energy Cosmic Ray Detector", 1973, Nucl. Instr. and Meth. 108, 445.

Maehl, R. C., Fisher, A. J., Hagen, F. A., and Ormes, J. F., "Neutron-Rich Isotopes of Cosmic Rays with $9 \leq Z \leq 16$", 1975, Ap. J. 202, L119.

Fisher, A. J., Hagen, F. A., Maehl, R. C., Ormes, J. F., and Arens, J. F., "The Isotopic Composition of Cosmic Rays with $5 \leq Z \leq 26$", 1976, Ap. J. 205, in press.

Positions held: Teaching Assistant, University of Maryland 1969-1970.

Research Assistant, University of Maryland 1970-1976.

ORIGINAL PAGE IS
OF POOR QUALITY

ABSTRACT

Title of Thesis: On the Age of Cosmic Rays as Derived from the Abundance of ^{10}Be

Frank A. Hagen, Doctor of Philosophy, 1976

Thesis directed by: Frank B. McDonald
Professor
Physics and Astronomy

The isotopic composition of cosmic ray Be, B, C and N has been studied using a new range versus total light technique. Special emphasis has been placed on the Be isotopes and, in particular, on the radioactive isotope ^{10}Be whose mean lifetime against decay ($\tau_d = 2.2 \times 10^6$ yr) makes it an ideal "clock" with which to measure the cosmic-ray age. The experiment consisted of a thin trigger scintillator, an acrylic plastic Cerenkov detector and a spark chamber, followed by a totally active stack of 14 scintillation detectors. This stack of scintillators made possible the measurement of range, and also permitted the removal of interacting events by continuously monitering their identities along their trajectories through the experiment. The experiment was carried by balloon to atmospheric depths ranging from 3.5 to 5.0 g cm^{-2} residual atmosphere for a total exposure time of 23 hr. The flight was carried out on August 15, 1973, from Thompson, Canada.

Both the theoretical and empirical response of the experiment have been considered in detail. The data have been corrected for variations in detector response as a function of position and time, and also for variations in detector thicknesses. The mass resolution achieved by the experiment is given by $\sigma_A = 0.047A$. Comparisons are made with the results of other experiments after correcting the data for interactions in the detector, the varying energy windows (roughly 150 to 450 MeV/nuc) in

which the experiment is sensitive to different isotopes, and production and destruction of nuclei in nuclear interactions in the atmosphere above the experiment. In addition, the data have been corrected for the effects of solar modulation before being compared with model predictions.

The data have been interpreted within the framework of the "leaky box" model of cosmic-ray propagation, where the cosmic rays are imagined to propagate freely within a box (e.g. the galactic disk) from which they have only a small probability of escape each time they hit a wall. The results indicate the survival of (55 $\pm$21) % of the ^{10}Be in the arriving cosmic rays. In the leaky box model, this is interpreted in terms of a mean cosmic-ray confinement time given by $\tau_e = 5^{+6}_{-3} \times 10^6$ yr, which corresponds to a mean density, $n = 0.7^{+1.0}_{-0.4}$ atoms cm^{-3}, of matter in the confinement volume. This result is apparently most consistent with the confinement of the cosmic rays to the galactic disk.

ACKNOWLEDGMENTS

I am of course indebted to many individuals for their contributions to the completion of this thesis. Thanks are especially due to Dr. F. B. McDonald, Chief of the Laboratory for High Energy Astrophysics at Goddard Space Flight Center, who served as my thesis advisor and provided me the opportunity to conduct this research. He has also offered many valuable comments during the preparation of the manuscript.

Dr. J. F. Ormes has been invaluable for suggesting the topic of the research, and for his constant encouragement, guidance and advice while it was being carried out. I am also indebted to Dr. A. J. Fisher, with whom the majority of this work was shared. This thesis could not have been successfully completed without the contributions of these two individuals. Others whose comments and suggestions have been of considerable assistance include Dr. V. K. Balasubrahmanyan, Dr. R. C. Maehl, Dr. J. F. Arens, and Dr. L. A. Fisk. I would also like to thank Dr. R. F. Silverberg and Dr. C. J. Crannell for their assistance at the beginning of my graduate career at the Laboratory.

J. Laws is to be thanked for his contributions to the engineering, design and checkout of the experiment. R. Greer, M. Powers, G. Cooper and L. Stonebreaker have contributed greatly in the assembly, checkout and flight phases of the experiment. J. Purvis digitized the data while C. Weikel and A. Chatterjee have done much of the basic programming associated with the experiment. A. Thompson, H. Trexel, F. Shaffer and L. White have contributed drafting support of all kinds and are to be thanked both for the quality of their work and their patience in doing it. Finally, I am indebted to S. Shrader for her patience in preparing the drafts and manuscripts for this thesis. Her experience and suggestions

have saved considerable time and effort.

I owe a great deal to my parents, who have never relented in their optimism and encouragement. I also owe a great deal to my wife, Amy, who has endured much on account of this work, and given nothing but encouragement in return.

TABLE OF CONTENTS

Chapter	Page
ACKNOWLEDGEMENTS	ii
LIST OF TABLES	vii
LIST OF FIGURES	ix
I. INTRODUCTION	1
A. The Cosmic Ray Source	3
B. Acceleration	6
C. Propagation	9
II. TECHNIQUES FOR THE MEASUREMENT OF MASS	13
A. The Development of Experimental Techniques	13
1. Basic Detectors	13
2. $\frac{dE}{dx}$	14
3. $\frac{dE}{dx}$ x C	14
4. $\frac{dE}{dx}$ x E	14
5. Magnetic Spectrometers	16
6. Trajectory Definition	16
B. The Measurement of Mass	17
1. Energy	17
2. Rate of Energy Loss to Ionization	20
3. Range	22
4. Rigidity	22
5. Cerenkov Radiation	25
6. Mass Determination	25
7. Resolution	31
C. The Experiment	37
1. Specialization to ExR	37

Chapter Page

2. Range Resolution. 40

3. Scintillator Saturation 42

4. Additional Considerations 42

5. Description of Experiment 43

a. Overview. 43

b. Testing and Checkout of Detectors 45

c. Detailed Description of Detectors 47

d. Light Pipes 49

e. Coincidence Requirements. 49

f. Pulse Height Analysis 50

6. Flight. 53

III. DATA ANALYSIS 55

A. Formulation of Response 55

B. Preliminary Selections. 58

C. R x L Mode of Analysis. 61

1. Estimation of Range 62

2. Standard Curves 67

3. Mass Determination. 71

4. Rejection of Background 75

5. Observed Isotopic Composition 77

D. Consideration of Mass Resolution. 84

1. Contributing Factors. 84

2. Analytical Analysis of Resolution 87

3. Empirical Consideration of Resolution 91

E. Corrections to the Data 92

1. Interactions. 92

Chapter Page

2. Energy Corrections. 95

3. Atmospheric Corrections 97

4. Demodulation Corrections. 108

F. Discussion of Results 112

G. Comparisons with Other Experiments. 113

IV. DISCUSSION OF RESULTS 119

A. The Diffusion Model 119

1. Halo Model. 119

2. Disk Model. 121

B. The Leaky Box Approximation 123

1. Pathlength. 128

2. Lifetime. 133

C. Conclusions 139

APPENDIX A. DETECTOR CALIBRATION. 146

1. Gain Change Factors 146

2. Detector Nonlinearities 153

3. Detector Normalization. 153

4. Positional and Temporal Nonuniformities 160

5. Detector Thicknesses. 168

APPENDIX B. DEFINITIONS OF SYMBOLS USED IN THIS THESIS. 170

REFERENCES 176

LIST OF TABLES

Table		Page
II.1.	Results of various possible two parameter analyses based on observations of the energy, ionization energy loss, range and/or rigidity of a ^{10}Be event with velocity $\beta = 0.5$.	29
II.2.	Resolution required in observation of energy, ionization energy loss, range and/or rigidity in order to expect a valley between ^{9}Be and ^{10}Be (abundances assumed in ratio 2:1) in various two parameter analyses	38
II.3.	Descriptions of detectors and their performance.	46
II.4.	Triggering thresholds for the experiment (in channel numbers)	52
III.1.	Response of various detectors (x minimum units) to relativistic particles as a function of charge	63
III.2.	Best fit parameters resulting from maximum likelihood analysis of mass distributions	81
III.3.	Correction factors applied to the data	94
III.4.	Correction factors applied to the semiempirical formula for partial cross sections (Silberberg et al. 1973) as derived from measurements of Lindstrom et al. (1975a) for ^{12}C and ^{16}O primaries	98
III.5.	Stability selections for atmospheric propagation	103
III.6.	Isotopic abundances at the detector and as extrapolated to the top of the atmosphere	104
III.7.	Atmospheric contributions to observed ^{10}Be	107
III.8.	Comparisons with other experiments	114
IV.1.	Stability selections for interstellar propagation. . . .	132
IV.2.	Best values of λ_e as derived from condition that source abundances of various isotopes vanish in a leaky box propagation model.	134
IV.3.	Isotopic abundances in the arriving cosmic rays as predicted by a leaky box model under various assumptions regarding propagation energy, pathlength, composition of interstellar medium and input cross sections	137

Table | Page

A.1. Gain change factors. 147

A.2. Detector thicknesses measured at their corners 169

LIST OF FIGURES

Figure		Page
II.1.	The energy of a proton and its velocity derivative as functions of velocity	19
II.2.	The ionization energy loss by a proton and its velocity derivative as functions of velocity	21
II.3.	The range of a proton and its velocity derivative as functions of velocity	23
II.4.	The rigidity of a proton and its velocity derivative as functions of velocity.	24
II.5.	The emission of Cerenkov radiation by a proton and its velocity derivative as functions of velocity . . .	26
II.6.	Mass as a function of assumed velocity derived from measurement of energy, ionization energy loss or range of a ^{10}Be with velocity $\beta = 0.5$.	28
II.7.	Resolution as a function of extrema locations for a bi-gaussian distribution with amplitude ratio $k = 2$. Values of the distribution function at the extrema are also indicated	33
II.8.	Critical resolution required for the appearance of a valley in a bi-gaussian distribution as a function of amplitude ratio	34
II.9.	Energy versus range for protons.	39
II.10.	Schematic diagram of the experiment.	44
II.11.	Schematic illustration of triggering logic used for the experiment	51
II.12.	Pulse height analysis strategy for detectors D7-14 . .	54
III.1.	Elemental abundances from Cerenkov versus scintillator analysis.	60
III.2.	Schematic illustration of range versus total light analysis	64
III.3.	Rotated light versus range plot for particles stopping near detector boundaries.	66

Figure		Page
III.4.	Range in the last detector as determined from last three detectors (last two considered as one) versus that determined from last two detectors penetrated	68
III.5.	Rotated light versus range plot for unselected data with standard response curves sketched in	69
III.6.	Integral and differential saturation as functions of velocity as derived from standard response curves	72
III.7.	Distribution of mass variance for Be events.	76
III.8.	Rotated light versus range plot for selected data. . .	78
III.9.	Mass histograms for data accepted and rejected by mass variance criterion. Maximum likelihood fits to accepted data are also indicated.	79
III.10.	Mass resolution (as derived from maximum likelihood fits) as a function of mass.	83
III.11.	Contributions to the experimental uncertainties. . . .	85
III.12.	Mass variance distributions (both uncorrected and corrected for assumed A^2 scaling) for Be events with $A > 8$ as compared to Be events with $A < 8$	93
III.13.	Distribution of atmospheric slant depths	101
III.14.	Isotopic abundances relative to carbon as a function of depth in a slab model atmosphere.	106
IV.1.	Isotopic abundances at the cosmic-ray source relative to carbon as a function of mean leakage pathlength, λ_e, assumed.	131
IV.2.	Mean leakage pathlength, λ_e, as derived from condition that source abundances of various isotopes vanish.	135
IV.3.	Matter density in cosmic-ray confinement volume as a function of mean escape pathlength	140
IV.4.	Mean lifetime against escape for cosmic rays as a function of mean pathlength for escape	141
A.1.	Typical gain change calibration plot: H'_{71} versus H'_{72}.	150

Figure | Page

A.2. Noisy gain change calibration plot: H_{92} versus H'_{93} 151

A.3. Representative calibration of nonlinearity of a 256 channel analyzer with a pulser 154

A.4. Unmapped Cerenkov versus scintillator plot 157

A.5. Absolute calibration of D4 159

A.6. Contour plot of D1 response to carbon. 162

A.7. Contour plot of D1 map, M_1^P, fitted to data of figure A.6 163

A.8. Cerenkov versus scintillator plot for mapped data. This should be compared to figure A.4. 164

A.9. Linear correlation of drift functions M_1^T and M_7^T. . . . 166

A.10. M_1^T and temperature as functions of time. 167

CHAPTER I

INTRODUCTION

As understood at the present time, the cosmic radiation contains electrons, protons and heavier nuclei from throughout the periodic table, with energies ranging from the suprathermal to over a billion times what can be achieved using currently available accelerators. In the course of their nucleosynthesis, acceleration and propagation through space, these particles must certainly have participated in very high energy processes of various kinds, and therefore carry significant information characterizing these processes. The cosmic rays fill the galaxy to an energy density ~ 1 eV cm^{-3}, which is comparable to that residing in visible light, the 3°K background radiation and the galactic magnetic fields. It follows that these particles must play an important role in the dynamic structure of the galaxy (Parker 1965, Badhwar et al. 1975). It is then of considerable interest to determine where the cosmic rays reside: whether they are confined predominantly to the galactic disk (Owens 1975, Dickinson et al. 1975), or perhaps fill a roughly spherical galactic "halo" surrounding the disk (Ginzburg et al. 1964, Suh 1974). The possibility has even been suggested that the cosmic radiation may fill some extended region of extragalactic space (Setti et al. 1972, Brecher et al. 1971, Sitte 1972).

Of the various observable features of the cosmic radiation--composition, energy spectra, temporal variations, and directional and positional anisotropies--the study of composition is perhaps the most promising for answering questions such as those posed above. For example, studies of the charge composition have revealed the presence of significant abundances of components (e.g. Li, Be and B) thought to be totally absent from

the cosmic-ray source. Such components must originate entirely in the nuclear spallation of heavier species. Thus the abundances of these species depend only on the amount of matter traversed by the primary cosmic-ray "beam". This leads to the conclusion that the cosmic rays have, on the average, traversed

$$\lambda_e = \langle m \rangle n v \tau_e \simeq 5 \ g\,cm^{-2} \tag{I.1}$$

of material. Here $\langle m \rangle$ is the mean atomic mass of the material (gas) in the region where the cosmic rays propagate, n is the number density of atoms, v is their propagation velocity ($v \sim c$ is usually a good approximation) and τ_e is the mean propagation time corresponding to λ_e.

However, a knowledge of λ_e does not answer the question of where the cosmic rays reside (i.e. in the galactic disk, a galactic "halo", or extragalactic space). One parameter which is highly sensitive to the confinement region, however, is the number density of atoms, n: $n \sim 1$ for the galactic disk, $n \sim 10^{-2}$ for the galactic "halo", and $n \sim 10^{-5}$ for the intergalactic medium. Since λ_e is known, however, the determination of n and τ_e are equivalent. As was first suggested nearly two decades ago by Hayakawa et al. (1958) and later emphasized by Peters (1963), this may be accomplished by a measurement of the abundance of the radioactive "clock" isotope ^{10}Be.

A direct experimental measurement of the abundance of ^{10}Be in the cosmic rays has long been delayed due both to the experimental problem of obtaining isotopic resolution and the rarity of ^{10}Be relative to its neighbors. Attempts have been made in the meantime to approach the problem indirectly by the measurement of the charge ratio $\frac{Be}{B}$ (Shapiro et al. 1968, 1969; O'Dell et al. 1975). These attempts have suffered

from the rarity of ^{10}Be with respect to the other isotopes of Be, in conjunction with the limited precision with which it is possible to calculate this ratio from theory in the cases of interest (i.e. the survival or decay of ^{10}Be). The first attempt at a direct measurement of the ^{10}Be abundance was by the University of New Hampshire group (Webber et al. 1973) using a balloon experiment floating at an atmospheric depth of ~ 3 g cm^{-2}. This group has also recently reported results of a new, improved experiment (Preszler et al. 1975). Satellite observations taken outside the earth's atmosphere and magnetosphere have also recently been reported by the University of Chicago group (Garcia-Munoz et al. 1975, 1975a). The objective of the present thesis is to supplement and improve upon the above results by a measurement of the isotopic abundances of cosmic ray Be, B, C and N, with the primary objective of determining the cosmic-ray age by a measurement of the ratio $\frac{^{10}Be}{Be}$.

Before discussing in detail the experiment and its results, it is desirable to sketch briefly our present understanding of the cosmic rays and the various theoretical models, particularly as these relate to studies of the composition of the cosmic radiation. The discussion is organized into three major parts following the temporal history of the particles: the nature of the cosmic-ray source (or nucleosynthesis), the nature of the acceleration to cosmic-ray energies, and the nature of the propagation of the cosmic rays through space. With respect to each of these topics, we may inquire of the mechanism of the process, and its location in space and time.

A. The Cosmic Ray Source

Because of both the ultra high energies of individual cosmic-ray particles and the energy content of the cosmic radiation as a whole, the

cosmic-ray source has at one time or another been attributed to virtually every violent phenomenon known or postulated to occur in the universe. The earth, thunderstorms, the sun, magnetic white dwarfs, supernovae, pulsars, explosions of the galactic center, radio galaxies, quasars, and even the big bang itself have all been suggested at one time or another as cosmic-ray sources. Clearly, there is a strong need for experimental observations capable of restricting the options available to the theorists in constructing models.

For example, the radio and optical emission of supernova remnants have been explained in terms of the synchrotron emission of electrons in magnetic fields (Ginzburg et al. 1964). For the particular case of the Crab supernova remnant, the emitting electrons are estimated to have energies as high as $\sim 5 \times 10^{11}$ eV. Because of their overwhelming rate of energy loss by synchrotron emission, these electrons could not have been accelerated more than $\sim$ 100 years ago. This is independent of their initial energy and far less than the age of the supernova, which was observed in the year 1054. Thus electrons are even now being accelerated to cosmic-ray energies in the Crab nebula. Accepting the rather uncertain hypothesis that the Crab nebula is a "typical" supernova remnant, and assuming that $\sim$ 100 times the energy going into the acceleration of electrons goes into the acceleration of protons and heavier nuclei (which is the ratio observed locally in the cosmic rays), one may estimate the rate at which cosmic rays are being contributed to the galaxy by supernovae (Ginzburg et al. 1964). In particular, it is conceivable that a typical supernova dissipates $\sim 10^{50}$ erg in cosmic rays, which gives an average power of $\sim 3 \times 10^{40}$ erg sec^{-1} if the frequency of supernovae is taken as one per hundred years. On the other hand, the ratio

of the volume in which cosmic rays are confined to their mean confinement time, $\frac{V}{\tau_e} \sim 10^{52}$ $cm^3 sec^{-1}$, is characteristic of most cosmic-ray propagation models which confine the cosmic rays to the galaxy. For example, in the halo model of Ginzburg (1964), the halo volume is $V \sim 2 \times 10^{68}$ cm^3, and the mean confinement time is $\tau_e \sim 3 \times 10^8$ yr. Assuming that the observed cosmic-ray energy density of ~ 1 eV cm^{-3} is constant in time (which seems to have been the case for at least the last billion years; Van Loon 1973), we then estimate the power required of the cosmic-ray sources to be $\sim 10^{40}$ erg sec^{-1}. This is in agreement with the above estimate of the power available from supernovae to within the accuracy of the numbers used.

Such energy considerations have served to make supernovae and supernova remnants attractive sites for the acceleration of the predominant portion of the cosmic rays. This would not rule out contributions from other sources, and indeed there may well exist a hierarchy of different types of sources both in our own galaxy and in others. Finally, we note that this result is dependent upon the existence of an efficient means of confining the cosmic rays to the galaxy, and thus retarding the rate of energy loss due to escaping particles.

The characteristics of the cosmic-ray source can be probed by observations of the composition of the cosmic rays, as extrapolated to the source in terms of some convenient propagation model. For example, observations of the very heavy ($Z \geqslant 30$) component are apparently somewhat suggestive of an r-process (as opposed to s-process) origin (Price et al. 1975). Since the r-process can only take place in an extremely hot environment with high density of neutrons present, this supports a model wherein the nucleosynthesis of the cosmic rays occurs in a

supernova explosion. The r-process does not (for example) occur as one of the normal cycles of nucleosynthesis in a stable star. Attempts have been made (with some degree of success) to calculate the observed cosmic-ray composition from models based on explosive nucleosynthesis (Hainebach et al. 1975), which is a strong possibility as a mechanism for supernova explosions (Arnett 1969, Truran et al. 1970). Such models have a number of free parameters, some of which may possibly be determined or considerably constrained by observations of the isotopic composition of the cosmic rays. For example, one such parameter is the neutron excess present in the source, which is strongly correlated to the abundances of ^{54}Fe and ^{58}Fe relative to ^{56}Fe. Another parameter, the temperature at which the nucleosynthesis occurs, would be reflected in the relative importance of various contributing nucleosynthesis chains, such as the explosive burning of C, O and Si, the CNO cycle, and so on. Each of these cycles produces certain characteristic isotopes, the observation of which would thus help to establish the temperature prevailing in the cosmic-ray source.

B. Acceleration

In the following section, the acceleration of particles to cosmic-ray energies is discussed. Features of the acceleration which may be reflected in the composition of the cosmic rays are of particular interest. For these purposes, a detailed discussion of the physics behind the acceleration is often not required, and therefore will not be given here. Features which are of interest include the nature of the reservoir from which particles are accelerated, and how they are selected for acceleration.

As suggested in the preceding section, supernova remnants are prime candidates for the cosmic-ray source. Furthermore, there is

evidence that the acceleration of cosmic rays is an ongoing process in supernova remnants (in particular, the Crab). A potential means for accelerating these particles was provided by the discovery of pulsars (Hewish et al. 1968)--one of which happens to be located in the Crab nebula--and their interpretation as rapidly spinning neutron stars formed in supernova explosions (Gold 1968). The acceleration mechanism would be provided by the enormous magnetic fields of $\sim 10^{12}$ gauss associated with these objects. This is supported by the observation that the Crab pulsar is losing energy (as estimated from its angular deceleration) at a rate essentially equal to that going into the acceleration of particles to relativistic energies (again assuming that $\sim$ 100 times as much energy goes into protons and nuclei as electrons; Pacini 1973).

It is implicit in all of the above that there may well be a substantial time delay between the origin (or nucleosynthesis) of the cosmic rays and their acceleration to relativistic energies. Specifically, the nucleosynthesis would most likely take place in the supernova explosion itself, while the acceleration appears to be a continuing process which might (for example) be directly attributed to the pulsar formed in the supernova explosion (e.g. see Gold 1968, Goldreich et al. 1969, Gunn et al. 1971), or might (on the other hand) be due to the action of rapidly moving magnetic clouds in the remnant (Ramadurai et al. 1972, Scott et al. 1975). Such acceleration would presumably occur after some degree of mixing of the debris from the explosion with the interstellar medium, which would be reflected in the cosmic-ray composition (Reeves 1973). The existence of a time delay between the nucleosynthesis and acceleration of the cosmic rays can be tested by measurements of the abundances of certain isotopes (e.g. ^{57}Co and ^{44}Ti) which decay exclusively by

electron capture, and are presumed to be produced by the cosmic-ray source (Shapiro et al. 1975, Soutoul et al. 1975). At rest, these isotopes are neutral and will decay at characteristic rates. Once accelerated, however, they are stripped of all their atomic electrons and thus become stable. We thus have radioactive clocks which are turned on at the time of nucleosynthesis and conveniently turned off when the actual acceleration occurs. Although isotopes which decay exclusively by electron capture are best for these purposes, it is possible that one may also use isotopes with alternate modes of decay (e.g. ^{56}Ni and ^{59}Ni), provided the alternate lifetime is sufficiently long (i.e. $\gtrsim$ a few million years, depending upon one's model for propagation) to ensure their survival in the cosmic rays.

Models have also been proposed in which the acceleration occurs virtually at the same time as the nucleosynthesis, i.e. by relativistic shock waves generated by the supernova explosion (Colgate 1969). However, such models suffer from a number of difficulties. One questions, for example, the survival of the heavy nuclei in the extreme environment of a relativistic shock wave. It also appears inevitable that the intense streaming of the cosmic rays away from their source when created in such intense bursts will set up self-generated magnetohydrodynamic waves (Wenzel 1973). These waves then serve to efficiently absorb energy by scattering the cosmic rays. Such a result implies that the cosmic rays would escape with at most a few percent of their original energy. This drastically increases the power requirements on the cosmic-ray sources, probably to unacceptable levels. Also, the dissipated energy would heat the interstellar medium, again to a degree which may well be unacceptable (Wenzel 1973).

The remarkable resemblence of cosmic-ray abundances to those characterizing the solar system (which may also be explained, in large part, by models based on explosive nucleosynthesis) has been noted essentially from the first observation of the nuclear component (Bradt et al. 1950). The correlation is considerably enhanced by taking account of ionization cross sections (Casse et al. 1975), which suggests that the cosmic rays may result from the selective acceleration of material characterized by essentially solar system abundances. The selection mechanism would be ionization--i.e. only ionized atoms are accelerated. Such a model would, of course, predict no anamalous enhancements or deficiencies of specific isotopes as compared to other isotopes of a given element, as the ionization cross sections are all the same. This line of reasoning can thus be easily tested by measurements of the isotopic composition of the cosmic rays.

C. Propagation

Having discussed the origin and acceleration of the cosmic rays, one still needs to consider their propagation in interstellar space before being able to make comparisons with experimental observations. Most current models for the propagation of cosmic rays are based on the diffusion model originally proposed by Ginzburg et al. (1964). Although cosmic rays are constrained to closely follow magnetic field lines in this model, they may be scattered back and forth along the lines by irregularities in the lines. Furthermore, the actual orientation of the field lines in space is considered sufficiently random that a small drift (or scattering) of a particle across the field lines effectively randomizes its trajectory through space. Thus the propagation has been approximated as a diffusive process, with the actual diffusion coefficient

used left as a free parameter to be adjusted (within limits) for the optimum agreement with observations.

If the characteristic pathlength required for a particle to escape in a diffusion model is much greater than the typical dimensions of the confinement region, then the diffusion model may be quite well approximated by a "leaky box" model (Jones 1970, Owens 1975a). In this model, the boundaries of the confinement region are pictured as the sides of a "leaky" box, which have a high efficiency for reflecting particles back into the box. The fundamental parameter in such a model is the probability of leaking out of the box. This is given by the leakage pathlength, λ_e, which is related to the mean time for escape from the box, τ_e, by equation I.1. If there are radioactive isotopes of mean decay time $\tau_d \sim \tau_e$ involved in the problem, then the model also becomes directly sensitive to the mean escape time, τ_e, and thus to the number density, n, of atoms in the box. The parameter λ_e can be determined if we assume that certain components of the locally observed cosmic rays are absent in the source. Their origin must then be entirely in the fragmentation of heavier species in the interstellar medium, a process which can easily be modeled. For example, Li, Be and B are all easily destroyed in hot stellar interiors, and for this reason are thought to be absent in the cosmic-ray sources. A calculation based on these elements gives $\lambda_e \simeq 5$ g cm^{-2} (Shapiro et al. 1973). Assuming a density $n \sim 1$ hydrogen atom cm^{-3} in the confinement volume (which would be consistent with confinement of the cosmic rays to the galactic disk) we then obtain $\tau_e \simeq 3 \times 10^6$ yr. from equation I.1. Alternatively, we may adopt a "halo" model in which the cosmic rays are confined to a quasi-spherical volume surrounding the galactic disk. In this case the gas

density ($n \cong 10^{-2} cm^{-3}$) is much lower than for the disk, so that a much longer escape time (i.e. $\tau_e \cong 3 \times 10^8$ yr) is required for consistency with the observed leakage pathlength. It is thus apparent that an experimental determination of the mean escape time, τ_e, would be a sensitive test for discriminating between these models.

As has already been pointed out, an experimental determination of the mean escape time, τ_e, is possible by a measurement of the abundance of a radioactive isotope which is completely secondary in origin (i.e. absent from the cosmic-ray source), and also has an appropriately long mean lifetime against decay (i.e. $\tau_d \sim \tau_e$). Several such isotopes have been suggested, including ^{10}Be ($\tau_d = 2.2 \times 10^6$ yr), ^{26}Al ($\tau_d = 1.2 \times 10^6$ yr) and ^{36}Cl ($\tau_d = 4 \times 10^6$ yr); in extreme cases even the isotope ^{40}K ($\tau_d = 1.9 \times 10^9$ yr) may be of use. Most attention so far has been focused on ^{10}Be because of its clear secondary origin, its nearly ideal lifetime (for a disk confinement model), and also because it is experimentally the most accessible. The experimental problem of separating ^{10}Be (especially from the more abundant neighboring isotope ^9Be) is still very difficult, however. For this reason, most of the effort so far has been concentrated on the indirect approach of measuring the charge ratio $\frac{Be}{B}$ (Shapiro et al. 1968, 1969; O'Dell et al. 1975). Since ^{10}Be decays to ^{10}B, this charge ratio is the most sensitive of any to the question of the survival of ^{10}Be in the cosmic rays. The precision obtainable by this approach suffers greatly from the very low abundance of ^{10}Be relative to the other Be isotopes, in conjunction with the limited precision of the theoretical predictions which can be made. Nevertheless, the analysis has been performed, with results which are most consistent with the complete survival of ^{10}Be in cosmic rays of energy $E \geqslant 1$ GeV/nuc

(Shapiro et al. 1968, 1969; O'Dell et al. 1975). The first attempt to directly measure the abundance of ^{10}Be in the cosmic rays was by Webber et al. (1973), who used a balloon borne experiment floating beneath a residual layer of ~ 3 g cm^{-2} of atmosphere. This group has also recently reported results on a new, improved experiment (Preszler et al. 1975). The only other published results are those of Garcia-Munoz et al. (1975, 1975a), who report results from the IMP 7 and IMP 8 satellites. While Garcia-Munoz et al. feel their results are consistent with the complete decay of ^{10}Be (i.e. a very long leakage lifetime), the results of Webber et al. appear to indicate the survival of a significant fraction of the ^{10}Be.

It is the objective of the current thesis to supplement and extend the above results by a measurement of the isotopic abundances of the elements Be, B, C and N, with special emphasis on the question of the degree to which ^{10}Be survives in the cosmic rays. Our results indicate the partial survival of ^{10}Be, and result in the estimate $\tau_e = 5^{+6}_{-3} \times 10^6$ yr for the mean escape time of cosmic rays. This is entirely consistent with models which confine the cosmic rays to the galactic disk. It is not consistent with models in which the cosmic rays are confined to a spherical halo region, but may be consistent with a hybrid model in which the cosmic rays are confined to a considerably flattened halo region surrounding the galactic disk.

CHAPTER II

TECHNIQUES FOR THE MEASUREMENT OF MASS

A. The Development of Experimental Techniques

Before discussing in detail the general problem of determining the mass of a cosmic-ray particle (section B), and the specific experimental approach of this thesis (section C), a brief description will first be given of the development of our knowledge of the composition (chemical and isotopic) of the cosmic radiation. We begin with the discovery of the existence of a significant component consisting of nuclei heavier than protons (Frier et al. 1948), which followed closely upon the association of the predominant component with protons by its highly penetrating nature (Schein et al. 1941) and positive charge (Johnson 1933, Alvarez et al. 1933, Rossi 1934). Although the existence of a heavy component was soon confirmed by a number of other experiments (e.g. see Singer 1958 and references therein), it was to be a decade before experimental resolution was improved to the point where a consensus began to emerge on the detailed charge composition of the cosmic rays. In particular, there were significant discrepancies in the measured abundances of the elements Li, Be and B as well as the odd Z nuclei (e.g. N, F, Na, Al and P), which tend to have abundances considerably reduced from those of their even Z neighbors. At the present time, experimental techniques have improved considerably, to the point where excellent charge resolution has been obtained by groups working at several laboratories for elements with $Z \leq 26$.

1. <u>Basic Detectors</u>. From the beginning, there has been a wide variety of detection schemes applied to the study of the cosmic-ray

composition. These have included both passive detectors (e.g. emulsions and plastics) and active detectors (e.g. cloud chambers, spark chambers, proportional counters, scintillators and solid state detectors). Although the passive detectors dominated at first, rapid improvements in the resolution and areas of the various active detectors enabled them to overtake the passive detectors.

2. $\underline{\frac{dE}{dx}}$. Early investigations of the chemical composition made use of the fact that the geomagnetic field excludes low energy particles from approaching the earth at low latitudes. By going to sufficiently low latitudes, one was therefore able to select highly relativistic particles ($E \gg 3.5$ GeV/nuc) whose ionization energy loss is proportional to Z^2. In this way, it was possible to determine the charge composition of the cosmic radiation at high energies by a simple measurement of the ionization energy loss or stopping power, $\frac{dE}{dx}$.

3. $\underline{\frac{dE}{dx} \times C}$. An important step towards extending measurements of the chemical composition to particles of arbitrary energy was taken by Webber and McDonald (1955), who added a measurement of Cerenkov radiation to the $\frac{dE}{dx}$ measurement. Since both $\frac{dE}{dx}$ and the emission of Cerenkov radiation depend only on Z and β, this allowed the determination of both these parameters by the simultaneous solution of two equations (i.e. one for $\frac{dE}{dx}$ and one for the Cerenkov radiation). In this way, the chemical composition of the cosmic rays may be measured over a wide range of energies. This range of energies ($\sim 10^2$ to 10^5 MeV/nuc is essentially defined by the threshold and saturation velocities characteristic of the available radiator materials.

4. $\underline{\frac{dE}{dx} \times E}$. The simultaneous measurement of the ionization energy loss and the total kinetic energy of a particle provided a second

technique capable of measuring the chemical composition as a function of energy (Webber et al. 1972). The basic principle of this approach is similar to that of the technique described above, with the Cerenkov measurement replaced by a total energy measurement. The difference is that the energy depends on mass (A) and velocity (β), whereas the Cerenkov emission of a particle depends on Z and β. One is therefore required to assume a one to one correlation between charge and mass (e.g. $A \cong 2Z$ for $Z \lesssim 20$) in order to complete the set of equations for the unknowns A, Z and β. In one form or another, this technique has been applied over a range of energies extending from ~ 10 keV/nuc up to ~ 100 GeV/nuc. The limitation at lower energies derives from the macroscopic thickness of the $\frac{dE}{dx}$ detector, while that at high energies results from problems associated with the construction of a practical detector capable of completely absorbing a particle's energy. As one goes to energies $E \gtrsim 100$ MeV/nuc, it becomes increasingly improbable that a given particle will stop in a detector without undergoing a destructive nuclear interaction. Although it is still possible to estimate the energy of a particle under such circumstances, the resolution of the measurement is considerably reduced.

As resolutions of E and $\frac{dE}{dx}$ detectors continued to improve, even isotopic resolution became possible by this technique. In this case, the assumption of a one to one correspondence between A and Z is replaced by the more realistic assumption of discrete valued charge and mass distributions (see section B for a detailed discussion of the analysis). The mass resolution obtained by this technique characteristically deteriorates as one goes to heavier particles. ^{3}He and ^{4}He were thus the first isotopes separated. At the present time, the isotopes resolved

by this technique extend to nitrogen (Webber et al. 1973, 1973a) and beyond (Greiner 1972, Mewaldt et al. 1975).

5. Magnetic Spectrometers. Recently, large superconducting magnetic spectrometers have also been applied to the study of the charge and isotopic composition of the cosmic rays (Dauber 1971). These instruments allow the determination of both the sign and magnitude of a particle's charge, and thus have been used to search for antimatter in the cosmic rays (Buffington et al. 1973, Golden et al. 1974). It has also been possible to use the geomagnetic field as a rigidity filter (Juliusson 1975, Dwyer et al. 1975) in order to study the isotopic composition of the cosmic rays at energies of a few GeV/nuc, which are very much above the energies accessible by other methods (i.e. $E \lesssim$ 500 MeV/nuc).

6. Trajectory Definition. As geometrical factors (i.e. active areas) continued to increase in attempts to measure ever rarer particles, some means for trajectory definition of particles in experiments became essential. This has been accomplished using hodoscopes (thin strips of scintillator or flash tubes, for example), optical and digital spark chambers, and multiwire proportional counters. Using such detectors, it became possible to correct for the zenith angles at which particles were incident on detectors, and also to correct for variations in detector efficiency over their surfaces.

The various possible experimental approaches to the determination of the isotopic composition of the cosmic radiation will be discussed in greater detail in section B, along with the approach actually adopted for this experiment (section C).

B. The Measurement of Mass

For our purposes, an individual cosmic-ray particle may be described by three parameters: its mass (A), charge (Z) and velocity (β). This description ignores properties such as sense of velocity, degree of ionization and levels of nuclear and atomic excitation, but will suffice for the present discussion. As it turns out, the charge may sometimes be determined with no a priori knowledge of the other two, while velocity may be determined knowing only the charge. The determination of the mass, on the other hand, requires a knowledge of both charge and velocity and, in this sense, is the most difficult measurement of the three. One has available essentially five observables from which to determine the mass: the range of the particle in some absorber, its energy, its rate of energy loss to ionization, its rigidity and its emission of Cerenkov radiation upon passing through an appropriate radiator. Since there are only three parameters to be determined (A, Z and β), the problem is over specified, and it is sufficient to measure a subset consisting of only three of the five observables (assuming, of course, that they are all independent). In fact, it is sometimes sufficient to measure only two of the five by assuming the particles one will observe are stable against spontaneous nuclear decay, and thus have $A \sim ZZ$. In the following five subsections, each of the five observables will be discussed in turn.

1. <u>Energy</u>. The kinetic energy of a particle of mass A, charge Z and velocity β is given by

$$ {}^{A}_{Z}E(\beta) = (\gamma - 1)\, A\, m_p c^2 = A\, {}^{1}_{1}E(\beta) \qquad \text{(II.1)} $$

where γ denotes the relativistic Lorenz factor. As will be customary

for the remainder of this thesis, mass number and charge are indicated by superscripts and subscripts, respectively, on the left hand side of a variable. The first equation merely states the usual relativistic formula for the kinetic energy, while the last equality gives the scaling in A and Z. The dependence of ${}^{1}_{1}E$ on β is shown in figure II.1.

The energy of a particle is often measured using a calorimetric approach in which the particle's energy is used to ionize atoms in some suitable absorber. The energy deposited is then determined by some means characteristic of the specific type of detector being used. For example, the ionization calorimeter may consist of scintillation counters, in which case one observes the light emitted in the recombination of electrons and ions. Alternatively, solid state detectors may be used, in which case one observes an increase in the conductivity of the detector. Finally, one may use passive detectors such as stacks of emulsions or thin plastic sheets, in which case one looks for actual damage done to the material. In some cases, passive absorbers are inserted between layers of active material (e.g. scintillators), but this is done at the expense of the precision of the measurement. The resolution of such a measurement is physically limited by the Poissonian statistics associated with processes such as the production of ion-electron pairs, the conversion of such pairs to photons and the conversion of photons to photoelectrons in a photomultiplier tube. For example, if w_{pe} is the energy deposited per photoelectron produced, the resolution is given by

$$\sigma_E = \left(\frac{E}{w_{pe}}\right)^{1/2} w_{pe} \qquad \text{(II.2)}$$

For scintillation detectors, $w_{pe} \approx 20$ keV/photoelectron so that energy resolution better than 1% may be obtained for $E \geq 200$ MeV. For other

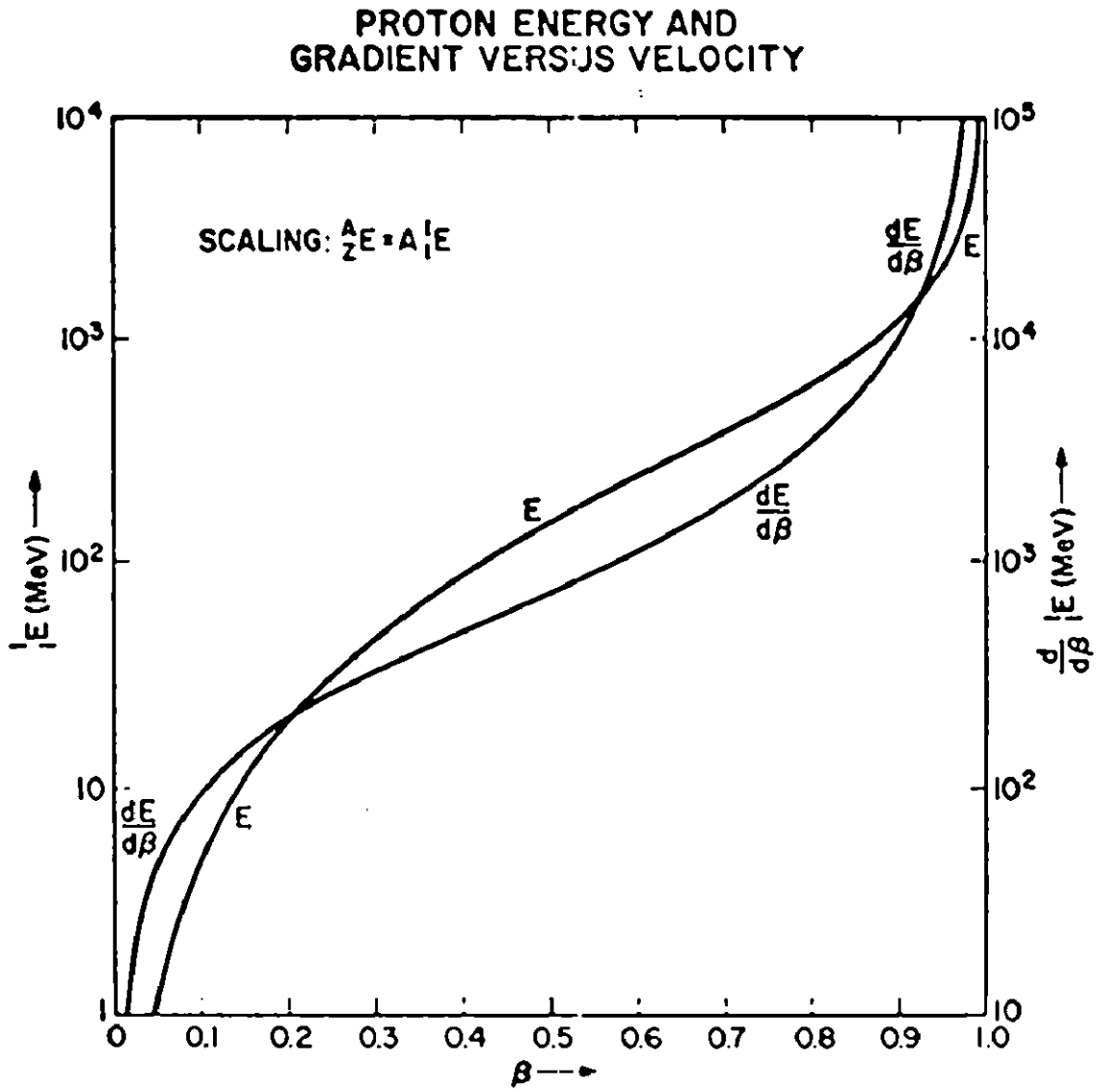

Figure II.1. The energy of a proton and its velocity derivative as functions of velocity.

types of detector (such as solid state), w_{pe} may be considerably smaller, and the energy resolution is accordingly increased. Practically, such resolutions are often far in excess of the requirements and not fully realized in many experiments.

2. Rate of Energy Loss to Ionization. The rate at which a particle loses energy by ionization, or stopping power, is given (in the Born approximation) by the Bethe-Bloch formula (Bohr 1913, Bethe 1930, Bloch 1933)

$$\begin{aligned} {}^{A}_{Z}\left(\frac{dE}{dx}\right) &= -4\pi r_e^2 m_e c^2 N_0 m_p Z_T n^T \left(\frac{Z}{\beta}\right)^2 \left[\ln\left(\frac{2m_e c^2 \beta^2 \gamma^2}{I(Z_T)}\right) - \beta^2\right] \\ &= Z^2 \, {}^{1}_{1}\left(\frac{dE}{dx}\right) \end{aligned} \qquad \text{(II.3)}$$

This expression breaks down at very high energies, where the ln γ increase of the term in brackets is eventually checked by the "density effect" (Sternheimer 1952, 1961). For particles of very low velocity, on the other hand, electron pickup becomes important and Z must be replaced by Z_{eff}, the effective (time averaged) charge of the particle. Neither of these effects are important for our considerations. Again, the scaling of the ionization energy loss in mass and charge is given by the last equality of equation II.3. The dependence of the proton ionization energy loss, ${}^{1}_{1}\left(\frac{dE}{dx}\right)$, on velocity, β, is shown in figure II.2.

A particle's rate of energy loss by ionization may be measured using proportional counters, ionization counters, thin scintillation counters or solid state detectors. Emulsions and thin sheets of plastic may also be used. Resolutions of the order of ~ 1% (dominated by Landau fluctuations; Symon 1948, Rossi 1952, Tschalar 1968, 1968a) are obtainable, depending upon the thickness of the detector, and the nature of the primary particle.

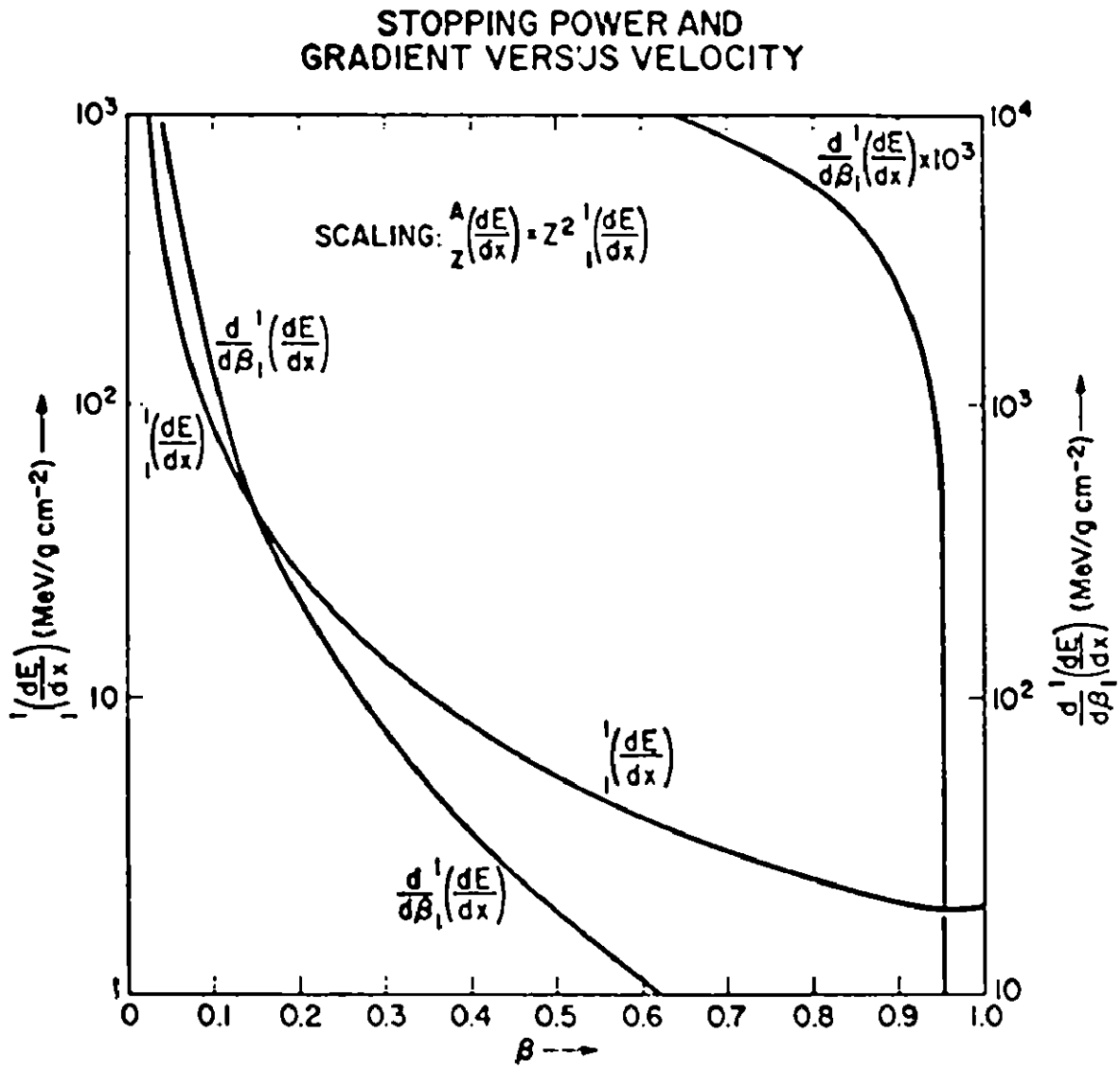

Figure II.2. The ionization energy loss by a proton and its velocity derivative as functions of velocity.

3. Range. Range is related to the stopping power, and energy, $E = (\gamma-1)Am_pc^2$, according to

$$ {}^{A}_{Z}R(\beta) = A m_p c^2 \int_{\gamma}^{1} \frac{d\gamma'}{{}^{A}_{Z}\left(\frac{dE}{dx}\right)} = \frac{A}{Z^2}\, {}^{1}_{1}R(\beta) \qquad \text{(II.4)} $$

where the scaling law given by the last equality follows from that for the stopping power, $\frac{dE}{dx}$. Figure II.3 shows the velocity dependence of the proton range, ${}^{1}_{1}R$.

The range of a particle is best measured by noting where the particle stops in a stack of emulsions or thin plastic detectors. More crude measurements using (thicker) solid state detectors or (even thicker) scintillation detectors have also been of some use in previous experiments. The range of a particle fluctuates due to the stochastic nature of the energy loss process. The distribution is characterized approximately by a Gaussian with standard deviation $\sigma_R = 0.01RA^{\frac{1}{2}}$ (Sternheimer 1960), and imposes a physical limit on the precision with which a meaningful measurement can be made.

4. Rigidity. Rigidity, the fourth observable, is given by

$$ {}^{A}_{Z}P(\beta) = \frac{pc}{Ze} = \frac{A}{Z}\frac{m_pc^2}{e}\gamma\beta = \frac{A}{Z}\, {}^{1}_{1}P(\beta) \qquad \text{(II.5)} $$

Once again, the last equality gives the scaling. The dependence of the proton rigidity, ${}^{1}_{1}P$, on velocity is shown in figure II.4.

The measurement of the rigidity of a particle is accomplished by measuring its radius of curvature in a known magnetic field. This makes use of the relation

$$ P = \frac{pc}{Ze} = \frac{B r_c c}{\cos\theta} \qquad \text{(II.6)} $$

where θ represents the angle between the particle's trajectory and the

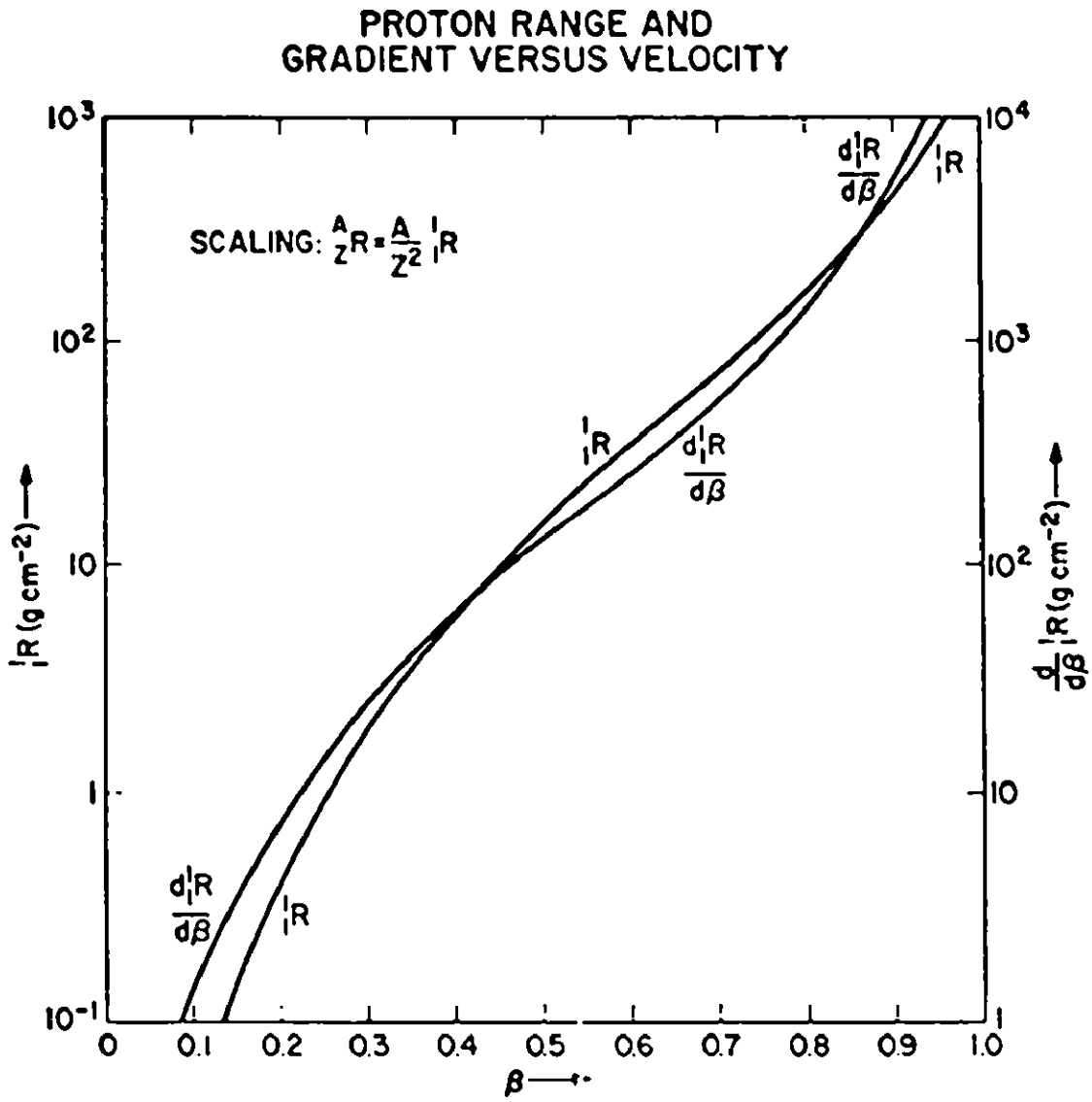

Figure II.3. The range of a proton and its velocity derivative as functions of velocity.

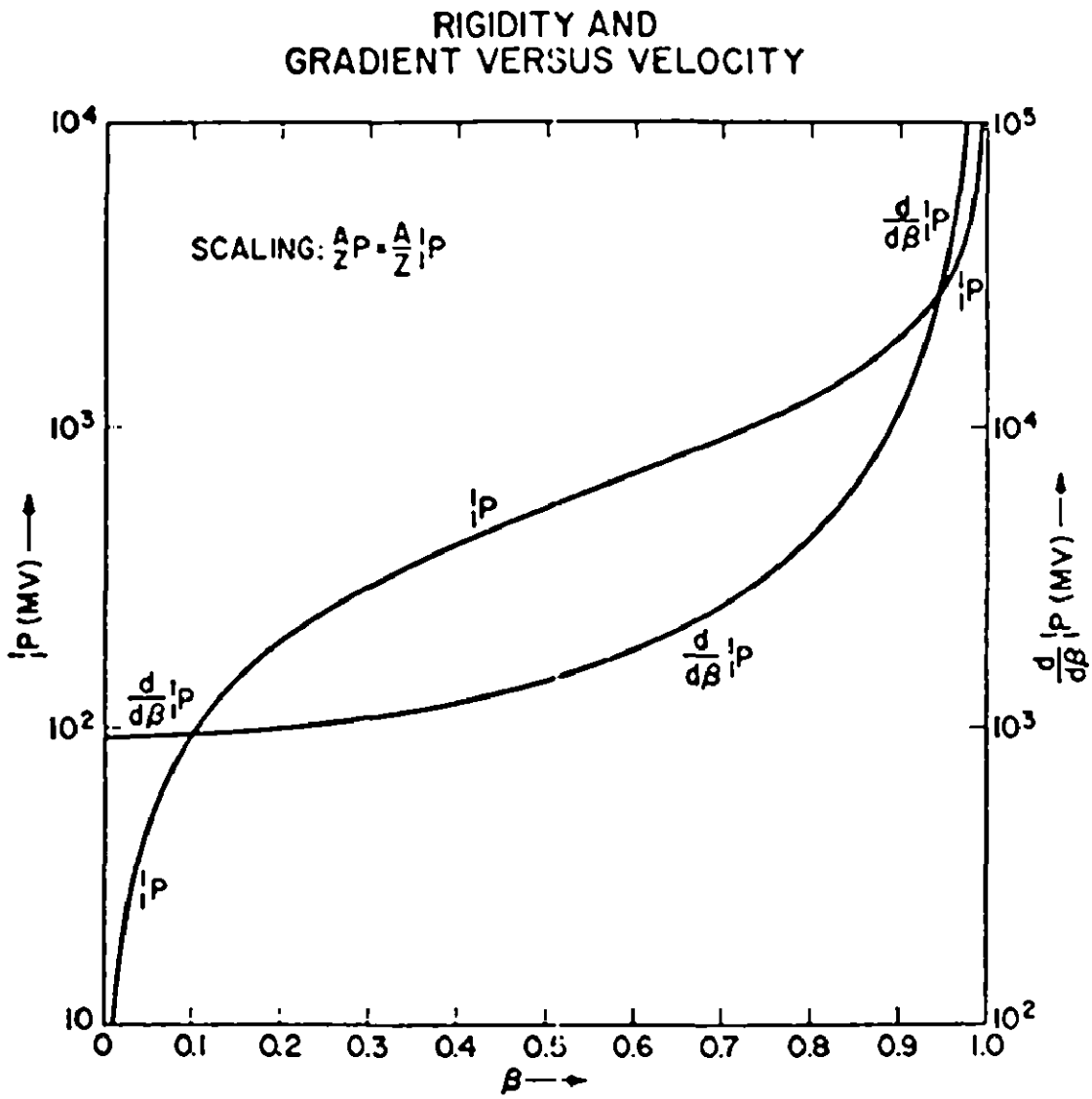

Figure II.4. The rigidity of a proton and its velocity derivative as functions of velocity.

magnetic field. The gyroradius, r_c, is determined using position sensitive detectors, such as cloud chambers, bubble chambers, multiwire proportional counters, spark chambers, emulsions or plastic detectors. Spark chambers and multiwire proportional counters have the advantage of being compatible with digital readout, while the others (also optical spark chambers) are generally capable of higher spatial resolution.

5. Cerenkov Radiation. Finally the Cerenkov response (in units of the response to a $\beta = 1$ proton) is given by (Jelley 1958)

$$ {}^{A}_{Z}C(\beta) = \left(\frac{Z^2}{n^2-1}\right)\left(n^2 - \frac{1}{\beta^2}\right) = Z^2\, {}^{1}_{1}C(\beta) \qquad \text{(II.7)} $$

The last equality again gives the scaling, and the proton Cerenkov response, ${}^{1}_{1}C$, is illustrated in figure II.5.

Cerenkov radiation may be observed by placing a radiator with a suitable index of refraction n (depending upon the range of velocities one intends to study) in a diffuse reflecting box. The light emitted by the radiator is then observed by photomultiplier tubes. The dominant contribution to the resolution obtained is the statistical process of collecting photons and converting them to photoelectrons, which is governed by Poissonian statistics. If a Cerenkov response of unity corresponds to ϵ photoelectrons, then the Cerenkov resolution is given by

$$ \sigma_C = \left(\frac{c}{\epsilon}\right)^{1/2} \qquad \text{(II.8)} $$

Values $\epsilon \sim 10$ are possible, depending on experimental details such as the thickness of the radiator, efficiency of photon collection, and so on.

6. Mass Determination. Given observations of some subset of the five observables discussed above (i.e. E, $\frac{dE}{dx}$, R, P and C), the relevant subset of equations II.1, II.3, II.4, II.5 and II.7 may be solved

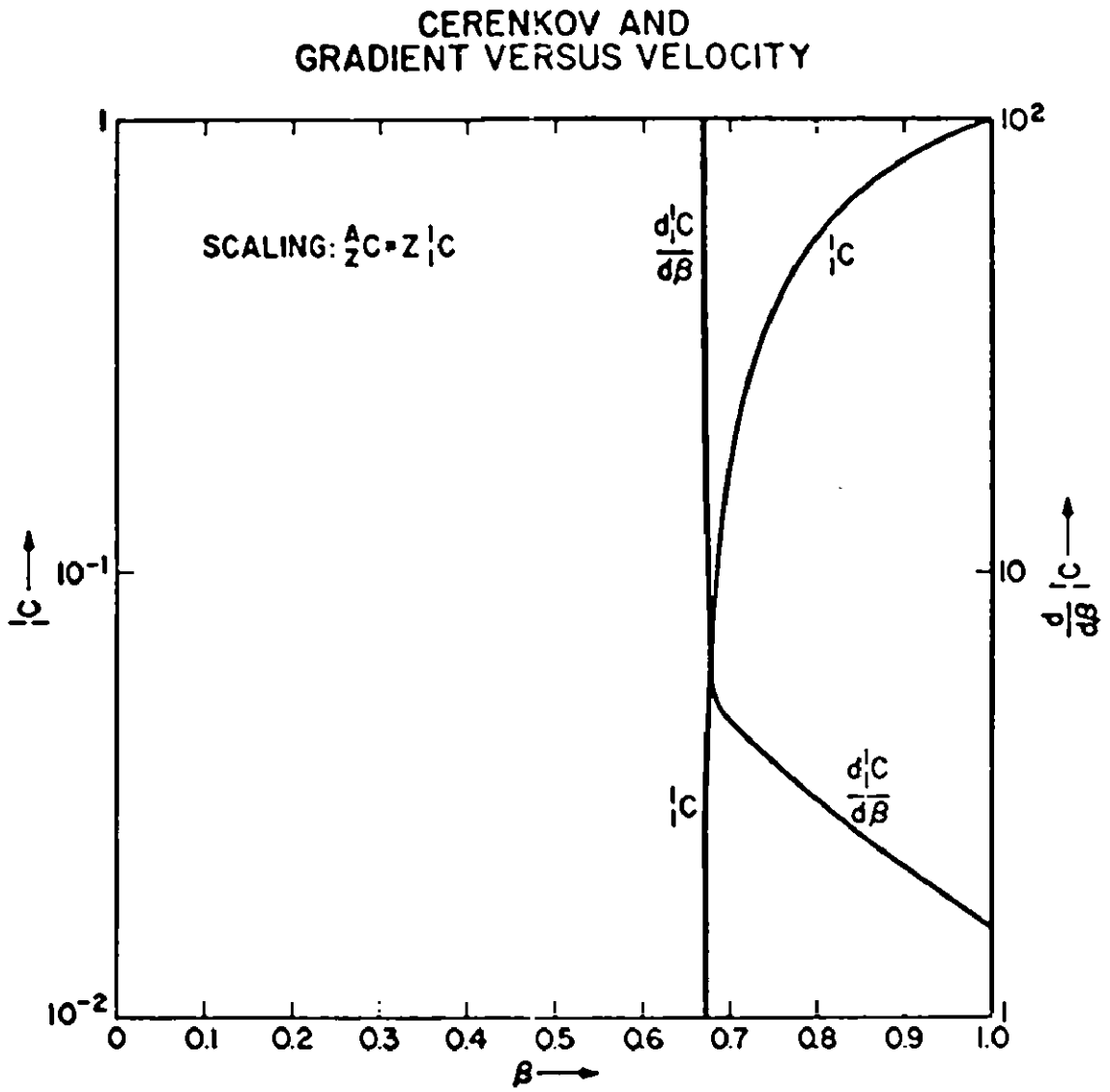

Figure II.5. The emission of Cerenkov radiation by a proton and its velocity derivative as functions of velocity.

simultaneously for the mass of a particle, together with its charge and velocity. We now consider the question of what is the optimal subset of the observables which one can observe. Suppose, for example, that we have a ^{10}Be incident on an apparatus with velocity $\beta = 0.5$. We have shown in figure II.6 how the analysis might proceed if we measure (for example) the observables E, $\frac{dE}{dx}$ and/or R. The appropriate numerical (i.e. observed) values have been substituted into each of equations II.1, II.3 and II.4, and the resulting relations solved for the mass, A, as a function of charge and velocity. The results are illustrated in figure II.6 for the particular cases where Z = 3, 4 and 5. Consider first a two parameter analysis utilizing the observables E and R. The various possible results of such an analysis are represented in figure II.6 by the intersections of E and R curves of the same charge, Z. In particular, the solutions are

$$\begin{pmatrix} A \\ Z \\ \beta \end{pmatrix} = \begin{pmatrix} 20 \\ 3 \\ 0.37 \end{pmatrix}, \begin{pmatrix} 10 \\ 4 \\ 0.50 \end{pmatrix} \text{ and } \begin{pmatrix} 5 \\ 5 \\ 0.64 \end{pmatrix} \tag{II.9}$$

for the present case. It is apparent from the above example that a two parameter analysis sometimes may be sufficient to uniquely determine all three of the unknowns A, Z and β when supplemented with the requirement that the observed particle be one of the known, stable isotopes. In particular, for the present case this immediately rules out the solutions ^{20}Li and ^{5}B. The results of a three parameter analysis may, in similar fashion, be represented as the simultaneous intersection of all three of the appropriate curves on a diagram such as figure II.6. In table II.1, the results of the various possible two parameter analyses involving the observables E, $\frac{dE}{dx}$, R and P have been tabulated for Z = 3, 4 and 5. We have again taken the actual event to be a ^{10}Be of velocity $\beta = 0.5$.

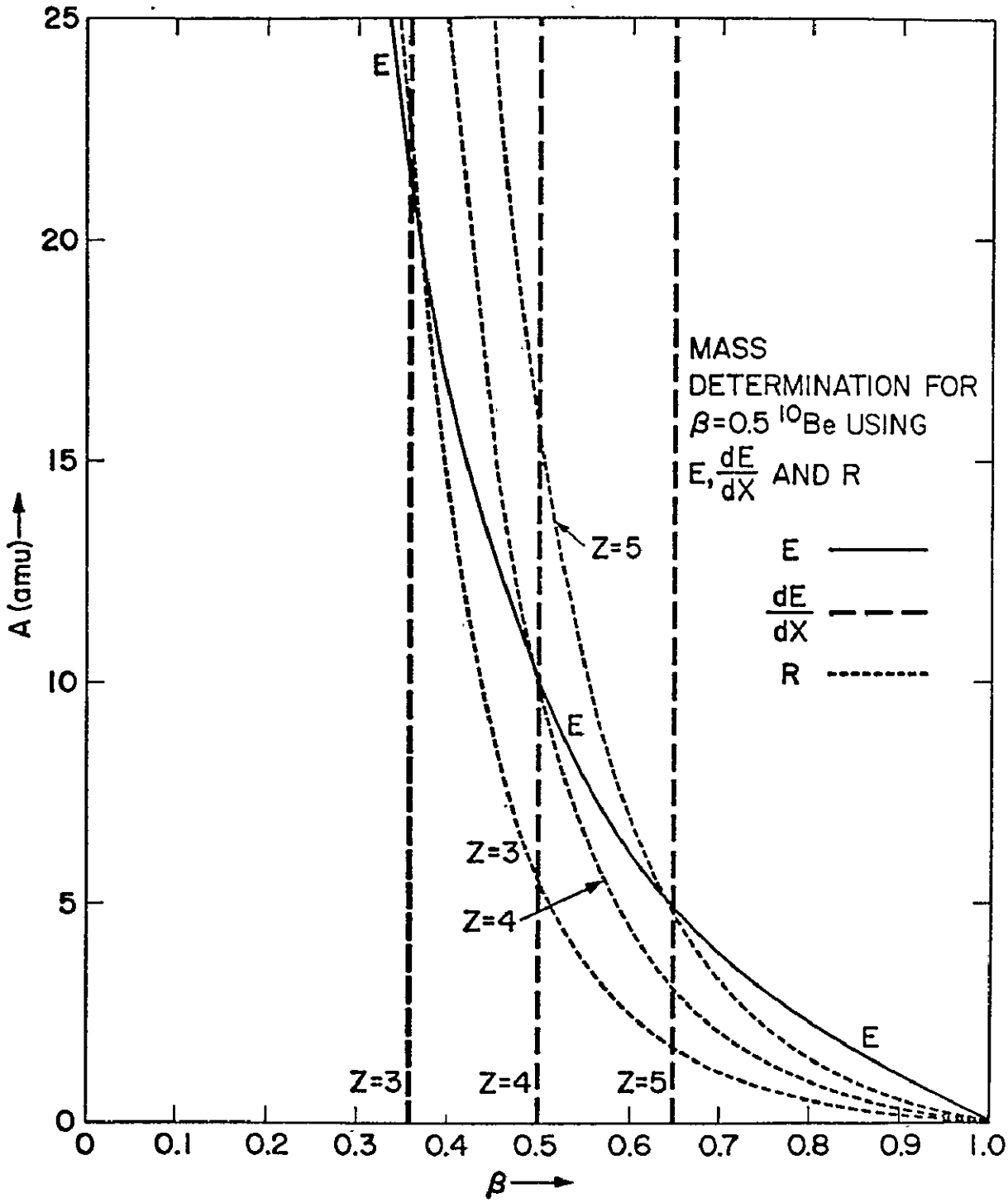

Figure II.6. Mass as a function of assumed velocity derived from measurement of energy, ionization energy loss or range of a ^{10}Be with velocity $\beta = 0.5$.

TABLE II.1

Results of Various Possible Two Parameter Analyses

Involving E, $\frac{dE}{dx}$ and R for ^{10}Be Event of Velocity $\beta = 0.5$

Analysis Mode	Z	A	β	Stability
$E x \frac{dE}{dx}$	3	21.20	0.360	
	4	10.00	0.500	Stable
	5	4.85	0.650	
ExR	3	20.00	0.372	
	4	10.00	0.500	Stable
	5	5.00	0.642	
ExP	3	5.30	0.630	Marginal
	4	10.00	0.500	Stable
	5	16.45	0.403	
$\frac{dE}{dx} x R$	3	22.40	0.360	
	4	10.00	0.500	Stable
	5	4.80	0.650	
$\frac{dE}{dx} x P$	3	11.10	0.360	
	4	10.00	0.500	Stable
	5	8.40	0.650	Marginal
RxP	3	8.50	0.464	Marginal
	4	10.00	0.500	Stable
	5	11.25	0.540	Stable

Since the event considered would be below Cerenkov threshold, only an upper limit on the velocity (i.e. $\beta \leqslant 0.67$) can be extracted from a Cerenkov measurement. For this reason, the observable C has not been considered in table II.1. From the table, we see that the only reasonable result (i.e. one yielding a stable particle) of a two parameter analysis involving combinations of the observables E, $\frac{dE}{dx}$ and R is a ^{10}Be of velocity $\beta = 0.5$, as desired. Furthermore, we gain little more than redundancy (which may be useful in the identification and elimination of background) by combining all three of these observables in a three parameter analysis. In particular, the degeneracies present in the various possible two parameter analyses (without the stability condition) are not removed by the three parameter analysis unless the measurements are extremely precise. This is readily apparent, both from table II.1 and figure II.6. The two parameter analyses using either E or $\frac{dE}{dx}$ in combination with P result in extraneous solutions which are only marginally rejected (or accepted) by the stability requirement. A three parameter analysis using all three of these observables (E, $\frac{dE}{dx}$ and P), however, easily removes the degeneracies (even without the stability condition), as opposed to the case where E, $\frac{dE}{dx}$ and R are used. Finally, the two parameter analysis using R and P is the most ambiguous. None of the extraneous solutions with $2 \leq Z \leq 8$ generated by this approach can easily be rejected by the stability condition. In this case, a third parameter (either E or $\frac{dE}{dx}$) is absolutely essential for the analysis. We may conclude from the above discussion that any combination of E, $\frac{dE}{dx}$ and R is adequate for a two parameter analysis. On the other hand, the combination E, $\frac{dE}{dx}$ and P yields the best three parameter analysis. We also note in passing that both of the observables E and R require that a particle be

stopped in some absorber for their determination. The probability of being able to do this without having the particle destroyed in a nuclear interaction decreases exponentially as the range of the particle (and also its energy) is increased. As a result, an analysis involving the measurement of $\frac{dE}{dx}$ and P (which do not require that a particle be stopped) becomes increasingly attractive. The measurement of Cerenkov response, C, is similarly attractive for velocities above the Cerenkov threshold (i.e. $\beta \geq 0.67$ for a radiator with $\underline{n} = 1.5$).

7. Resolution. The above discussion of various analysis schemes for mass determination is essentially independent of the resolutions obtainable or other technological constraints. We now consider the resolution with which it is desirable to measure the various observable parameters in order to achieve isotopic separation. Consider, for example, a mass distribution of the form

$$f(A) = k \exp\left(-\frac{A^2}{2\sigma^2}\right) + \exp\left[-\frac{(A-1)^2}{2\sigma^2}\right] \tag{II.10}$$

This represents the result of measuring two neighboring isotopes (of masses $A_1 = 0$ and $A_2 = 1$) with abundances in the ratio k:1, respectively, with a mass resolution given by σ. For the purposes of this discussion, the mass scale is arbitrary to within a constant, i.e. the isotopes could as well be of masses $A_1 = 9$ and $A_2 = 10$, in which case one need only make the substitution $A \rightarrow A-9$. The condition for the existence of an extremum (peak or valley) in this distribution at $A = A_o$ is

$$\sigma^2 = \left(A_o - \frac{1}{2}\right) \Big/ \ln\left(\frac{k A_o}{1 - A_o}\right) \tag{II.11}$$

If we choose k = 2 (which is approximately what we expect for the case of cosmic ray ^{9}Be and ^{10}Be), the extremum location, A_o, is related to

the resolution, σ, as shown in figure II.7. In this figure, the value of the distribution function at the extremum (i.e. the height of the peak or valley) is also indicated. For example, consider the case where $\sigma = 0.5$. From figure II.7, we see that there is only one extremum (at $A_o = 0.085$) in this case, which must correspond to the major ($A_1 = 0$) peak. The minor ($A_2 = 1$) peak is apparently lost in the tail of its neighbor. If we now improve the resolution to $\sigma = 0.3$, there are three solutions to equation II.11. These are at $A_o = 0.005$ (the major peak), $A_o = 0.599$ (the valley) and $A_o = 0.991$ (the minor peak). We also see that the height of the distribution is $f(0.005) = 2$, $f(0.559) = 0.674$ and $f(0.991) = 1.10$ at the major peak, valley and minor peak, respectively.

The condition on the mass resolution for the appearance of a valley between the two distributions is $\sigma \leqslant 0.35$ in the particular case where $k = 2$, as may readily be seen from figure II.7. This result may be generalized to arbitrary k by writing $\sigma \leq \sigma_{crit}$, where σ_{crit} represents a maximum of the function $\sigma(A_o)$ defined by equation II.11. Again, this is readily apparent from figure II.7. For the general case, we thus require

$$\sigma^2 \leqq \sigma_{crit}^2 = A_o(1-A_o) = \frac{\left(A_o - \frac{1}{2}\right)}{\ln\left(\frac{kA_o}{1-A_o}\right)} \qquad \text{(II.12)}$$

where the second equality is merely a restatement of equation II.11. From equation II.12, we see that a knowledge of any one of the three parameters k, A_o and σ_{crit} defines the other two. In particular, the dependence of σ_{crit} on k is shown in figure II.8. This figure shows how the requirement on the resolution for the appearance of a valley becomes more strict as the relative abundance of the minor isotope

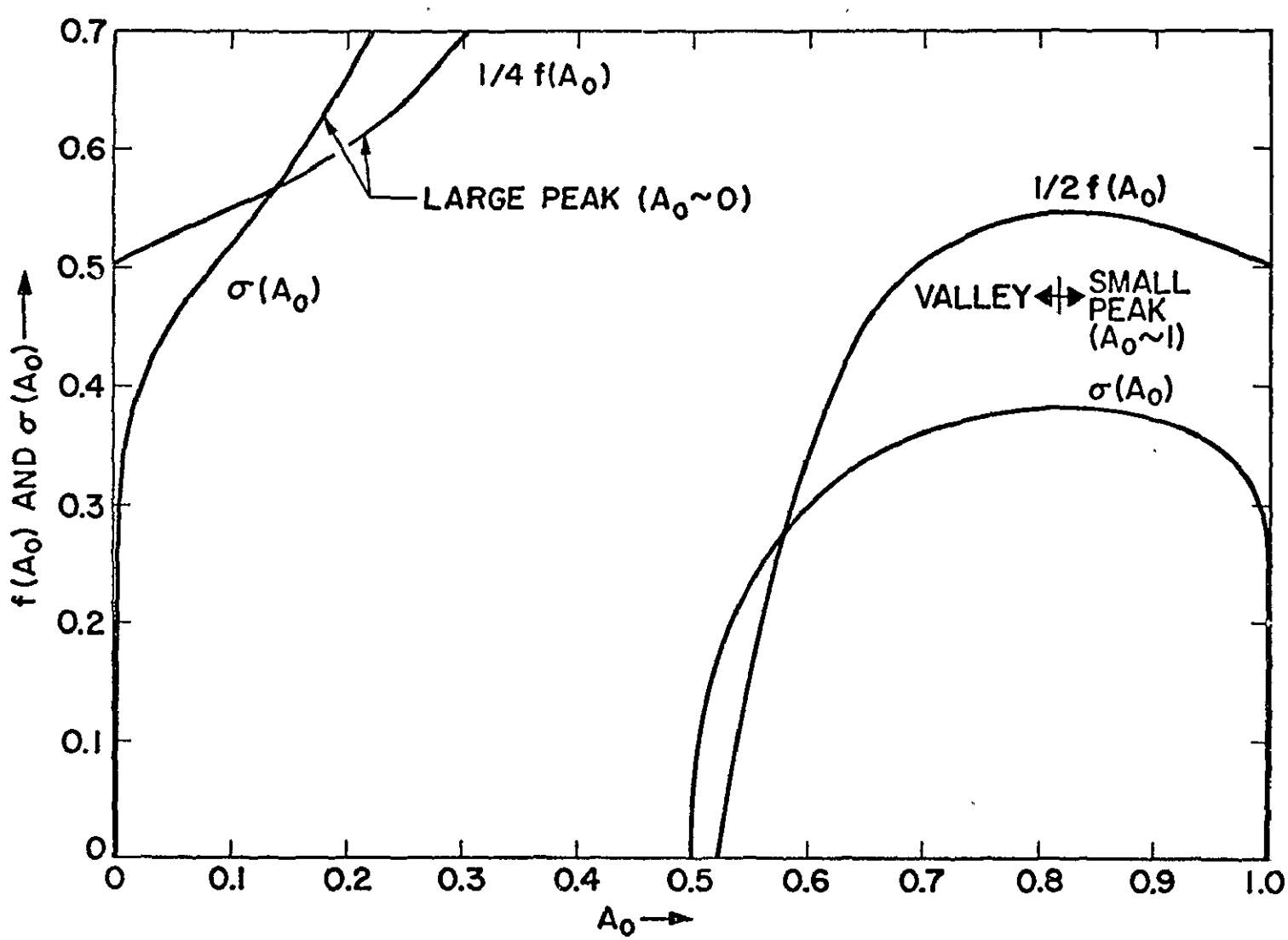

Figure II.7. Resolution as a function of extrema locations for a bi-Gaussian distribution with amplitude ratio k = 2. Values of the distribution function at the extrema are also indicated.

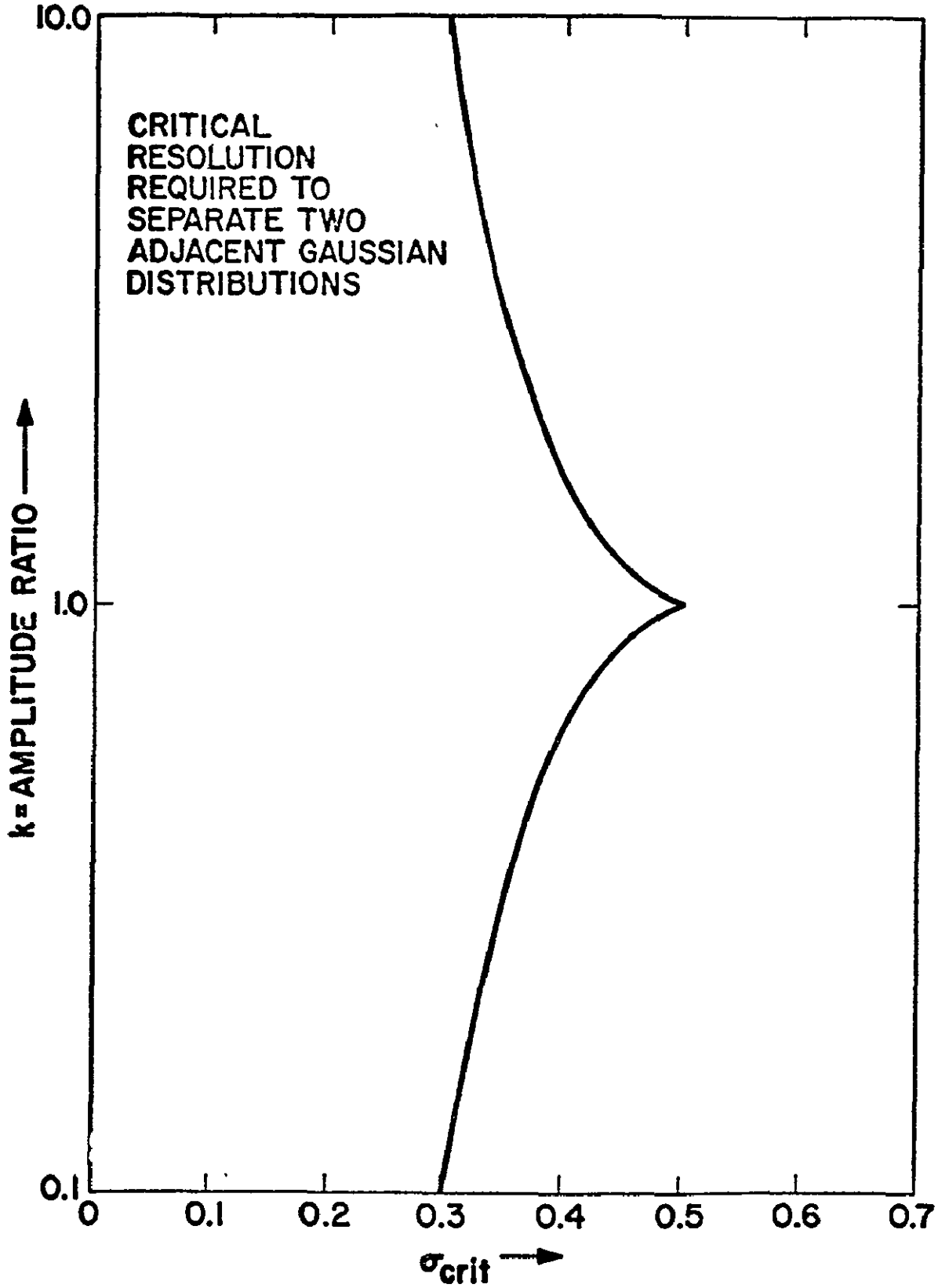

Figure II.8. Critical resolution required for the appearance of a valley in a bi-Gaussian distribution as a function of amplitude ratio.

(e.g. ^{10}Be) is decreased.

We emphasize that the existence of a valley between two neighboring isotopes in a mass distribution is only one of many possible definitions of the critical resolution required to "separate" the two isotopes. One may even rely completely on deconvolution techniques in which case the "separation" criterion is on the accuracy to which one knows the resolution and indeed the shape of the mass distribution, rather than on the magnitude of the resolution itself.

In order to estimate the resolution obtainable by the various analyses described above, we formalize equations II.1, II.3, II.4, II.5 and II.7 as follows:

$$ {}^{A}_{Z}O_i(\beta) = \underline{O}_i \tag{II.13} $$

Here $\underline{O}_i$ represents the observed value of a given observable, while ${}^{A}_{Z}O_i(\beta)$ gives its functional dependence on Z, A and β. For example for the observable E, we have

$$ \underline{O}_E = E \tag{II.14} $$

and

$$ {}^{A}_{Z}O_E = (\gamma-1) A m_p c^2 \tag{II.15} $$

Equation III.13 may be solved for the mass, $A_i(\beta)$, as a function of $\underline{O}_i$, Z and β. The functions $A_E(\beta)$, $A_{\frac{dE}{dx}}(\beta)$ and $A_R(\beta)$ are shown in figure II.6 for the particular case where the observed particle is a ^{10}Be of velocity β= 0.5. Expanding $A_i(\beta)$ to first order in β about β_{oi}, we have

$$ A_i(\beta) \cong A_i(\beta_{oi}) + (\beta - \beta_{oi}) \frac{\partial A_i}{\partial \beta_{oi}} \tag{II.16} $$

where $\frac{\partial A_i}{\partial \beta_{oi}}$ represents the velocity derivative of $A_i(\beta)$ evaluated at $\beta = \beta_{oi}$. We proceed with a two parameter analysis as described in the previous section by writing equation II.16 again for a second observable $j \neq i$. Solving for the mass, we then obtain the result

$$A = \frac{A_i(\beta_o)\frac{\partial A_j}{\partial \beta_o} - A_j(\beta_o)\frac{\partial A_i}{\partial \beta_o}}{\frac{\partial A_j}{\partial \beta_o} - \frac{\partial A_i}{\partial \beta_o}} \tag{II.17}$$

where we have put $\beta_o = \beta_{oi} = \beta_{oj}$. The uncertainty in the result of the two parameter analysis as given by equation II.17 enters through the dependences of the functions $A_i(\beta)$ and $A_j(\beta)$ on the observations $\underline{O}_i$ and $\underline{O}_j$, respectively. In particular, if we let β_o be the velocity corresponding to A so that $A = A_i(\beta_o) = A_j(\beta_o)$, then the uncertainty, σ_A, in the mass determination, A, is given by

$$\sigma_A = \left[\left(\frac{\sigma_i}{\Delta_{ij}}\right)^2 + \left(\frac{\sigma_j}{\Delta_{ji}}\right)^2\right]^{\frac{1}{2}} \tag{II.18}$$

where

$$\Delta_{ij} = \left| \left[\left(\frac{\partial A_i}{\partial \beta_o}\right)^{-1} - \left(\frac{\partial A_j}{\partial \beta_o}\right)^{-1}\right] \left(\frac{\partial}{\partial \beta_o} \; {}^{A}_{Z}O_i\right) \right| \tag{II.19}$$

defines the mass resolution scale factor, and σ_i denotes the resolution of the observation $\underline{O}_i$. In order to interpret the scale factors, assume both parameters contribute equally to the resolution in equation II.18. In this case, the condition for the existence of a valley between two neighboring mass distributions is given by

$$\sigma_i \leq \left(\frac{\Delta_{ij}\,\sigma_{crit}}{\sqrt{2}}\right) \tag{II.20}$$

where σ_{crit} is defined by equation II.12. In the particular case where the abundances of the two isotopes are in the ratio 2:1 (i.e. k = 2), this reduces to

$$\sigma_i \leq 0.25\,\Delta_{ij} = \sigma_i^{max} \tag{II.21}$$

The σ_i^{max} are listed in table II.2 for the various possible observables and analyses, again for the particular case of a ^{10}Be with velocity β = 0.5. We also recall that this table strictly applies only to the case where k = ^{9}Be/^{10}Be = 2, and both observables in a two parameter analysis contribute equally to the uncertainty in the resultant mass.

C. The Experiment

1. Specialization to ExR. We chose to do an experiment measuring the observables E, $\frac{dE}{dx}$ and R which utilized the existing technology in large area scintillation counters at our laboratory. The measurement of range was to be the unique feature of the experiment. This was accomplished by stopping particles in a stack of relatively thin scintillation counters, which then provided multiple measurements of both $\frac{dE}{dx}$ and E as functions of the residual range of the particle. The result is a redundancy of mass determinations, which may then be used for the identification and removal of background. In the remainder of this section, we will specialize the discussion of section B to an experiment of the multiple $\frac{dE}{dx}$ x E x R variety.

In figure II.9, the energy of a proton is given directly as a function of its range. Curves corresponding to other particle species will have the same (log-log) shape, only offset in both R and E according to the scaling laws given by equations II.1 and II.4. It is apparent from the figure that, over a considerable range (up to R $\cong$ 100 g cm^{-2}),

TABLE II.2

Resolution Required to Resolve a ^{10}Be

of

Velocity $\beta = 0.5$ in a Two Parameter Analysis

Auxiliary Observable	Primary Observable			
	E	$\frac{dE}{dx}$	R	P
E	----	1.7%	1.7%	1.3%
$\frac{dE}{dx}$	2.3%	----	2.3%	2.5%
R	1.0%	1.0%	----	1.8%
P	2.3%	3.3%	5.8%	----

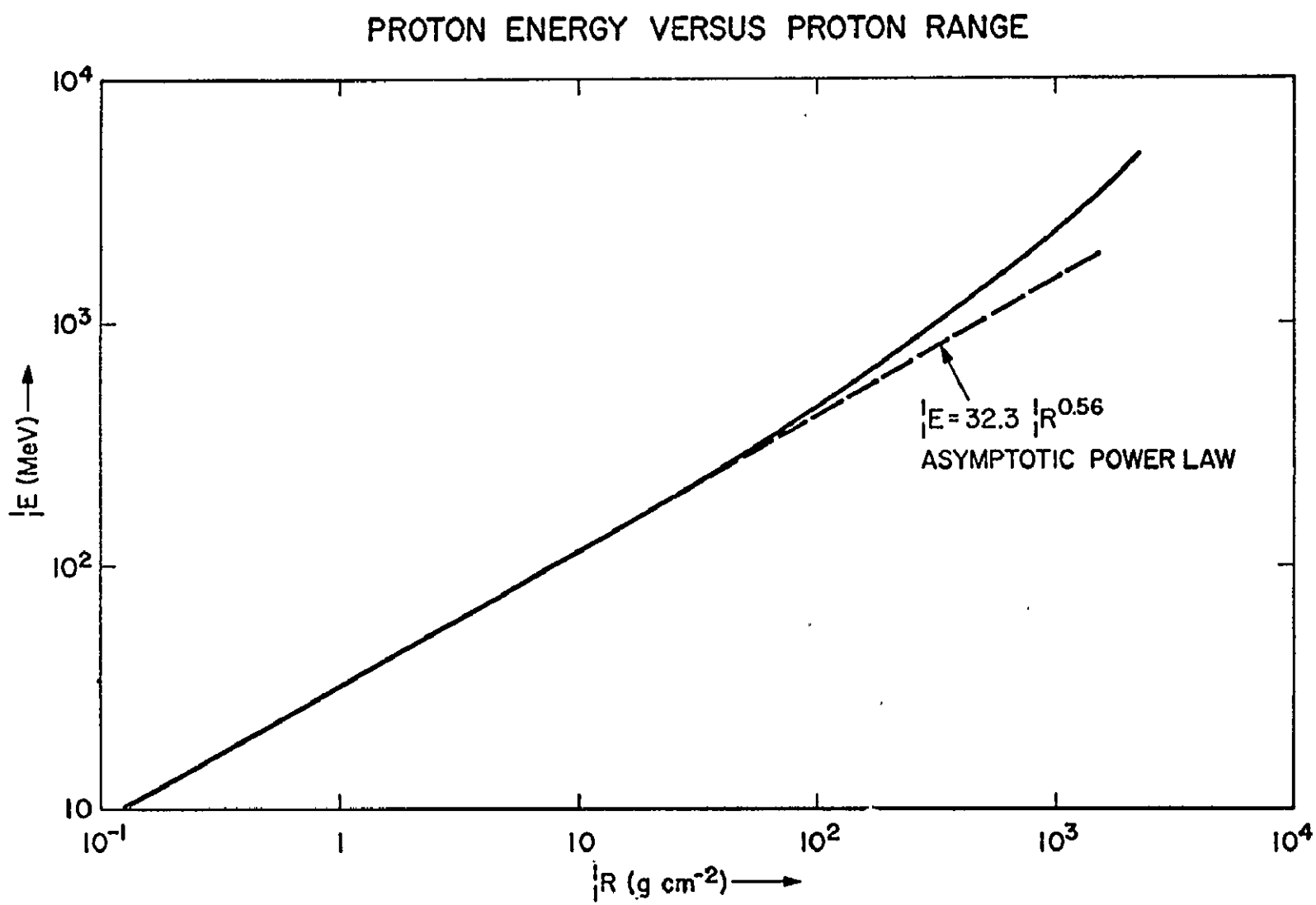

Figure II.9. Energy versus range for protons.

the relation

$$\frac{1}{A}\left({}^{A}_{Z}E_{MeV}\right) = {}^{1}_{1}E_{MeV} = 32.3\left({}^{1}_{1}R_{g\,cm^{-2}}\right)^{0.56}$$
$$= 32.3\left[\frac{Z^2}{A}\left({}^{A}_{Z}R_{g\,cm^{-2}}\right)\right]^{0.56} \qquad \text{(II.22)}$$

is an adequate approximation to the range energy relation. Solving for the mass, A, in terms of R, E and Z, one has the result

$$A = (3.72\times10^{-4})\,Z^{-1.12}\left({}^{A}_{Z}R_{g\,cm^{-2}}\right)^{-1.27}\left({}^{A}_{Z}E_{MeV}\right)^{2.27} \qquad \text{(II.23)}$$

The resolution of the mass determination is then given by

$$\left(\frac{\sigma_A}{A}\right)^2 = 1.61\left(\frac{\sigma_R}{R}\right)^2 + 5.15\left(\frac{\sigma_E}{E}\right)^2 \qquad \text{(II.24)}$$

This reduces to

$$\sigma_A^{-2} = \left(\frac{\sigma_R}{0.762}\right)^2 + \left(\frac{\sigma_E}{64.8}\right)^2 \qquad \text{(II.25)}$$

for the particular case of a ^{10}Be with velocity $\beta = 0.5$. This is in agreement with the result given by equation II.18. Equation II.24, however, applies to particles of arbitrary Z, A and β. It is apparent from this result that an experiment of the E x R variety has the poorest resolution for the heaviest isotope at the lowest energy.

2. <u>Range Resolution</u>. From equation II.24, we estimate that the range must be resolved to within ~ 2% in order to clearly resolve the isotope ^{10}Be (as defined by equation II.21). Thus if we take the resolution to be $\sigma_R \sim 1$ g cm^{-2} (i.e. the thickness of a thin scintillator), we conclude that ^{10}Be can only be resolved for $R \gtrsim 50$ g cm^{-2}. Clearly, we must do better by at least an order of magnitude if this approach is to be feasible (e.g. the mean free path of ^{10}Be against nuclear inter-

actions in scintillator is ~ 22 g cm^{-2}). Thus, we are required to resolve the range to much less than the thickness of a single scintillator. A simple solution is to use the known range energy relation (i.e. see figure II.9) to deduce the range in the last detector penetrated from the energy deposited. If we approximate the range energy relation by equation II.22, then

$$R_{last} = \left(2.02 \times 10^{-3}\, g\, cm^{-2}/MeV^{1.79}\right)\left(\frac{A}{Z^2}\right)\left[\frac{1}{A} H_{last}\right]^{1.79} \qquad \text{(II.26)}$$

where H_{last} is the pulse height (in MeV) in the last detector penetrated. This, however, requires an a priori knowledge of A and Z. This problem may be circumvented by writing equation II.26 again for the range in the last two detectors penetrated:

$$R_{last} + T_{last-1} \sec\theta = \left(2.02 \times 10^{-3}\, g\, cm^{-2}/MeV^{1.79}\right)\left(\frac{A}{Z^2}\right)\left[\frac{1}{A}\left(H_{last} + H_{last-1}\right)\right]^{1.79} \qquad \text{(II.27)}$$

Here T_{last-1} is the thickness of the next to last detector penetrated, and θ is the zenith angle at which the particle is incident. Equations II.26 and II.27 may then be solved to give the result

$$R_{last} = T_{last-1} \sec\theta \left[\left(1 + \frac{H_{last-1}}{H_{last}}\right)^{1.79} - 1\right]^{-1} \qquad \text{(II.28)}$$

which depends only on the pulse heights in the last two detectors, the exponent of the range energy relation, the thickness of the next to last detector and the zenith angle, all of which are observable. The problem is, then, apparently solved, as the range resolution has been considerably improved.

3. Scintillator Saturation. There is yet another effect which must be considered, namely, the saturation of the response of the scintillation counters used. This has two effects. In the first place, the response of a scintillator is now a nonlinear function of the energy deposited, as well as Z and A. Although the effect is not completely understood in a quantitative sense, it does seem possible to conclude that the saturation of scintillator response (i.e. $\frac{dL}{dE}$) depends only on Z and β, and not on mass. The detailed form of this dependence, however, must be measured for each specific application. This may be done by using an accelerator for extensive calibrations. Alternatively, it may be accomplished (with less precision) by using in flight data. The latter possibility relies on particles known to stop near detector boundaries, for which the range is well known. The second effect of the scintillator saturation concerns our ability to estimate the range in the last detector. One may hope that an assumption of a power law response is still approximately valid, in which case equation II.22 (with adjusted parameters) may still be applied, perhaps in an iterative fashion. There is some hope for this since the saturation is expected to be a relatively small effect for the particles of interest (i.e. particles of low charge, and in particular, ^{10}Be). However, the exact effect of scintillator saturation is not known a priori, and the calibration may be required.

4. Additional Considerations. Yet another factor which should be considered is the requirement to obtain a statistically significant result. As an example, consider an isotope such as ^{10}Be. The differential flux of this isotope is expected to be $\sim 5 \times 10^{-5}$ particles $m^{-2}ster^{-1}sec^{-1}$ $(MeV/nuc)^{-1}$ (Tsao et al. 1973). Assuming an exposure time of 24 hours and an energy window of $\sim$ 400 MeV/nuc in which the

experiment is sensitive, we expect to observe roughly 1700 G particles, where G is the geometrical factor of the experiment in m^2 ster. Even with a geometrical factor $G = 0.25\ m^2$ ster (which is the largest we can attain using the available gondola), we expect only $\sim 425\ ^{10}Be$, even before considering losses due to nuclear interactions, dead time and so on. Clearly these effects will be important, so that we should make every effort to maximize the geometrical factor. Finally, a constraint on the upper limit was set by the requirement to utilize existing hardware wherever possible, including certain detectors, pulse height analyzers and the gondola.

5. Description of Experiment. To summarize the preceding discussion, the experiment was designed to operate in a multiple $\frac{dE}{dx} \times E \times R$ mode in order to maximize its isotopic separation. The heart of the experiment consists of a stack of scintillation counters with which it is possible to determine the range of a particle and also to test for background by consistency checks.

a. Overview

The physical layout of the experiment is illustrated schematically in figure II.10. Briefly, it consists of a thin trigger scintillator, D1, followed immediately by a Cerenkov radiator, D2. This is followed by a spark chamber, which was used to define particle trajectories through the experiment. This was especially important for the identification of stopping particles, the determination of particle ranges from their normal projections, and mapping of positional variations in the responses of the various detectors. The spark chamber is followed by the totally active stack of 12 scintillation counters, D3-14, which comprised the heart of the experiment. These allowed multiple measure-

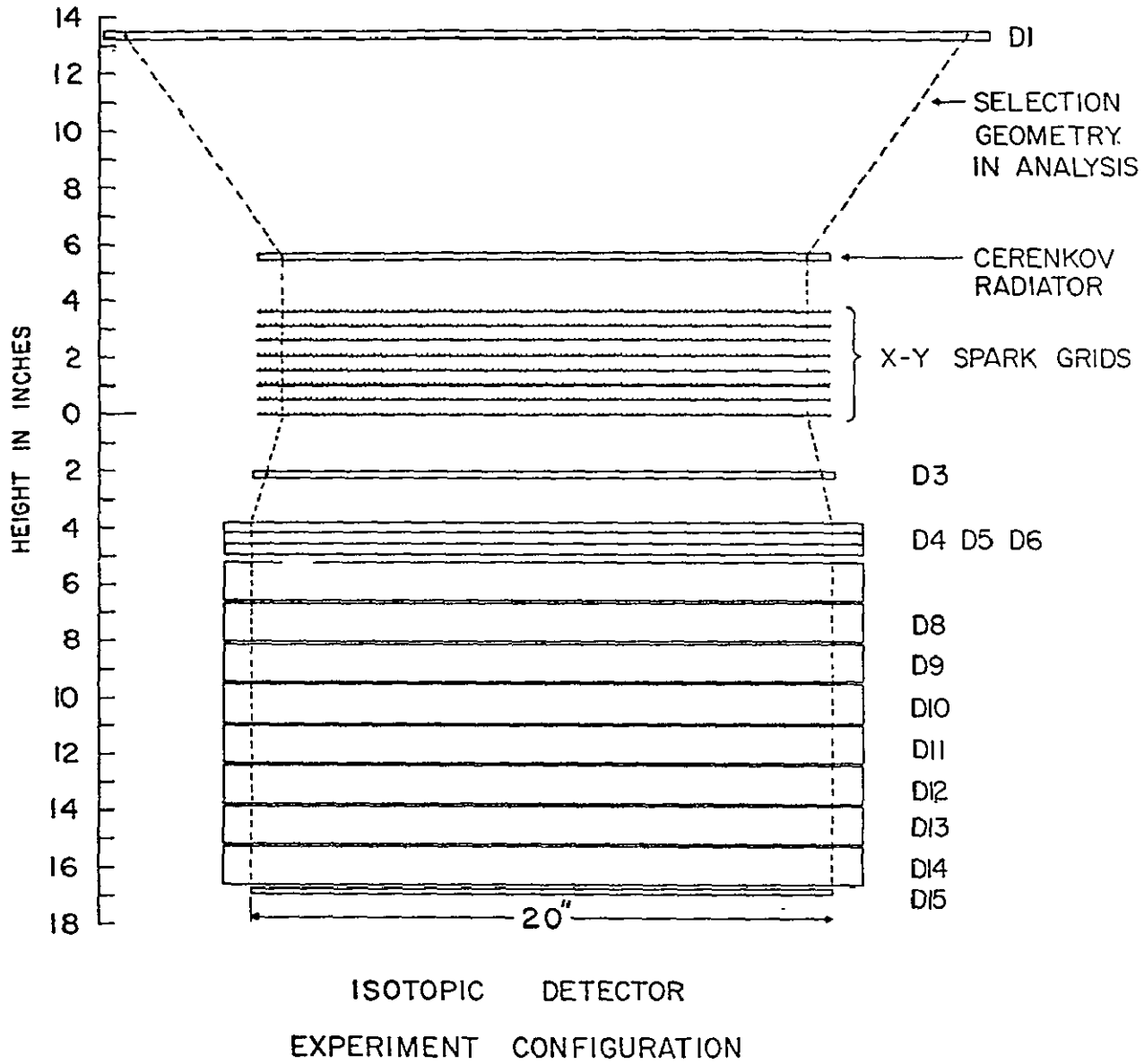

Figure II.10. Schematic diagram of the experiment.

ments of E and $\frac{dE}{dx}$ as functions of R for each event analyzed. The final element, D15, is a penetration counter, and gives only a "yes" or "no" output. The scintillators are all made of Pilot Y, chosen for its good response to heavily ionizing particles.

b. Testing and Checkout of Detectors

Each detector assembly (consisting of scintillator, light pipes, photomultiplier tubes and pre-amplifiers) was evaluated in a light tight box using muons and a 1μC, P_{μ}^{238} alpha source. For the scintillators, commercial amplifiers, pulse height analyzers and high voltage supplies were used for these tests; in general, the high voltage was set to levels well above the flight values. For the Cerenkov detector, the flight amplifier and high voltage supplies were also incorporated in the checkout; after balancing, the photomultiplier high voltage levels were fixed and not changed for the flight. The general procedure of the evaluation was first to infer the response per photoelectron of the system from the location, V_{α}, and full width at half maximum, W_{α}, of the peak from the alpha source, assuming purely Poisson statistics. The most probable number of photoelectrons produced for each muon, N_{pe}, was then deduced from the location of the muon peak, V_{μ}, relative to the alpha peak:

$$N_{pe} = \left(\frac{W_{\alpha}}{2.35 V_{\alpha}} \right)^{\frac{1}{2}} \frac{V_{\mu}}{V_{\alpha}} \qquad \text{(II.29)}$$

The procedure was similar for the Cerenkov detector, except that a 0.003μC, Am^{241} alpha source embedded in a NaI scintillator was used as a light source. The general results of the preflight checkout are given in table II.3, together with other miscellaneous data pertaining to the various detectors.

TABLE II.3: Detector Design and Performance

Detector	Type	Nominal Thickness (cm)	Area (cm^2)	Light Pipes Type*	Light Pipes Number	Photomultipliers Type**	Photomultipliers Number	Pulse Height Analyzers Type (Channels)	Pulse Height Analyzers Number	Pulse Height Analyzers Number Gain Ranges Each	Pulse Height Analyzers Nominal Gain Change Factors	Conversion Efficiency
D1	Pilot Y	.635	77.5 x 77.5	Adiabatic	4	7.62	4	1024	1	4	4	175 p.e. MeV^{-1}
D2	Lucite	1.270	50.8 x 50.8	Diffuse Reflecting Box		12.7	12	1024	1	4	8	10.3p.e. $muon^{-1}$
D3	Pilot Y	.635	50.2 x 50.2	Adiabatic	2	7.62	2	1024 256	1 1	4 3	4 5.85	139 p.e. MeV^{-1}
D4	Pilot Y	.953	58.4 x 55.9	Triangular-A	2	7.62	2	256	2	3	5.85	50 p.e. MeV^{-1}
D5	Pilot Y	.953	58.4 x 55.9	Triangular-A	2	7.62	2	256	2	3	5.85	50 p.e. MeV^{-1}
D6	Pilot Y	.953	58.4 x 55.9	Triangular-A	2	7.62	2	256	2	3	5.85	40 p.e. MeV^{-1}
D7	Pilot Y	3.493	59.7 x 55.9	Triangular-B	2	7.62	4	256	2	3	5.85	144 p.e. MeV^{-1}
D8	Pilot Y	3.493	59.7 x 55.9	Triangular-B	2	7.62	4	256	2	3	5.85	91 p.e. MeV^{-1}
D9	Pilot Y	3.493	59.7 x 55.9	Triangular-B	2	7.62	4	256	2	3	5.85	108 p.e. MeV^{-1}
D10	Pilot Y	3.493	59.7 x 55.9	Triangular-B	2	7.62	4	256	2	3	5.85	94 p.e. MeV^{-1}
D11	Pilot Y	3.493	59.7 x 55.9	Triangular-B	2	7.62	4	256	2	3	5.85	101 p.e. MeV^{-1}
D12	Pilot Y	3.493	59.7 x 55.9	Triangular-B	2	7.62	4	256	2	3	5.85	104 p.e. MeV^{-1}
D13	Pilot Y	3.493	59.7 x 55.9	Triangular-B	2	7.62	4	256	2	3	5.85	94 p.e. MeV^{-1}
D14	Pilot Y	3.493	59.7 x 55.9	Triangular-B	2	7.62	4	256	2	3	5.85	78 p.e. MeV^{-1}
D15	Pilot Y	.635	50.8 x 50.8	None		7.62	1	None				

*Adiabatic Light Pipes are of plastic finger variety; Triangular-A refers to pyramidical design going from a face 1.02cm x 32.3 cm to one 5.84cm x 5.84cm in a distance of 22.86cm; Triangular-B goes from 3.25cm x 32.3cm to 6.99cm x 6.99cm in a distance of 14.4cm.

**7.62cm photomultipliers are RCA 4524, 12.7cm photomultipliers are RCA 4525.

ORIGINAL PAGE IS OF POOR QUALITY

c. Detailed Description of Detectors

The D1 scintillator was included primarily for triggering purposes. Its size was made significantly larger than the other scintillators in order to increase the effective geometry of the scintillator-Cerenkov telescope (D1-3) for measuring the charge composition of non-stopping particles. Because of this large size, it was occasionally possible to trigger the experiment with particles which did not pass through the spark chamber, which was only 50.8 cm x 50.8 cm. Such events were discarded in the analysis. The D1 scintillator was made as thin as possible (0.635 cm) in order to minimize the amount of matter above the totally active stack of scintillators, D3-14. This was balanced with the necessity to have a reasonable level of resolution (dominated by Landau fluctuations) for triggering the experiment.

The Cerenkov radiator, D2, is a sheet of acrylic plastic 1/2" thick. It is enclosed in a box painted with diffuse reflecting white paint, and viewed through the sides of the box.

The Cerenkov detector is followed by a digitized spark chamber consisting of eight decks 1.27 cm apart (Ehrmann et al., 1967). Each deck consisted of one x and one y plane of 200 wires each. The wires, spaced 0.254 cm apart, where threaded through magnetic cores whose polarity could be reversed by a current pulse in the wire. The set cores were read out using the pulse induced in a second wire when the cores were reset through a third wire. The spark chamber was used to determine the pathlength of a particle in a given detector, to correct the data for positional variations in the response and thickness of the detectors, and also to predict the point at which a particle would exit from the totally active stack, D3-14, assuming it did not stop. The latter was

essential in determining whether or not a given particle had actually stopped in the experiment. The spark chamber was also useful in rejecting background, which appeared as multiple tracks (Arens et al. 1974); events which gave no track were also discarded. Both the spark chamber windows and the Cerenkov light diffusion box were constructed of aluminum sheets 0.124 g/cm^2 thick.

The D3 scintillator is primarily a trigger scintillator. However, it also serves as the first element of the totally active stack of scintillators D3-14, and is especially useful for particles of low energy which do not penetrate very far into the stack. Its size is the same as the active area of the spark chamber, and thus is somewhat smaller than the other scintillators. This helped the experiment to trigger on particles which had actually passed through the spark chamber. D3 was made fairly thin in order to maximize the number of detectors penetrated by low energy particles before stopping, thus maximizing the information available for the analysis. The limiting factor is again the role of statistical fluctuations, together with the physical requirement that the experiment should not have large gaps of empty space between detectors (which would drastically decrease the geometric factor).

The three thin scintillators, D4-6, are slightly thicker than D3 in order to minimize empty space between detectors; However, they are still sufficiently thin to give multiple data points for low energy particles. D4-6 have dimensions somewhat larger than D3 in order to increase the geometric factor as much as possible within the limitations imposed by the size of the spark chamber, which is fixed.

The thick scintillators, D7-14, are intended to extend the sensitivity of the instrument to higher energy particles. Although

detectors D7-14 are much thicker than the other scintillators, they are still sufficiently thin to provide significant information in the critical region near the end of a particle's range where $\frac{dE}{dx}$ is rapidly changing.

The anticoincidence scintillator, D15, is included to give some indication of whether or not a particle has stopped in D14; without it, D14 is reduced to an anticoincidence scintillator for D13. Particles were defined to have stopped in D14 if, and only if, their trajectories passed through D15 and D15 gave no response.

d. Light Pipes

There are two types of light pipe used in the experiment. Adiabatic, plastic finger light pipes were used with D1 and D3 in order to maximize light collection efficiency for these two very thin scintillators. For D4-14, triangular light pipes were used. Their shapes were determined by connecting the edge face of a given scintillator to a rectangle 7.62 cm high (determined by the diameters of the photomultiplier faces) by four planar surfaces. They were made as long as possible (within the constraint that they fit into the gondola) in order to maximize their efficiency. They were of two general types, as described in table II.3. Each type was compared with the adiabatic light pipes and found to have about half the collection efficiency of the adiabatic pipes. On the other hand they were much less costly to construct. The main problem connected with the use of these light pipes was a rapid variation in collection efficiency near the junction of the two pipes, which was corrected in the data reduction. These light pipes also resulted in some problems during the balancing of the photomultiplier high voltages due to geometrical asymmetries present in the design.

e. Coincidence Requirements

A schematic of the logic used in triggering the experiment is shown in figure II.11. As can be seen, the experiment was designed to trigger in four separate modes: the isotope mode (for stopping particles), the Cerenkov mode (for heavy particles penetrating D1-3), the penetrating mode (for events to be used in mapping positional and temporal variations in detector response) and the calibration mode (for use in normalizing the responses of the various detectors). The criteria required for triggering in each of these modes are given in table II.4.

Most events triggered the experiment in the isotope mode. This was the primary triggering mode for the experiment, and was intended to detect particles heavier than helium which stopped in the experiment. Since ionization energy loss decreases with increasing range, this mode was designed to require lower thresholds on D1 for particles of longer ranges. These thresholds were set to reject He (which would otherwise have swamped the experiment) while accepting as much Li as possible, with no rejection of Be.

Of the other modes, the Cerenkov mode was intended as a separate experiment to measure the charge composition using detectors D1-3, while the penetrating and calibration modes were intended to provide calibration data for calibrating the various data and removing systematic errors. The calibration mode failed to operate properly in the experiment, and so provided no useful information.

f. Pulse Height Analysis

There were two types of pulse height analyzers used in the experiment. All used automatic gain switching in order to obtain the required dynamic range of $\sim 10^5$. Detectors D4-14 each had two 256 channel analyzers with synchronous clocks and three gain ranges each. The

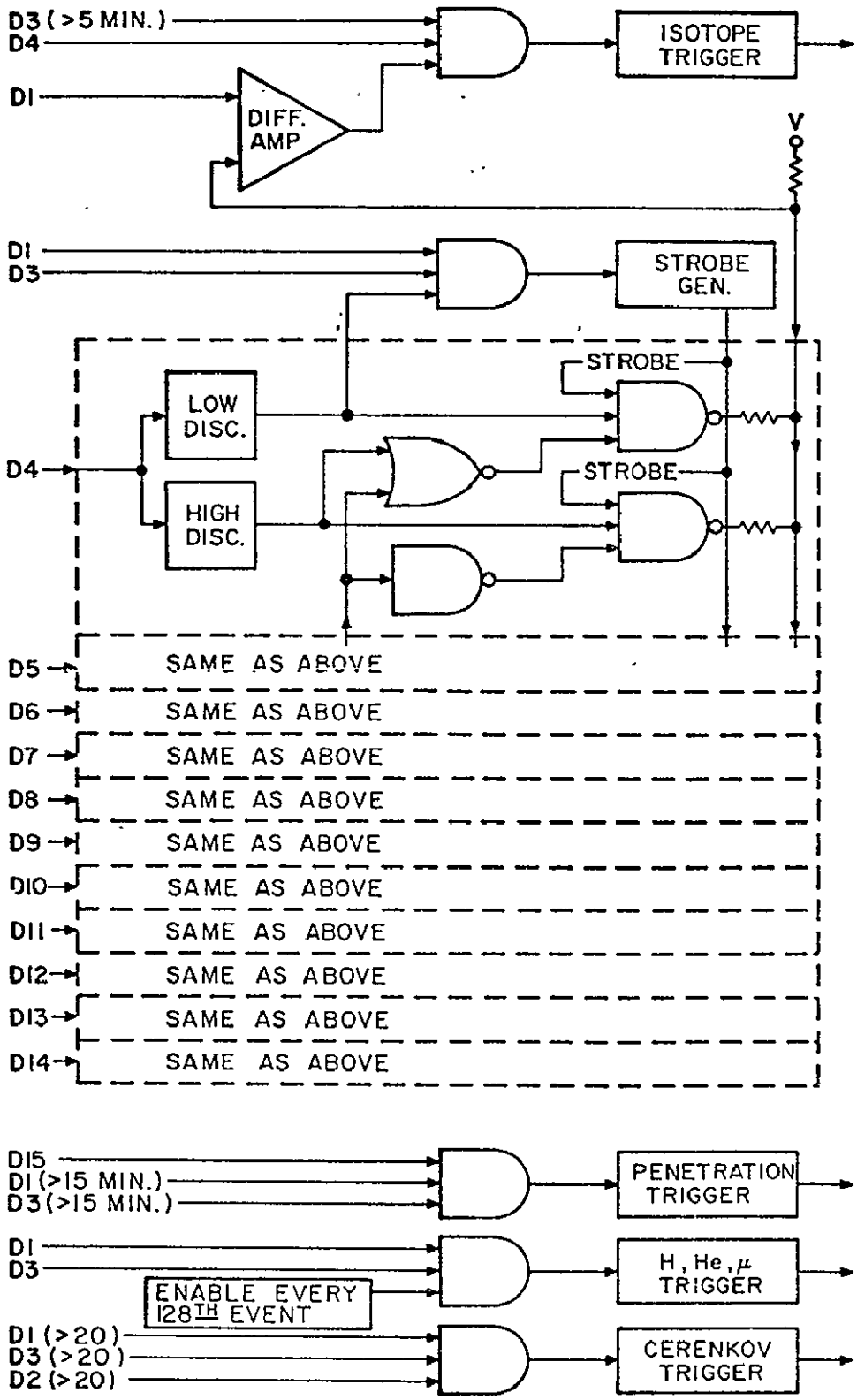

Figure II.11. Schematic illustration of triggering logic used for the experiment.

ORIGINAL PAGE IS
OF POOR QUALITY

TABLE II.4

TRIGGERING THRESHOLDS (in channel numbers)

	Isotope Mode		Penetrating	Cerenkov	Calibration	
	Low	High	Mode	Mode	Mode	Muons*
D1			81	147	1.5	6.0
D2				(165)		5.5
D3	41		106	185	3	7.5
D4	2	21				1.07
D1	272	248				
D5	2	23				0.89
D1	234	222				
D6	4	21				0.92
D1	211	204				
D7	12	137				5.25
D1	195	173				
D8	11	133				4.82
D1	164	150				
D9	12	144				5.25
D1	143	133				
D10	9	107				3.73
D1	131	125				
D11	9					3.73
D1	120					
D12	8					3.56
D1	114					
DI3	10					3.88
D1	108					
D14	9					4.18
D1	103					
D15			0.25xMin			

*Best estimate using x10 amplifiers for D4-14

gain ranges of the two pulse height analyzers on a given detector were overlapping, thus permitting an accurate calibration of gain factors and zero offset from in flight data. D1-3 used 1024 channel analyzers with asynchronous clocks and four gain ranges each. D3 also was analyzed by a 256 channel analyzer, which was included primarily for the extra thresholds it provided for triggering purposes; however, it also served as a partial check on the 1024 channel analyzer. A schematic diagram of the pulse height analysis strategy is given in figure II.12.

6. Flight. The experiment was flown by balloon from Thompson, Canada, on August 15, 1973, at 5:04 a.m, local time. Data was received at Thompson and Ft. McMurray. The payload floated at altitudes between 3.5 and 5 g cm^{-2} residual atmosphere for ~ 22 hours and was cut down at 7:00 a.m. on August 16.

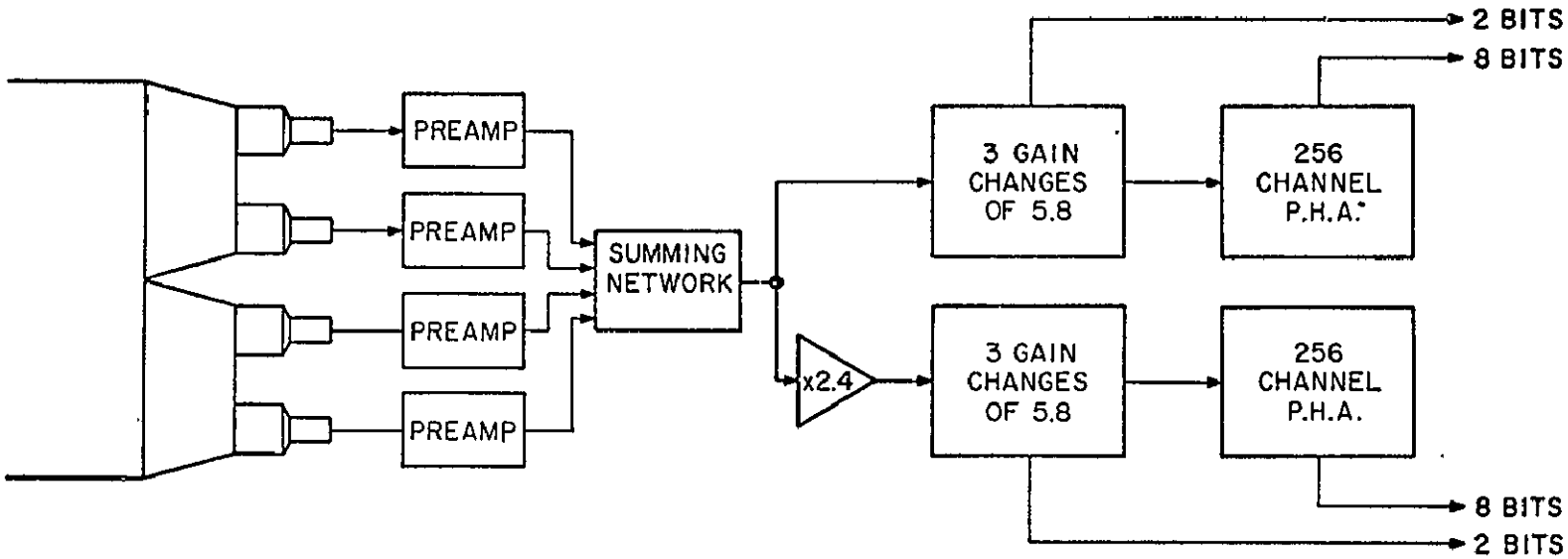

Figure II.12. Pulse height analysis strategy for detectors D7-14.

CHAPTER III

DATA ANALYSIS

A. Formulation of Response

The differential response of detector i to a particle of charge Z, mass A and velocity β is given by the relation

$$\frac{d}{dx}\left[{}^{A}_{Z}L(\beta)\right] = {}^{A}_{Z}\left[\frac{dE}{dx}(\beta)\right] {}^{A}_{Z}\left[\frac{dL_i}{dE}(\beta)\right] M_i(\vec{r}_i, t) \qquad \text{(III.1)}$$

where the factor M describes the variation in response with position ($\vec{r}_i$) and time (t) for detector i, and $\frac{dL}{dE}$ represents the efficiency with which energy lost by the particle in detector i is converted to signal. Here it is assumed that the systematic variations in response with time and position in a detector (represented by M_i) may be separated from the dependence on parameters (i.e. Z, A and β) which characterize the particle itself. We will also assume that $\frac{dL}{dE}$ is independent of mass and detector number. Although this latter assumption (namely, independence of detector number) is not justified on a broad scale, it is a satisfactory approximation for the particles of charge $4 \leq Z \leq 7$ with which we will be exclusively concerned in this thesis, as will be shown later. Finally, since the detectors are in general quite thin with respect to their horizontal dimensions, any dependence of M_i on $\vec{r}_i \cdot \hat{e}_z$ (and consequently also on the zenith and azimuthal angles, θ and $\emptyset$, respectively) can be neglected. If R_i is the particle's range (as measured from the top face of detector i), then the pulse height measured by the detector is

$${}^{A}_{Z}H_i(\beta) = M_i \int_{R_i - T_i \sec\theta}^{R_i} dR' \, \frac{dE}{dx} \, \frac{dL}{dE} \qquad \text{(III.2)}$$

where $T_i(\vec{r}_i) \cong T_i({}_{\perp}\vec{r}_i)$ gives the detector thickness as a function of

position, ${}_{\perp}\vec{r}_i$, in its central horizontal plane. For a relativistic particle, this becomes

$$H_i(\beta \to 1) = M_i T_i \sec\theta \frac{dE}{dx}(\beta \to 1) \frac{dL}{dE}(\beta \to 1) \tag{III.3}$$

which is the basic relation used for calibration and mapping of positional and temporal variations.

The response of the Cerenkov detector may be characterized in a similar fashion. The differential response is given by

$$\frac{d}{dx} L_2 = M_2 C T_2^{-1} \tag{III.4}$$

with

$$\overset{A}{Z} C(\beta) = \left(\frac{Z^2}{\underline{n}^2 - 1}\right)\left(\underline{n}^2 - \frac{1}{\beta^2}\right) \tag{III.5}$$

for a Cerenkov radiator with index of refraction, $\underline{n}$. Analogous to the case for scintillators, we have

$$H_2 = \int_{R_2 - T_2 \sec\theta}^{R_2} dR' M_2 C T_2^{-1} \tag{III.6}$$

and

$$H_2(\beta \to 1) = Z^2 M_2 \sec\theta \tag{III.7}$$

The pulse heights, H_i, are of course statistical quantities. As such they are characterized by distribution functions rather than unique values. These distribution functions are determined by both physical and instrumental factors. For example, important contributions come from Landau fluctuations in the production of delta rays and Poisson fluctuations in the conversion of scintillator light to photoelectrons in the photomultiplier. All distribution functions are (for convenience,

and unless otherwise noted) approximated by Gaussian distribution with widths characterized by their standard deviation, σ. Furthermore, these distributions are all assumed to be statistically independent (again, unless otherwise noted).

The pulse height ${}^{A}_{Z}H_i(\beta)$ represents the signal (light) observed in detector i by a particle of charge Z, mass A and velocity β at the top of the detector. Because of the large dynamic range required (typically $\sim 10^5$), this was analyzed by a pulse height analyzer with dynamic gain switching. There were two types of pulse height analyzer used: D4-14 were each analyzed by two 256 channel analyzers using three gain ranges each, while D1-3 were analyzed by 1024 channel analyzers using four gain ranges each; D3 was also analyzed by a 256 channel analyzer. Since each gain range can be regarded as a separate pulse height analyzer with its own gain and zero offset, the pulse heights H_i are related to the raw channel numbers, H'_{ij}, (where j denotes the gain range) according to

$$H_i = a_{ij}\left(H'_{ij} + b_{ij}\right) \qquad \text{(III.8)}$$

The determination of the a_{ij} and b_{ij} is discussed in detail in Appendix A, and so will only be briefly sketched here. The a_{ij} and b_{ij} were all determined by terms of a_{i1}, and b_{i1} by use of the overlapping gain ranges of the two different pulse height analyzers analyzing a given detector. In cases where there was only one pulse height analyzer, $b_{ij} = 0$ was assumed, and the a_{ij} were determined in terms of a_{i1} by comparing the cut-out channel of a given gain range with the cut-in channel of the next gain range (these should both correspond to the same pulse height). Alternatively, when two pulse height analyzers analyzed the same detector, both the a_{ij} and b_{ij} could be determined in terms of the a_{i1} and b_{i1} by

plotting one pulse height analyzer against the other. Next, the a_{i1} and b_{i1} were all determined in terms of a_{41} and b_{41} using semirelativistic particles (i.e. particles incapable of producing knock-on electrons of long range which might couple one detector to another, yet sufficiently fast that they did not slow down significantly in traversing a detector). Finally, $b_{41} = 0$ was assumed, and a_{41} was determined to give reasonable pulse heights for relativistic particles (i.e. $\sim Z^2$ in x minimum units).

In addition to the pulse height analyzer gain and zero offset factors (a_{ij} and b_{ij}), the factor M_i (which describes positional and temporal variations in response) must also be determined. $M_i(\vec{r}_i,t)$ has been assumed to be separable:

$$M_i(\vec{r}_i,t) = M_i^P(\vec{r}_i)\, M_i^T(t) \tag{III.9}$$

Here the mapping function, M_i^P, depends only on position and the drift function, M_i^T, depends only on time. Both M_i^P and M_i^T are normalized to unity in order to preserve detector normalizations. The functions M_i^P and M_i^T were determined by observing variations in detector response to relativistic C and O nuclei. M_i^P was approximated by an 11x11 polynomial with the 121 coefficients determined by a maximum likelihood fit. M_i^T, on the other hand, was approximated by the least squares spline technique (Thompson 1973).

Finally it was necessary to know the thicknesses of the various detectors as a function of position. This was accomplished by caliper measurements of each detector on a 5 cm grid.

B. Preliminary Selections

In the preceding section, the reduction of the raw data to a form essentially independent of the idiosyncracies of this particular experiment

has been discussed. The data must now be analyzed in a manner capable of achieving elemental and isotopic resolution. This has been approached in different ways for various subsets of the data: For very high energy events ($E \geqslant 570$ MeV/nuc), only the elemental abundances have been derived using a Cerenkov versus scintillator analysis based on detectors D1-3. The elemental abundances resulting from this analysis are shown in figure III.1. Events which stop in D3-14, and yet are above the Cerenkov counter threshold (i.e. $\beta \geqslant 0.67$) are subjected to an isotopic analysis based on the Cerenkov and range measurements. This has the unique advantage of not requiring the determination of any peculier response functions--the interdependence of Cerenkov response and the range of a particle are well known. This approach is particularly effective for the heavier particles with $Z \geqslant 8$. Finally, particles which stop in D3-14 and have $4 \leq Z \leq 7$ have been subjected to a light versus range analysis. The restriction on the charge of the particles analyzed is imposed by triggering thresholds from below, and from above by the non-uniform response functions of the Pilot Y scintillators used in the experiment. This thesis will be concerned exclusively with this mode of analysis, which is described in detail in section B of the present chapter.

The data analysis begins with the isolation of a relevant subset of the data, which is defined by the following criteria.

Only events stopping in detectors D5-13 are included in the analysis. A particle is said to have stopped in a given detector if that detector produces the last nonzero pulse height observed and the extrapolated spark chamber track exits from the stack at a point deeper than halfway through the following detector. Events stopping before D5 suffer from reduced resolution due to the minimal number of detectors penetrated.

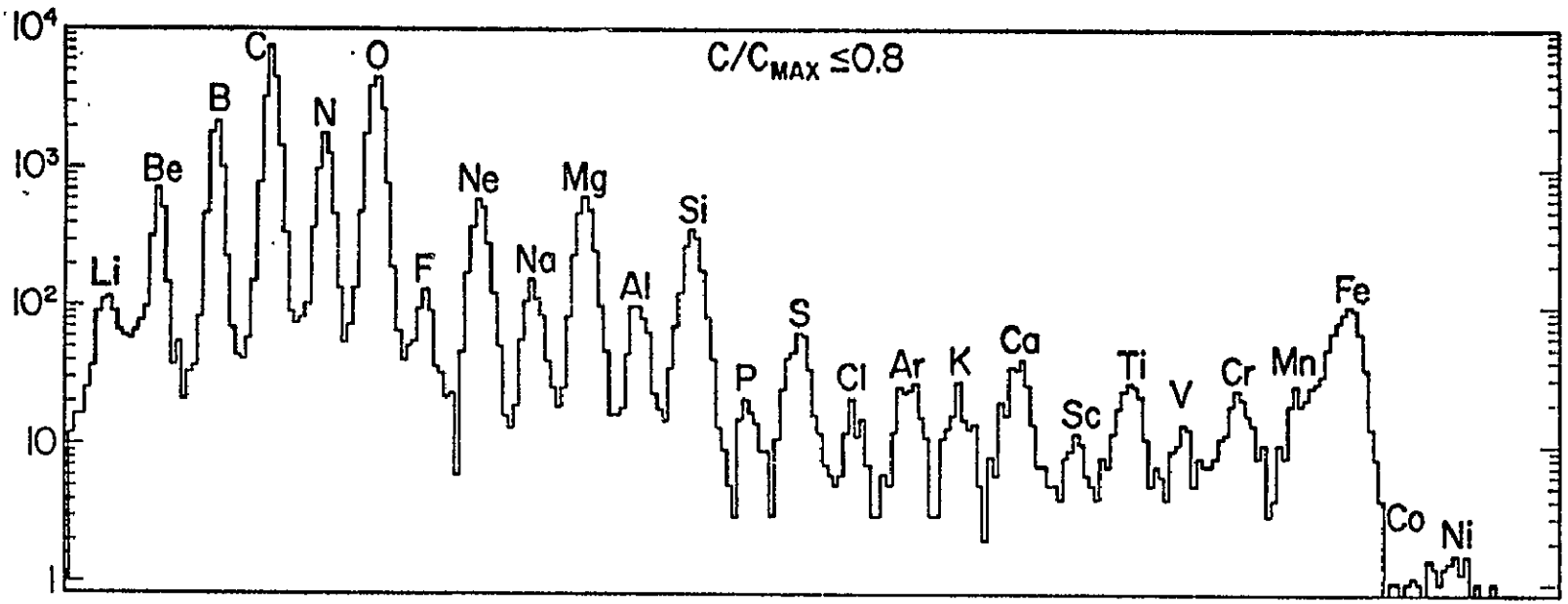

Figure III.1. Elemental abundances from Cerenkov versus scintillator analysis.

D14, on the other hand, suffers from noise from the spark chamber in one of its pulse height analyzers. In addition, it is not always possible to determine whether a particle has stopped in this detector due to the reduced size of the anticoincidence scintillator, D15.

No events producing either no track or more than one track in the spark chamber are included. An acceptable track must include discharges in at least five of the eight spark chamber decks in the x and y views.

"Obviously interacting" events were excluded. These were identified by examining the sequence of pulse heights in detectors D3-14. Events with pulse heights more than 15% less than the average of the pulse heights from the preceding two detectors (excluding the Cerenkov, D2) or more than 30% less than the pulse height from the immediately preceding detector were excluded unless the pulse height in question corresponded to the detector in which the particle stopped.

Finally, events were discarded in which the pulse heights from two pulse height analyzers analyzing the same detector did not agree to within one channel equivalent of the smaller of the two pulse heights.

C. R x L Mode of Analysis

The R x L mode of analysis (with which we are exclusively concerned here) is based upon a presentation of the response of the totally active stack of scintillators in terms of the variables L_i (total light observed in and after detector i) and R_i (range of particle measured from top of detector i). In doing this, the implicit assumption that the detectors all have identical response functions, $\frac{dL}{dE}$, has been made in order to allow the interpretation of L_i as a simple sum of pulse heights in different detectors. As has been observed previously, this assumption is not generally valid, and is a suitable approximation only

over a limited range of incident particles such as that ($4 \leq Z \leq 7$) with which the present analysis is exclusively concerned. As an example, the responses of the various detectors to relativistic particles of various charges are tabulated in table III.1. Ideally each detector should show the same response to the same incident particle in this table. As can easily be seen, however, this is not the case, and indeed cannot be the case over the entire range of charges for any choice of detector normalizations. However, for the restricted range of particles considered here, the effect is 1%. The R x L mode of analysis offers important advantages due to the scaling of the fundamental parameters L_i and R_i in mass. It is an intuitively straight forward approach, which still offers the advantages of a multiparameter analysis for testing the internal consistancy of events in order to identify and eliminate background. The R x L analysis is very similar to the R x E analysis which was discussed in Chapter II. Its fundamental concepts are illustrated in figure III.2, which depicts its application to an actual ^{9}Be event. In figure III.2A, the event is shown incident on the experiment at a zenith angle of 29°, and stopping in detector D11. The analysis of this event will now be described in detail in the following subsections.

1. <u>Estimation of Range</u>. As is shown in the lower half of figure III.2A, one first adds the various pulse heights to obtain several values of L_i (one for each detector penetrated) as a function of detector number. Insofar as detector numbers may be related to depth in the stack, this is already a crude R x L representation. As we have seen in Chapter II, however, this estimate must be considerably refined if we are to have isotopic resolution. The refinement of the range estimate obviously depends upon a determination of the range in the last detector

TABLE III.1

Responses of Detectors D1 and D3-11 to Relativistic

Particles of Various Charges (xMinimum Units)

	D1	D3	D4	D5	D6	D7	D8	D9	D10	D11
Be	14	15	15	15	15	14	14	14	14	14
B	22	22	22	22	22	22	22	21	21	22
C	30	30	30	30	30	30	30	30	30	30
N	40	40	40	39	39	40	39	39	39	39
O	50	49	50	50	49	49	49	49	49	49
Ne	73	70	74	72	72	72	72	72	72	73
Mg	96	92	97	96	96	95	96	96	97	98
Si	122	116	125	125	123	120	121	122	122	126
Fe	324	310	358	368	358	316	349	318	328	338

ORIGINAL PAGE IS
OF POOR QUALITY

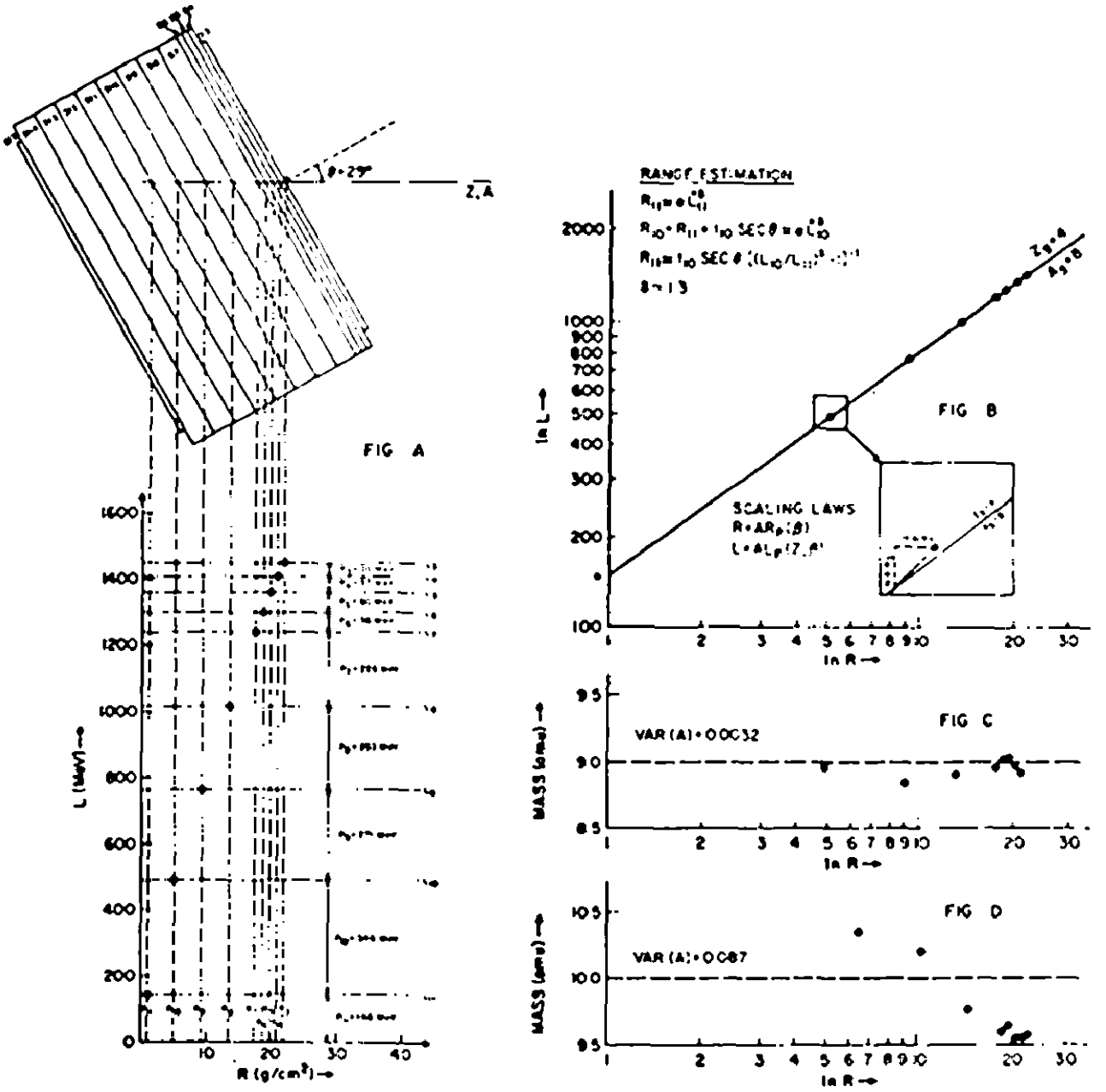

Figure III.2. Schematic illustration of range versus total light analysis.

(in which the particle stops), R_{last}. Even without such an estimate, however, there is a certain subclass of particles for which the range is fairly well known, namely those which stop near detector boundaries. Such particles may be identified by looking for (relatively) very small pulse heights in the last detector penetrated by stopping events, i.e. $L_{last} \rightarrow 0$. For such events (depending upon the limits put on L_{last}) R_{last} may be made arbitrarily small and, consequently, negligible compared to detector thicknesses (which are added to it in the analysis). Of course, the tightness of this selection must be balanced with the statistical weight of the resultant subset of the data. Figure III.3 shows the result of plotting such a subset of the data on what amounts to a rotated ln L versus ln R plot (i.e. the dependent and independent variables have been chosen as linear combinations of ln L and ln R such that the response curves are nearly horizontal). As can be seen, the detector response is well approximated by a power law of the form

$$R_i = \alpha L_i^{\delta} \tag{III.10}$$

where $\delta \simeq 1.3$ is a constant, and $\alpha(Z,A)$ does not depend on velocity. By writing this equation again for the next to last detector penetrated, the parameter $\alpha(Z,A)$ may be eliminated. One may then use the relation

$$R_{last-1} = R_{last} + T_{last-1} \sec\theta \tag{III.11}$$

to obtain the result

$$R_{last} = T_{last-1} \sec\theta \left[\left(\frac{L_{last-1}}{L_{last}} \right)^{\delta} - 1 \right]^{-1} \tag{III.12}$$

from which it is possible to estimate the range of a particle in the last detector with no a priori knowledge of its charge or mass. The derivation

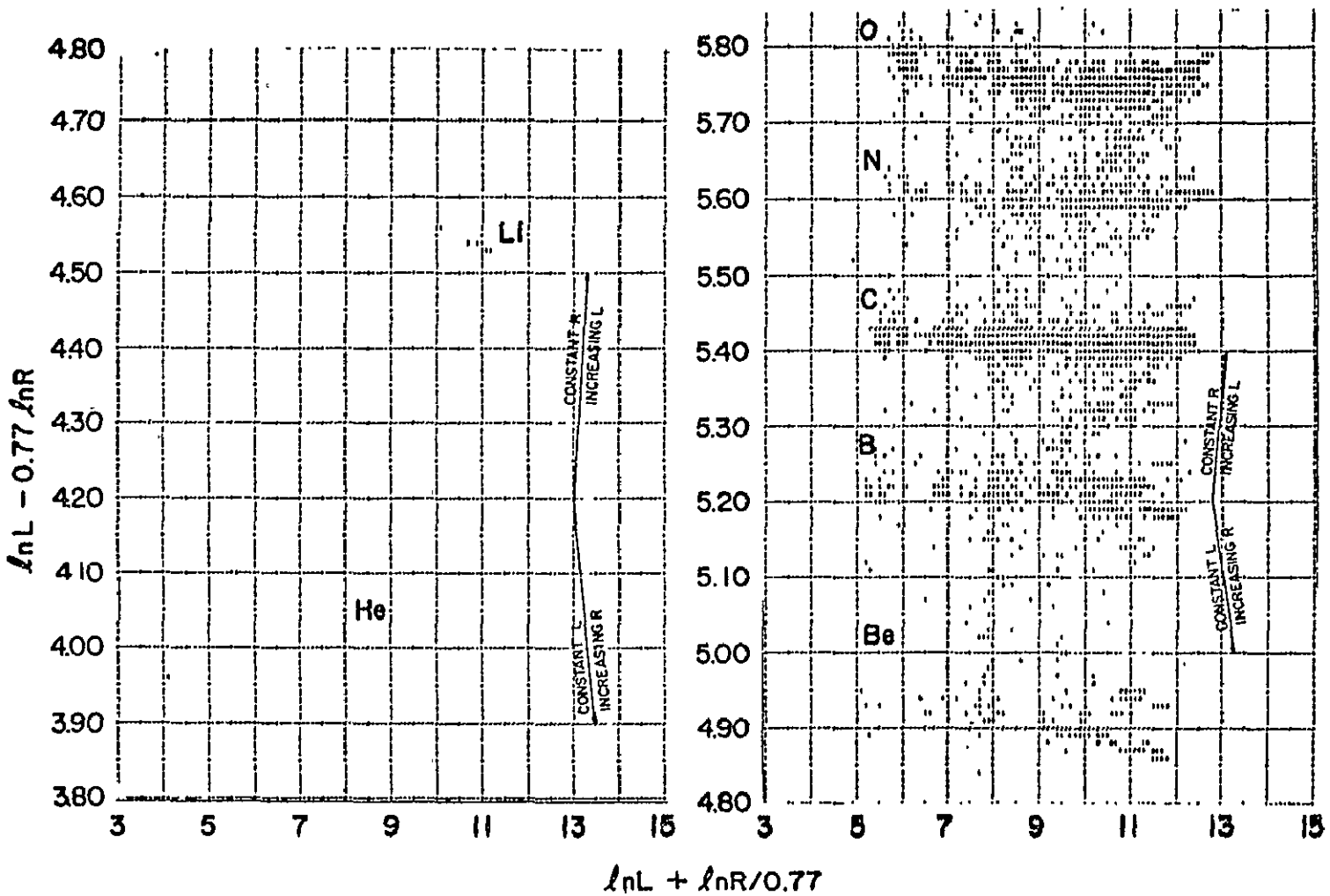

Figure III.3. Rotated light versus range plot for particles stopping near detector boundaries.

of this relation requires only that the (integral) response of the last two detectors to a given particle be characterized by identical power laws of the form III.10. This assumption appears to be justified at least for $4 \leq Z \leq 7$ and

$$R_{last} \gtrsim T_4 = 0.983 \ g\,cm^{-2} \tag{III.13}$$

where easy experimental checks are possible (see figure III.3). For particles of shorter range, this dependence must then be extrapolated.

From a strictly mathematical point of view, it is possible to extract some information on the detector response, even for $R < T_4$. Essentially, this would be done by requiring

$$\begin{aligned} R_{last} &= \alpha L_{last-1}^{\delta} - T_{last-1} \sec\theta \\ &= T_{last-2} \sec\theta \left[\left(\frac{L_{last-2}}{L_{last-1}} \right)^{\delta} - 1 \right]^{-1} - T_{last-1} \sec\theta \end{aligned} \tag{III.14}$$

which is based entirely on observables. This would be useful as a cross check on the reliability of the range estimation procedure. However, both terms in III.14 are generally larger than their difference, with the result that the accuracy suffers. For this reason, and statistical limitations imposed by the amount of data available, it is not possible to use equation III.14 to meaningfully extend the checks on equation III.12. An attempt to compare the predictions of equations III.14 and III.12 is shown in figure III.4.

2. <u>Standard Curves</u>. Having determined R_{last} to first order, all of the available data may be presented on a diagram similar to that of figure III.3. This is shown in figure III.5. From this figure, one sees that there is a very clear separation of the various charges. However,

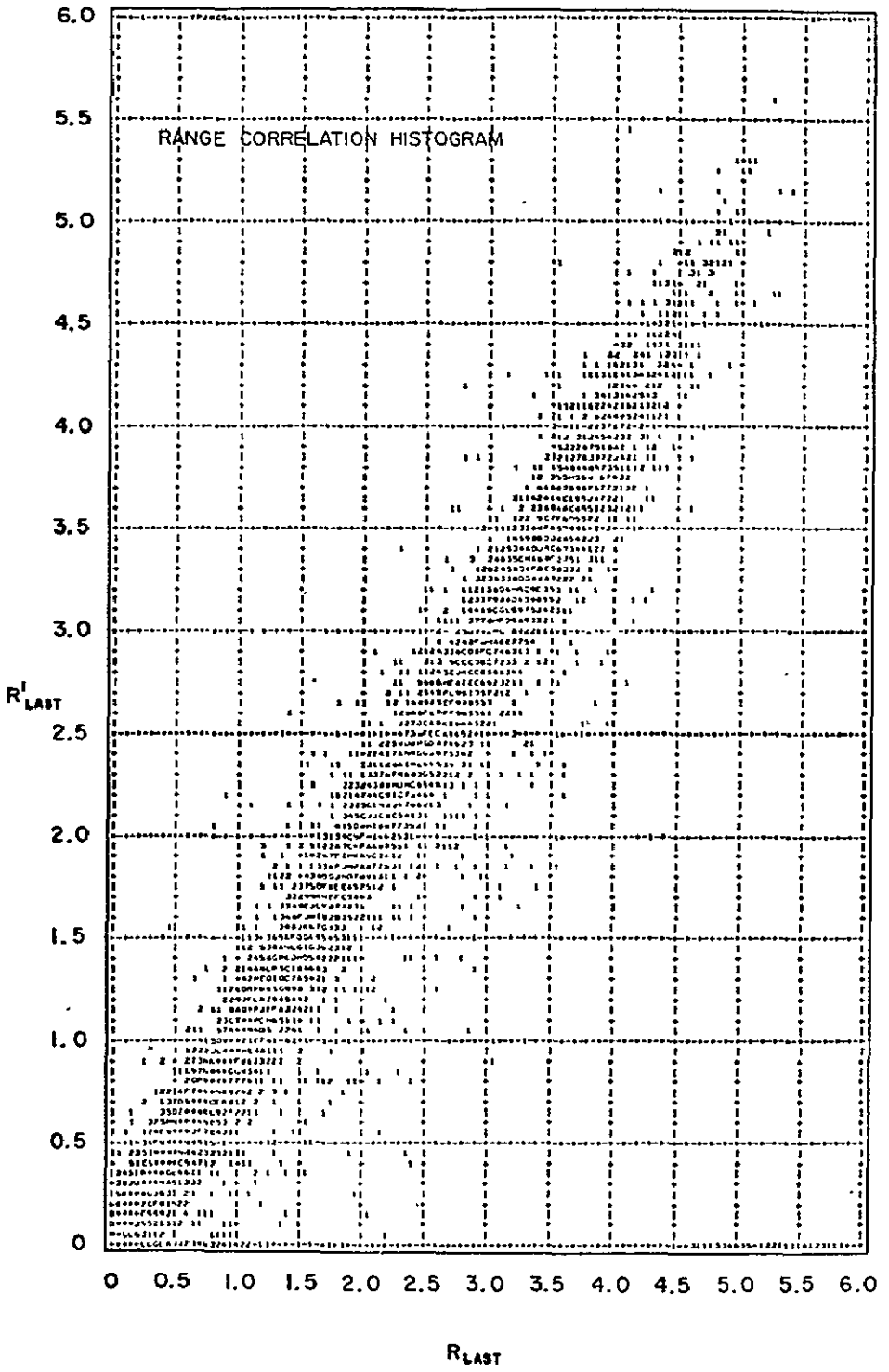

Figure III.4. Range in the last detector as determined from last three detectors (last two considered as one) versus that determined from last two detectors penetrated.

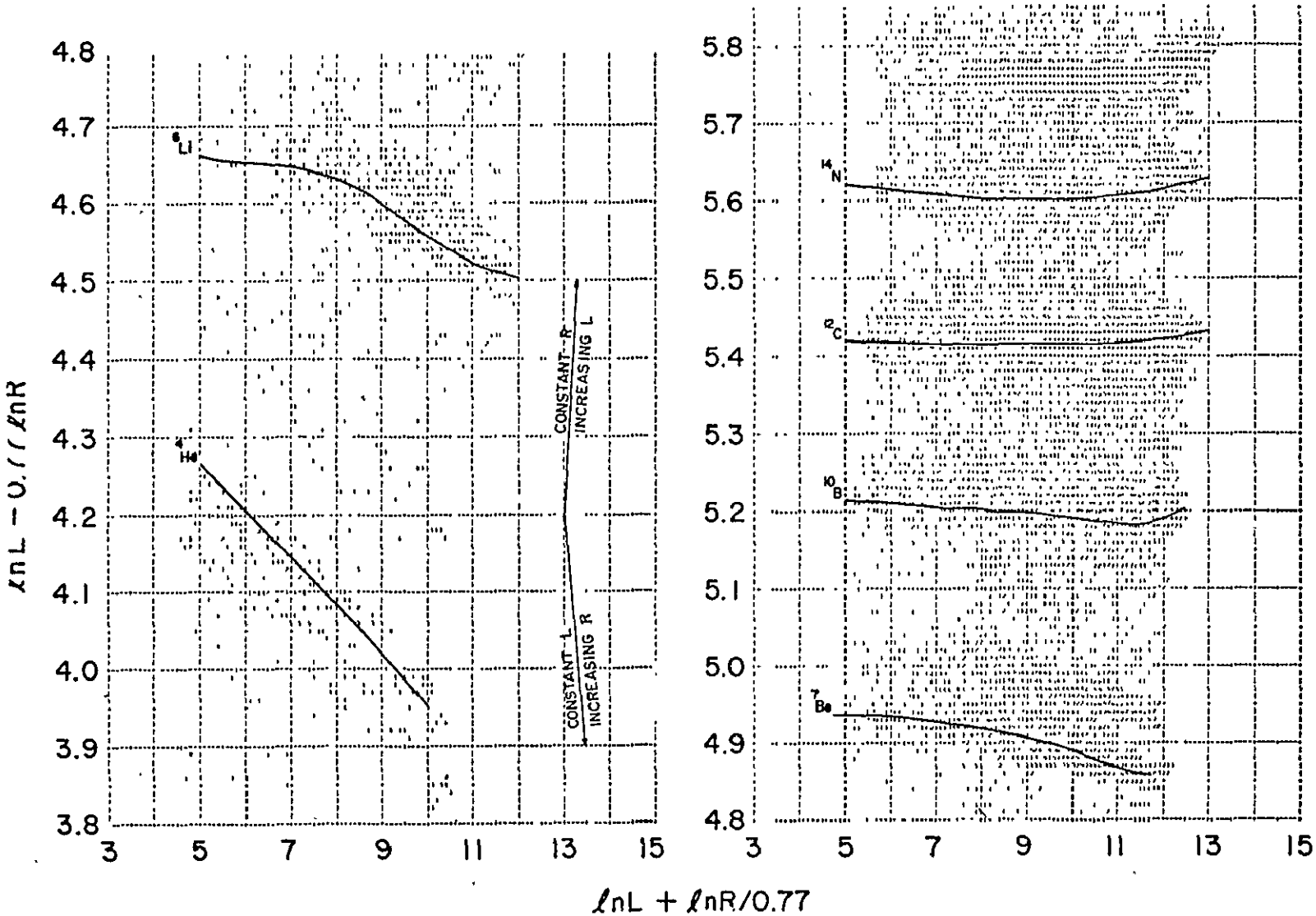

Figure III.5. Rotated light versus range plot for unselected data with standard response curves sketched in.

mass separation is apparent only for $Z \leqslant 3$ and ^{7}Be. In particular, the important isotope, ^{10}Be, is not clearly separated from ^{9}Be, and the problem gets worse for heavier isotopes. Since the response function $\frac{dL}{dE}$ is independent of the particle mass (A) while depending on both charge and velocity, it should be sufficient to determine $\frac{dL}{dE}$ for a single isotope of each element, and then extend the result to the remaining isotopes. This will be discussed later in more detail.

The standard response functions L(R) are obtained by averaging over the widths of the distributions in figure III.5 along the ordinate. Where at least one isotope of a charge group is clearly separated, only data pertaining to the most abundant such isotope is used. Where no isotope is clearly separated (i.e. for $Z \geqslant 5$) all of the data for a given element are treated as if pertaining to a single isotope. This does carry with it certain difficulties. For instance, the density of experimental points along a given response line in figure III.5 is a complicated function of spectral characteristics and the geometry of the telescope. In reality, the vertical contours used to locate the standard response curves are probably not always normal to the gradient in the density of experimental points. It is thus probable that there are <u>small</u> systematic errors in the determination of the standard response curves for elements with significant abundances of more than one unresolved isotope. The effect is most important for B and N (which do not exhibit a single, dominant isotope), and does not apply to Be at all since the Be response curve is based on the well separated ^{7}Be data. Presumably, it can be corrected by an iterative approach if the initial approximations to the response lines are sufficiently close to reality. However, this has not been attempted in the present analysis.

The standard response curves which have been adopted are shown in figure III.5, together with the nominal masses assigned to them. The precise masses to which they correspond will be determined later in the analysis. In the particular case of B, the response curve has been shifted somewhat (according to rules to be developed in the following section) to correspond more closely to the isotope ^{10}B. These same standard response curves are presented in figure III.6 in the form of integral response (saturation) as a function of velocity by use of the range energy tables. Also shown are the corresponding differential response functions.

3. Mass Determination. In order to apply the standard response lines to the data, use is made of two fundamental scaling laws. The first,

$$ {}^{A}_{Z}R(\beta) = A\,{}^{1}_{Z}R(\beta) \tag{III.15} $$

is a restatement of equation II.4, while the second,

$$ {}^{A}_{Z}L(\beta) = A\,{}^{1}_{Z}L(\beta) \tag{III.16} $$

is analogous to equation II.1. Its validity is equivalent to the assumption that the differential scintillator response function, $\frac{dL}{dE}$, is independent of the mass of the ionizing particle (see equation II.3). This is reasonable, at least to first order, since the medium sees only the charge of the incident particle. For Coulomb collisions with atomic electrons, the mass of the projectile (assumed to be an atomic nucleus) is relatively very large and does not significantly affect the energy transferred to the knock-on electrons or the number of collisions per unit pathlength which are the two fundamental parameters involved in the

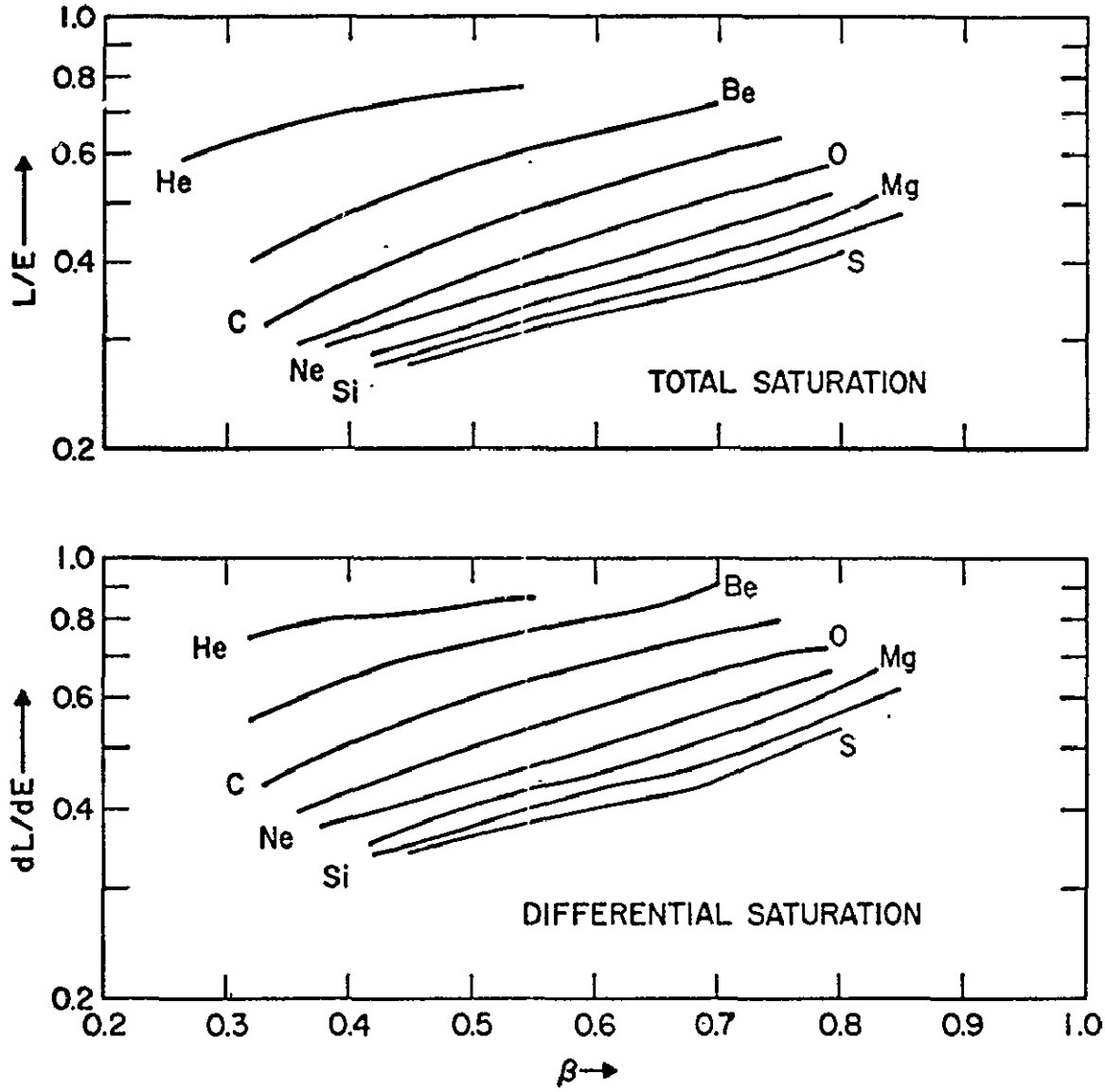

Figure III.6. Integral and differential saturation as functions of velocity as derived from standard response curves.

problem (Rossi 1952). The most plausible objection to this scaling would be to note that saturation (i.e. the departure from unity of the scintillator response, $\frac{dL}{dE}$, is a macroscopic phenomenon (which is not well understood) rather than a microscopic one (Meyer et al. 1962). The suggestion is then that one should take account of the fact that a particle of smaller mass slows down more in traversing a macroscopic distance (~ the dimension of a "typical luminescense center") than one of greater mass and identical initial velocity. Thus the lighter particle will deposit slightly more energy and the scintillator response may be more highly saturated. Essentially, the condition for this effect to be negligible and the scaling given by equation III.16 to hold is

$$\frac{\mu}{R} \ll \left[\frac{d\ln\left(\frac{L}{E}\right)}{d\ln R}\right]^{-1} \gtrsim 3 \qquad \text{(III.17)}$$

where the second inequality results from the power law approximation to the range energy relation (equation II.22) and the response curves given in figure III.6. As an upper limit, we may take μ to be a characteristic dimension for luminescence centers. A better upper limit, μ', would be the magnitude of the range discrepancy which develops when two particles, of the same charge and velocity but differing mass, traverse a distance equivalent to the characteristic dimension of a luminescence center, μ:

$$\mu' = \left| \frac{A_1}{Z} R(\beta_1) - \frac{A_2}{Z} R(\beta_2) \right| \qquad \text{(III.18)}$$

Here β_1 and β_2 are given by

$$\mu = \frac{A_1}{Z} R(\beta_0) - \frac{A_1}{Z} R(\beta_1) = \frac{A_2}{Z} R(\beta_0) - \frac{A_2}{Z} R(\beta_2) \qquad \text{(III.19)}$$

and β_o is the initial velocity of both particles. In any case, the inequality III.17 is easily satisfied for any realistic values of the relevant parameters. A more detailed experimental and theoretical investigation of the phenomenon of scintillator saturation has been given by Taylor et al. (1951), Meyer et al. (1962), Katz et al. (1968), Kobetich et al. (1968).

The analysis now proceeds to figure III.2B. Using the scaling law given by equations III.15 and III.16, we obtain

$$\ln {}^{A}_{Z}R(\beta) = \ln {}^{A_s}_{Z}R(\beta) + \ln\left(\frac{A}{A_s}\right) \tag{III.20}$$

Similarly,

$$\ln {}^{A}_{Z}L(\beta) = \ln {}^{A_s}_{Z}L(\beta) + \ln\left(\frac{A}{A_s}\right) \tag{III.21}$$

Thus, on the log log plot of figure III.2B, the curve corresponding to variable mass with fixed charge and velocity is a straight line of slope 1. Furthermore, the distance between an experimental point (mass A) and the standard response line (characterized by mass A_s) along such a (slope 1) curve is just $\sqrt{2}\ln \frac{A}{A_s}$. In this way, a mass can be defined for each experimental point. This, of course, depends upon a priori knowledge of the charge of the particle; however, as is apparent from figure III.5, the charge determination is straight forward. Should the charge not be well defined, one would simply compute a mass for each possible charge, then select the charge for which the various mass estimates are most consistent. Finally, since the points (L_{last}, R_{last}) and (L_{last-1}, R_{last-1}) have already been used to define the residual range in the last detector, they can provide only one unique estimate of the mass. The results of the analysis just described for the event considered in figure III.2 are shown in figure III.2C.

The best estimate of the mass is taken as that corresponding to the maximum range, namely A_3. This is reasonable since, in general, the point (L_i, R_i) contains all the information contained in L_{i-1}, R_{i-1}) plus a contribution from detector i. As one goes to longer and longer ranges, the increase in precision due to additional detectors penetrated decreases. In other words, the most important detectors in determining the mass of a particle are the ones nearest the end of its range. This especially stands out when one chooses to analyze in a multiple $\frac{dL}{dE}$ versus (R or L) mode; where $\frac{dL}{dx}$ must be measured as close as possible to the end of a particle's range. The mass estimates $A_4, \ldots, A_{last-1}$ are used only to test the internal consistency of the event or, in other words, to look for background.

4. <u>Rejection of Background</u>. One would expect the A_i to approach A_3 in the manner of a convergent series as detector number, i, decreases. This follows since, as range is increased, each new detector added contributes a smaller fraction of the total light, L_i. Such a behavior is seen, for example, in figure III.2C. If we suppose that the A_i are distributed about A_3 with a Gaussian distribution, then we can compute the variance of the A_i, $\mathrm{var}(A) = \sigma^2$, where σ is a number characteristic of the width of the distribution. However, for background events, one expects relatively large excursions of the A_i since the particle has changed its mass (and possibly also its charge) at some point in the experiment. These excursions should be reflected in abnormally large values of the var(A) parameter. In figure III.7, a frequency distribution of the var(A) parameter for Be events is shown. From this figure a test given by

$$\mathrm{var}(A) \lesssim 0.10 \left(\frac{A}{8}\right)^2 \qquad \text{(III.22)}$$

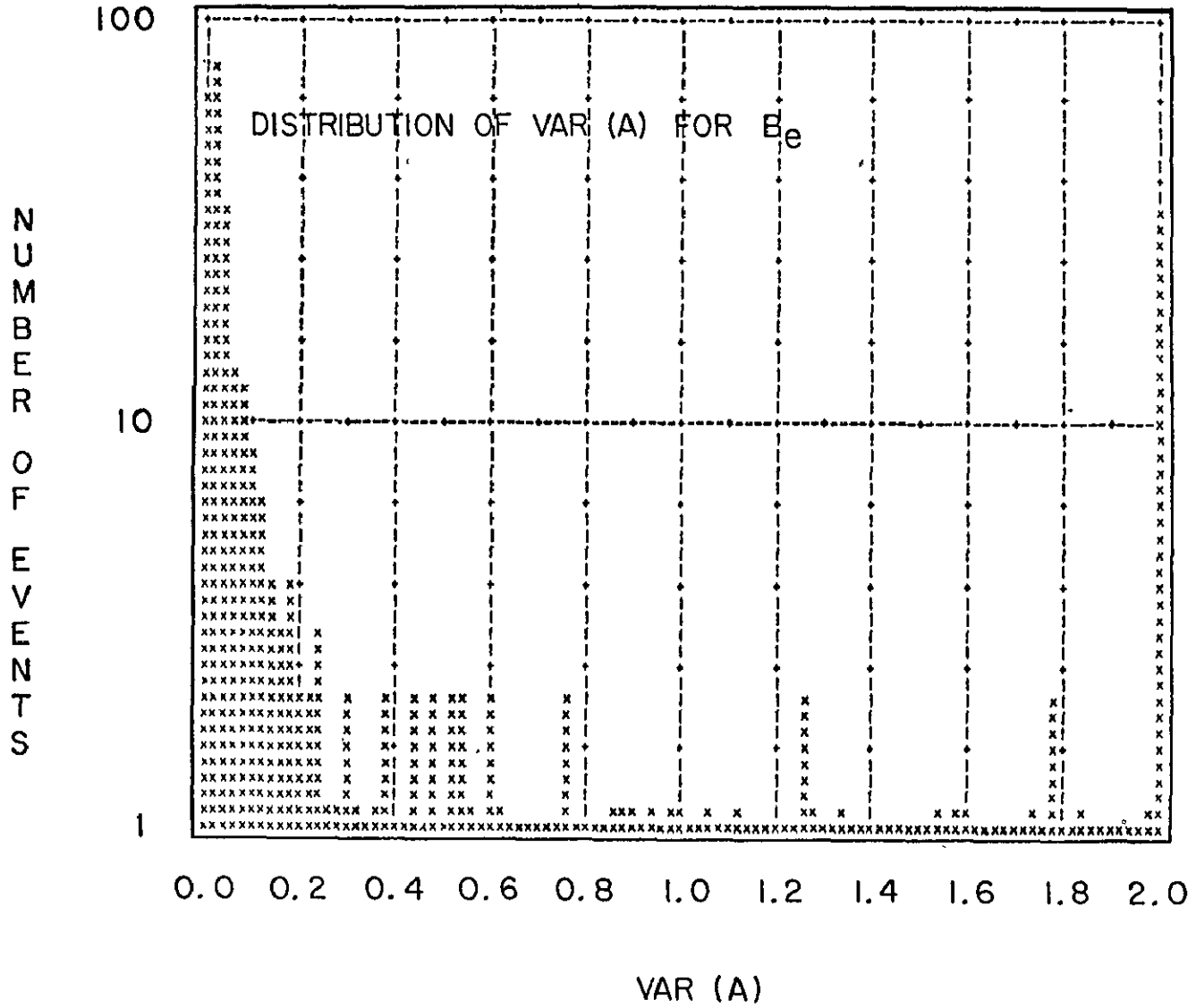

Figure III.7. Distribution of mass variance for Be events.

has been defined in order to select non-interacting events. Events which fail this test are identified as background and discarded. The scaling with mass of the selection threshold given by equation III.22 can be supported on both analytical and observational grounds; this justification will be discussed in detail when the mass resolution is considered in section III.D. The effectiveness of the criterion III.22 in removing background events is readily seen by a comparison of figures III.8 and III.5.

5. Observed Isotopic Composition. The mass histograms resulting from the analysis just described are displayed in figure III.9. Also shown are equivalent histograms for events which were rejected by the var(A) criterion, III.22, as background. It is to be noted that, in most cases, the background level is quite flat; for the one notable exception (C), the background peak is at a distinctly different mass than the non-background peak. As may be seen from the figure, the percentage of events rejected decreases as mass increases. One would expect the opposite behavior, if anything, since the total inelastic cross section increases with A. This observation is taken as an indication of the increased efficiency of the initial selections on the data in removing background. In particular, the requirement that the scintillator pulse heights be (within specified limits and excluding the detector in which a particle stops) a monotonically increasing function of detector number is considered to be responsible for this effect.

The mass distribution for each element has been fitted using the maximum likelihood method. In doing this, the mass distribution corresponding to a single isotope of mass A and charge Z is assumed to be a simple Gaussian:

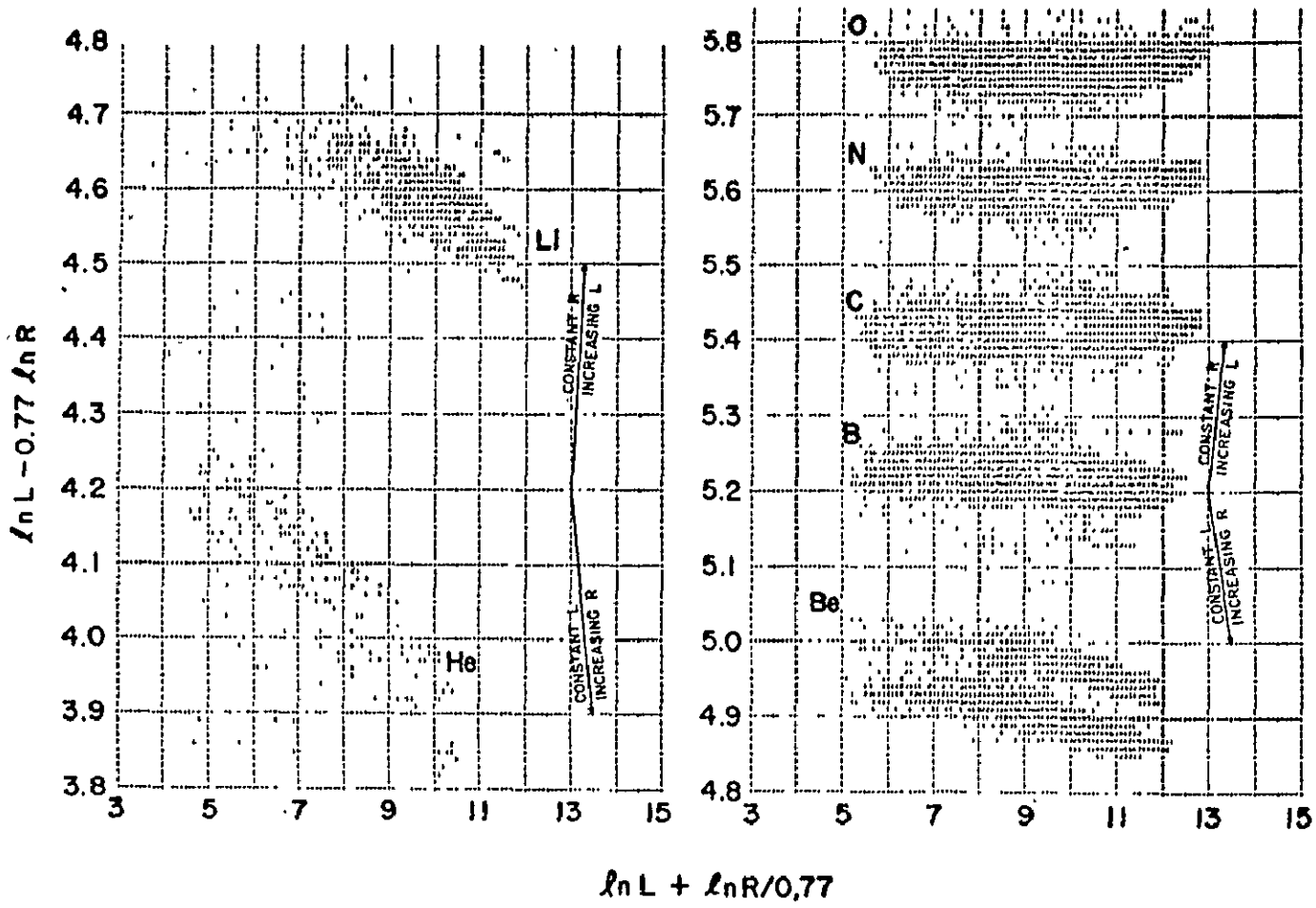

Figure III.8. Rotated light versus range plot for selected data.

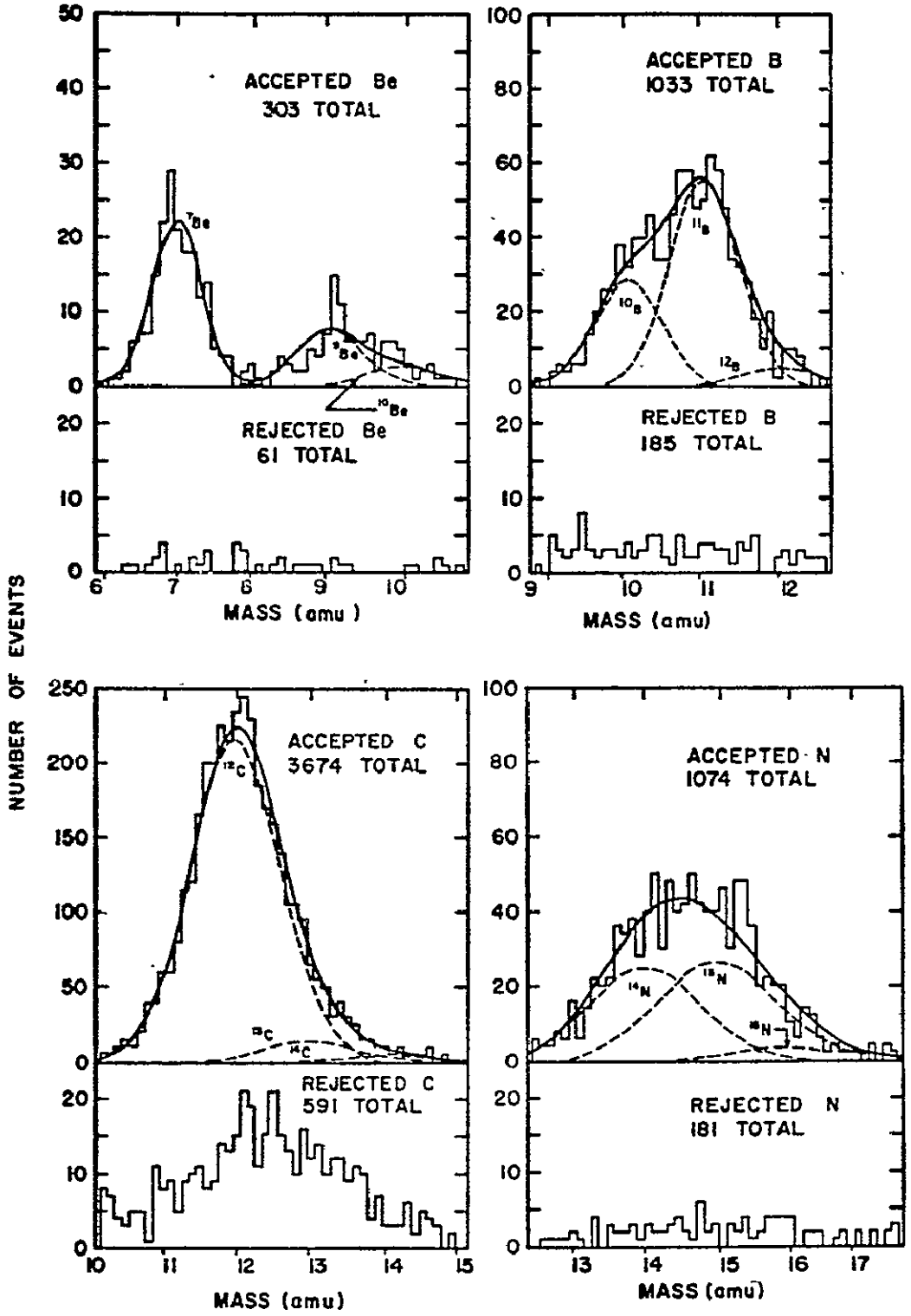

Figure III.9. Mass histograms for data accepted and rejected by mass variance criterion. Maximum likelihood fits to accepted data are also indicated.

$$ {}^{A}_{Z}N(A') = \left[\frac{{}^{A}_{Z}N_{tot}}{\sqrt{2\pi}\,{}^{A}_{Z}\sigma}\right] \exp\left[-\frac{1}{2}\left(\frac{A'-A}{{}^{A}_{Z}\sigma}\right)^{2}\right] \qquad \text{(III.23)} $$

where A is the actual isotopic mass and A' represents the observation. Furthermore, the widths of the mass distributions, ${}^{A}_{Z}\sigma$, for different isotopes of the same element are assumed to scale as the mass:

$$ {}^{A}_{Z}\sigma = \left(\frac{A}{A_s}\right) {}^{A_s}_{Z}\sigma \qquad \text{(III.24)} $$

This is equivalent to the scaling (equation III.22) of the background mass variance threshold with A^2. The justification for both of these assumptions will be discussed later in section III.D. Finally, it will be recalled that the analysis only yields the mass of a particle relative to that corresponding to the standard response line for a given element, A_s. It is therefore convenient to include A_s as a free parameter in the fit, especially for elements where no isotope was clearly separated. The parameters which are varied in the maximum likelihood fit for a given element are, then, the mass corresponding to the standard response curve, A_s, the characteristic resolution, ${}^{A_s}_{Z}\sigma$, and the abundances of the various allowed isotopes, ${}^{A}_{Z}N_{tot}$. The best fits to the various distributions are indicated by smooth curves in figure III.9. The best fit parameters are listed in table III.2, together with the statistical errors (standard deviations) assigned by the maximum likelihood method. These error estimates include the effects of correlations among the various free parameters in the fit.

In order to improve the convergence of the maximum likelihood fit to the mass distribution to nitrogen, a second analysis has been performed in which the value of ${}^{14}_{7}\sigma$ was fixed. The precise value used

TABLE III.2. Maximum Likelihood Best Fit Parameters. Uncertainty estimates are based on the assumption of Gaussian likelihood distributions. The subscript S refers to the standard response curves shown in figures III.4 and III.5.

Beryllium	Boron	Carbon	Nitrogen	Nitrogen*
$A_s = 7.88 \pm 0.04$	$A_s = 9.75 \pm 0.01$	$A_s = 12.12 \pm 0.01$	$A_s = 14.47 \pm 0.61$	$A_s = 14.57 \pm 0.19$
${}^{8}_{4}\sigma = 0.38 \pm 0.13$	${}^{10}_{5}\sigma = 0.42 \pm 0.14$	${}^{12}_{6}\sigma = 0.60 \pm 0.02$	${}^{14}_{7}\sigma = 0.74 \pm 0.08$	${}^{14}_{7}\sigma = 0.658^{*}$
${}^{7}_{4}N_{tot} = 189 \pm 14$	${}^{10}_{5}N_{tot} = 302 \pm 32$	${}^{12}_{6}N_{tot} = 3301 \pm 60$	${}^{14}_{7}N_{tot} = 464 \pm 309$	${}^{14}_{7}N_{tot} = 405 \pm 75$
${}^{9}_{4}N_{tot} = 81 \pm 11$	${}^{11}_{5}N_{tot} = 641 \pm 36$	${}^{13}_{6}N_{tot} = 256 \pm 26^{**}$	${}^{15}_{7}N_{tot} = 523 \pm 244$	${}^{15}_{7}N_{tot} = 525 \pm 56$
${}^{10}_{4}N_{tot} = 34 \pm 8$	${}^{12}_{5}N_{tot} = 69 \pm 18$	${}^{14}_{6}N_{tot} = 93 \pm 15$	${}^{16}_{7}N_{tot} = 69 \pm 72$	${}^{16}_{7}N_{tot} = 123 \pm 35$

*Value of ${}^{14}_{7}\sigma$ fixed using figure III.9 in order to improve resolution.

**Uncertainty has been estimated for ${}^{13}C$ due to difficulties in taking 2nd derivative of likelihood function.

for ${}^{14}_{7}\sigma$ has been obtained essentially by generalizing equation III.24 to relate resolutions for isotopes even of different elements. Equation III.24 then becomes similar to the assumed scaling of the variance selection threshold given by equation III.22. Both analytical and empirical justifications for these assumptions are given in section D, where the mass resolution is considered in detail. In particular, figure III.10 has been used to fix the value of ${}^{14}_{7}\sigma$. The result of this procedure, given in table III.2, is apparently a significant improvement in the resolution with which the remaining free parameters are determined. However, it must be born in mind that uncertainties in the fitted parameters resulting from an uncertainty in ${}^{14}_{7}\sigma$ through correlations will not be included in the uncertainties estimated by this approach. Nevertheless, these results have been adopted for the remainder of this thesis.

In performing the maximum likelihood fits to the mass distributions for the elements B, C and N, it was found that they tended to converge better when allowed to add contributions from unstable nuclei to the mass distributions on the high mass side. The abundances of these isotopes (i.e. ${}^{12}B$, ${}^{16}N$ and ${}^{14}C$) were generally more than could be explained by production in the atmosphere above the experiment. The most likely cause of such an effect appears to be an asymmetry in the mass distributions for these elements. This can very probably be related in part to the fact that the response curves for these elements were not determined from data corresponding to a single isotope. In order to estimate the possible magnitude of this effect for Be, we observe that these spurious isotopes are generally $\sim$ 10% of neighboring abundant isotopes. As applied to ${}^{10}Be$, this would mean a reduction by one standard deviation in the observed abundance. We note that there seems to be no such effect

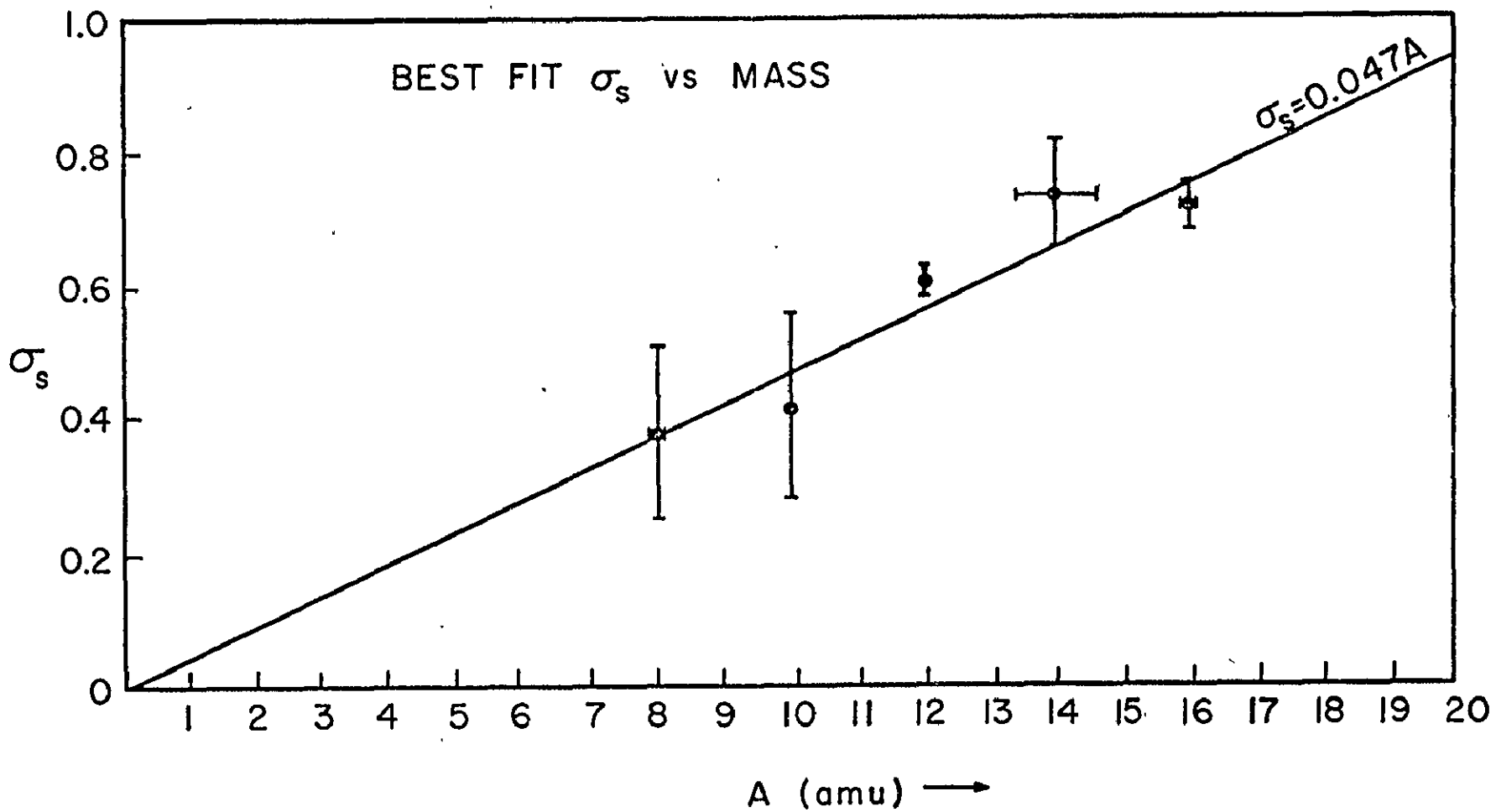

Figure III.10. Mass resolution (as derived from maximum likelihood fits) as a function of mass.

in the case of ^{7}Be--in particular, the ~ 19 ^{8}Be we might expect from the above considerations are not observed. For the purposes of further analysis of the data, the spurious isotopes ^{12}B, ^{14}C and ^{16}N have been obsorbed into the observed abundances of the remaining isotopes of B, C and N, respectively, in such a manner as to preserve the fractional isotopic abundances within each element.

D. Consideration of Mass Resolution

1. Contributing Factors. The mass resolutions achieved in the mass distributions of figure III.7 are estimated in table III.2. It is readily apparent that only the isotope ^{7}Be has been clearly separated, and this only by virtue of the absence of ^{8}Be. In particular, we have not achieved the goal ($\sigma \leqslant 0.35$ for ^{10}Be) which was set in section III.B.7, and consequently do not observe two peaks separated by a valley in the mass distribution representing ^{9}Be and ^{10}Be. As may be seen from table II.2, this may be traced to the uncertainty in our measurement of the total light, which is estimated as ~ 2% (we require ~ 1%). This is limited by the internormalization of the responses of the various detectors, which in turn was limited primarily by the necessity of using semi-relativistic particles and also by response functions which varied from detector to detector. Thus, the primary goal in improving the resolution would be to improve the precision of the total light measurement through a detailed calibration of the response of each detector. Nevertheless, the resolution which has been obtained is comparable to those of other experiments which have been reported (Webber et al. 1973, Preszler et al. 1975, Garcia-Munoz et al. 1975, 1975a).

As a step towards understanding the mass resolution realized in the experiment (e.g. see figure III.9), various contributions are illustrated in figure III.11. The dominant contribution is from Landau

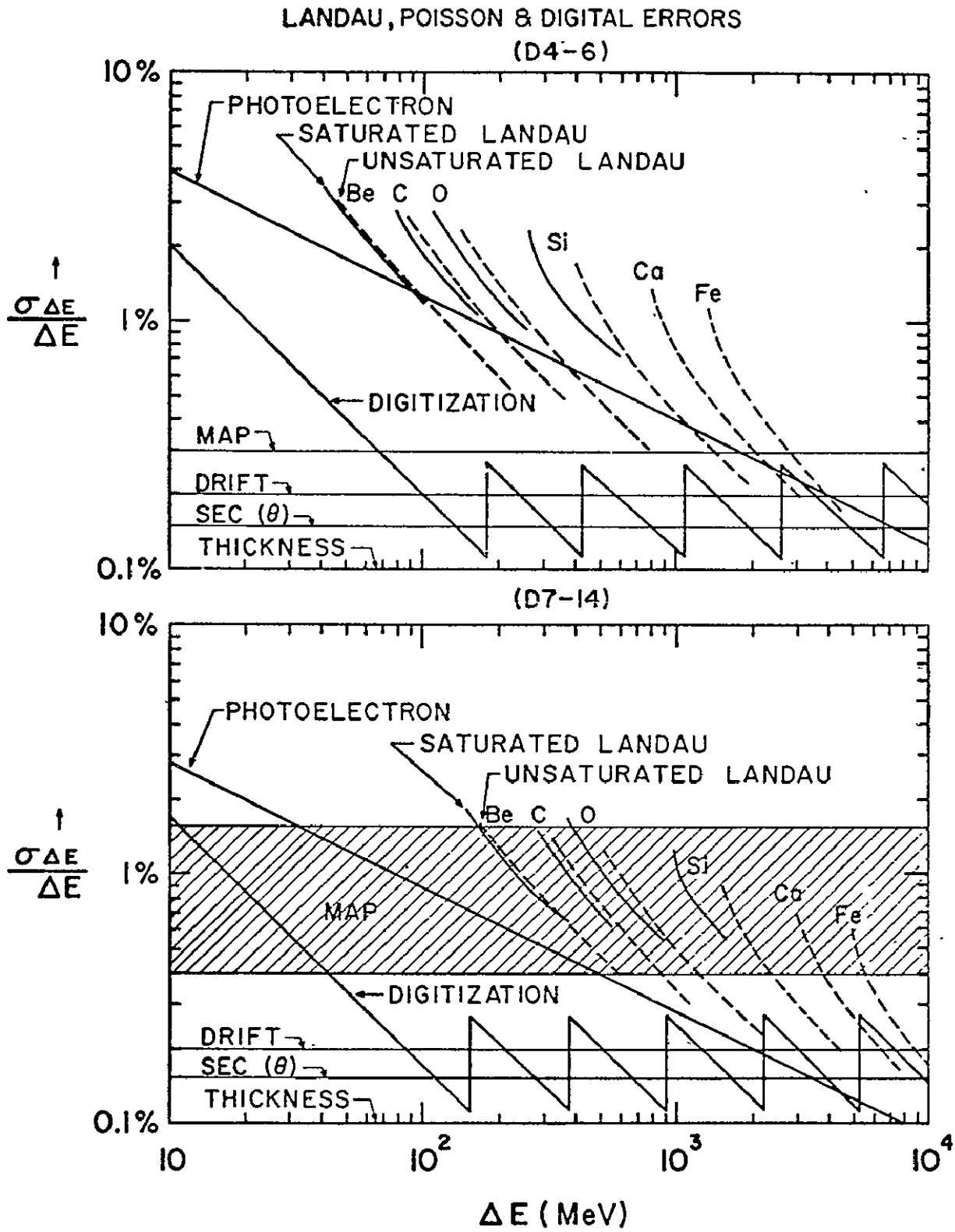

Figure III.11. Contributions to the experimental uncertainties.

fluctuations, which result from the statistics of producing very high energy knock-on electrons and thereby depositing an abnormally large amount of energy in a given detector (e.g. see Rossi 1952). For thin detectors, this effect can cause a distribution of pulse heights in response to a uniform beam of incident particles which is skewed towards high pulse heights. However, for the present considerations, a Gaussian approximation to the Landau distribution is adequate. This is given for scintillation detectors by

$$\sigma_{Landau} = \left(\frac{T}{12.3\ g\,cm^{-2}}\right)^{\frac{1}{2}} \gamma \left(1 - \frac{1}{2}\beta^2\right)^{\frac{1}{2}} \left(2 m_e c^2\right) \qquad \text{(III.25)}$$

where T denotes the detector thickness. Equation III.25 is valid only in the limit where the energy given a single knock-on electron is small in comparison to the total energy lost in a detector, which holds for all cases of interest here. The magnitude of the Landau fluctuations is probably not significantly affected by saturation of the scintillator response, since the fluctuations are attributed to long range delta rays which deposit most of their energy far from the core of intense ionization immediately surrounding the trajectory of the primary particle. However, the magnitude of the effect relative to the observed pulse height will, in general, increase as scintillator saturation is introduced since the pulse height itself is reduced by saturation effects while Landau fluctuations probably are not. The correction to the Landau fluctuations for scintillator saturation effects, derived from figure III.6, is also indicated in figure III.11.

A second contribution to the broadening of the mass resolution comes from the Poissonian statistics associated with the fact that only a statistical fraction of the photons produced by the scintillators is

actually observed by the photomultiplier tubes. This is formulated in equation II.2. The photoelectron conversion efficiency shown in figure III.11 has been taken from the preflight calibration of the various detectors (see table II.3).

Of the remaining contributions to the broadening of the mass resolution shown in figure III.11, digitization refers to the round off error due to the digitization of the signal by the pulse height analyzers. For the 256 channel analyzers (with synchronous clocks), this has been approximated by a Gaussian distribution characterized by a standard deviation

$$\sigma_{Dig} \sim \frac{1}{2\sqrt{3}} \text{ channels} \tag{III.26}$$

Estimates of the statistical resolution of the temporal and positional mapping of response variations, our knowledge of detector thicknesses and the resolution of the spark chamber in defining particle trajectories are also indicated in the figure. Not included in the figure is the contribution of detector normalization uncertainties, which are thought to enter at about the 2% level.

2. <u>Analytical Analysis of Resolution</u>. After incorporating the scaling laws III.15 and III.16 into the power law approximation to the standard response curves (given by equation III.10) one obtains a general formulation of the detector response, which may then be solved for the mass:

$$A = \alpha^{\frac{1}{\delta-1}} A_S \, L^{\frac{\delta}{\delta-1}} \, R^{-\frac{1}{\delta-1}} \tag{III.27}$$

Assuming the independence of the parameters L and R, the mass resolution, σ_A, may be estimated in terms of the range resolution, σ_R, and light

resolution, σ_L:

$$\left(\frac{\sigma_A}{A}\right)^2 = \left(\frac{\delta}{\delta-1}\right)^2 \left(\frac{\sigma_L}{L}\right)^2 + \left(\frac{1}{\delta-1}\right)^2 \left(\frac{\sigma_R}{R}\right)^2 \qquad \text{(III.28)}$$

The assumption that R and L are independent is technically valid only in the limit of long range, where the information used to determine R becomes an insignificant contribution to L. However, the contribution of range to the total uncertainty is normally quite small, as will be seen below. It is then reasonable to use equation III.28 to estimate the resolution of the mass measurement even for particles of short range.

In order to estimate the uncertainty of the range measurement, we rewrite equation III.12 for the range in the last detector in the form

$$R_{last} = T_{last-1} \sec\theta \left[H_R^{\delta} - 1\right]^{-1} \qquad \text{(III.29)}$$

where

$$H_R = \frac{H_{last-1}}{H_{last}} + 1 = \frac{L_{last-1}}{L_{last}} \qquad \text{(III.30)}$$

gives the ratio of light observed in the last two detectors penetrated to that observed in the last detector penetrated. Generally, we have $H_R \geqslant 2$; however when the particle stops in the first thick detector, D7, this becomes $H_R \geqslant 1.25$. If the pulse heights are known to a resolution given by $\frac{\sigma_H}{H}$, then the uncertainty in the range measurement is

$$\frac{\sigma_R}{R_{last}} = \sqrt{2}\left(\frac{\sigma_H}{H}\right)\left[\frac{\delta H_R^{\delta-1}(H_R - 1)}{H_R^{\delta} - 1}\right] \qquad \text{(III.31)}$$

For $H_R \geqslant 1.25$, the term in brackets is bounded by 1 and δ and equation III.31 becomes

$$\sqrt{2}\left(\frac{R_{last}}{R}\right)\left(\frac{\sigma_H}{H}\right) \leq \frac{\sigma_R}{R} \leq \delta\sqrt{2}\left(\frac{R_{last}}{R}\right)\left(\frac{\sigma_H}{H}\right) \qquad \text{(III.32)}$$

Finally, by putting

$$R \simeq (2\,last - 5)\, R_{last} \tag{III.33}$$

we obtain

$$\frac{\sigma_R}{R} \simeq \frac{\delta+1}{\sqrt{2}\,(2\,last-5)} \frac{\sigma_H}{H} \tag{III.34}$$

The uncertainty in the determination of the total light, L, is given by

$$\frac{\sigma_L}{L} \simeq \left(\frac{1}{last-2}\right)^{\frac{1}{2}} \frac{\sigma_H}{H} \tag{III.35}$$

Substituting the results given by equations III.34 and III.35 into equation III.28 and factoring out the contribution from the total light, we obtain

$$\begin{aligned} \frac{\sigma_A}{A} &\simeq \left(\frac{\delta}{\delta-1}\right)\left(\frac{1}{last-2}\right)^{\frac{1}{2}}\left(\frac{\sigma_H}{H}\right)\left[1+\left(\frac{1+\delta}{\delta}\right)^2 \frac{(last-2)}{2(2\,last-5)^2}\right]^{\frac{1}{2}} \\ &\simeq \left(\frac{\delta}{\delta-1}\right)\left(\frac{1}{last-2}\right)^{\frac{1}{2}}\left(\frac{\sigma_H}{H}\right)\left[1+\frac{1}{2}\left(\frac{1+\delta}{2\delta}\right)^2\left(\frac{1}{last-2}\right)\right]^{\frac{1}{2}} \end{aligned} \tag{III.36}$$

The second term in brackets is negligible for $\delta \gg 1$, which is easily satisfied for all cases of interest. In particular, $\delta = 1.3$ for the Pilot Y scintillators used in the present experiment, and $\delta \simeq 1.8$ for a completely non-saturating scintillator (see equation II.22). Thus the contribution of range to the total uncertainty in the mass measurement is in fact negligible, as has already been pointed out. We then have

$$\frac{\sigma_A}{A} \simeq \left(\frac{\delta}{\delta-1}\right)\left(\frac{1}{last-2}\right)^{\frac{1}{2}}\left(\frac{\sigma_H}{H}\right) \tag{III.37}$$

For the present case, the scintillators have been estimated to be normalized to within $\frac{\sigma_H}{H} \simeq 0.02$. Putting $\delta = 1.3$ and assuming the particle to

stop in D7, we then have the result

$$\sigma_A \cong 0.039\ A \tag{III.38}$$

The result given by equation III.37 supports the assumption that the mass resolution scales as the mass (equation III.24). It also supports the related assumption that the mass variance selection threshold used to reject background should scale as mass squared. Essentially, the scaling with mass depends only on the assumption of power law response functions (equation III.27), and thus is quite generally applicable.

The result given by equation III.37 also gives some idea of the parameters one might try to optimize in attempting to design a similar experiment with improved mass resolution. For example, the biggest improvement (potentially at least a factor of two) would result from an improved calibration of the detectors. This is readily seen from figure III.11. Such improvements might be accomplished through extensive accelerator calibrations of the various detectors and/or by the construction of detectors with more uniform response. Alternatively, one could expect as much as a factor of two improvement in mass resolution by going to completely nonsaturating (i.e. $\delta = 1.8$) scintillators. To put the potential for improvement as just discussed into perspective, we note that the mass resolution of the experiment for ^{10}Be is given by equation III.38 as $\sigma_A \cong 0.4$ amu. This should be compared with the critical resolution at which a valley begins to appear between ^{9}Be and ^{10}Be. Taking $k = 2.5$ in equation II.12, this is $\sigma_{crit} = 0.35$ amu. Thus we need achieve only a small part of the potential improvement of the mass resolution before the results become markedly more convincing.

Finally, equation III.36 may be rewritten to give some insight

into the problem of deciding the optimal detector thicknesses for this type of experiment, namely those such that the errors in the range measurement actually are negligible. In particular, the second term in brackets in equation III.36 represents the ratio of the contributions of range and the total light to the total uncertainty. This term may be written

$$1 \gg \left(\frac{1+\delta}{\delta}\right)^2 \frac{1}{2}\left(\frac{R_{last}}{R}\right)^2 \cong \left(\frac{1+\delta}{\delta}\right)^2 \frac{last - 2}{2(2\,last - 5)^2} \qquad \text{(III.39)}$$

where the inequality expresses the condition for the uncertainty in the range measurement to be negligible. Putting $\delta = 1.3$, we then require the range in the last detector to satisfy

$$R_{last} \ll 0.64\,R \qquad \text{(III.40)}$$

Thus, each detector should be much less than half the thickness of the material above it in the totally active stack (i.e. D3-14 in the present case). This condition is easily satisfied by the present experiment, since no particles have been accepted which stop before detector D5.

3. <u>Empirical Consideration of Resolution</u>. Since the assumption of a mass resolution which scales as the mass is quite important in the analysis, it is desirable to obtain empirical evidence of its validity if possible. This has been attempted in two ways. The first (see figure III.10) is to plot the $\frac{A_s}{Z}\sigma$ derived from fitting the mass distributions against A_s. Since the fit for each element was done independently of the others, this gives one point for each element considered. Although the resolution appears to scale as predicted, this is not a completely definitive check since a scaling of the resolution with charge (rather than mass) would satisfy the data equally well. However, there is no a

priori reason to believe this is so. A second check was attempted in order to test the scaling among different isotopes of a single element. Figure III.12A gives the distribution of var(A) for Be with $A > 8$ as compared that for $A < 8$. If a mass independent threshold on var(A) is correct, then the distribution of var(A) should be identical for all A. Figure III.12A suggests that this is not the case. Figure III.12B shows the same comparison after correcting the variance for the assumed A^2 scaling. The situation is definitely improved over the uncorrected case, and the mass scaling of the resolution is supported.

E. Corrections to the Data

In order to determine the cosmic ray composition at the top of the atmosphere, various corrections have been applied. These factors are listed in table III.3, together with the observed and various corrected abundances. The corrections treat losses due to interactions in the experiment itself (including the gondola), the production and loss of the various species in the atmosphere, and energy normalization factors to account for the fact that different isotopes are observed over different energy windows and modulated differently in penetrating the solar cavity.

1. Interactions. The correction factors for interactions in the detector itself (column C of table III.3) are given by

$$ {}^{A}_{Z}C^{Inter} = {}^{A}_{Z}N_{tot}^{-1} \int_0^R dR' \frac{d}{dR'}\left({}^{A}_{Z}N_{td}\right) \exp\left[\sum_{A_{tar}} \sigma(A, A_{tar}) \int_0^{R'} dR'' \, n(A_{tar})\right] \qquad \text{(III.41)} $$

Here $n(A_{tar})$ is the density of target atoms of mass A_{tar} along the trajectory of a particle, and the total inelastic (reaction) cross section, $\sigma_{tot}(A,A_{tar})$, is given by the empirical relation

$$ \sigma_{tot}(A, A_{tar}) = 10\,\pi\,(1.29)^2\left(A^{\frac{1}{3}} + A_{tar}^{\frac{1}{3}} - b\right)^2 \qquad \text{(III.42)} $$

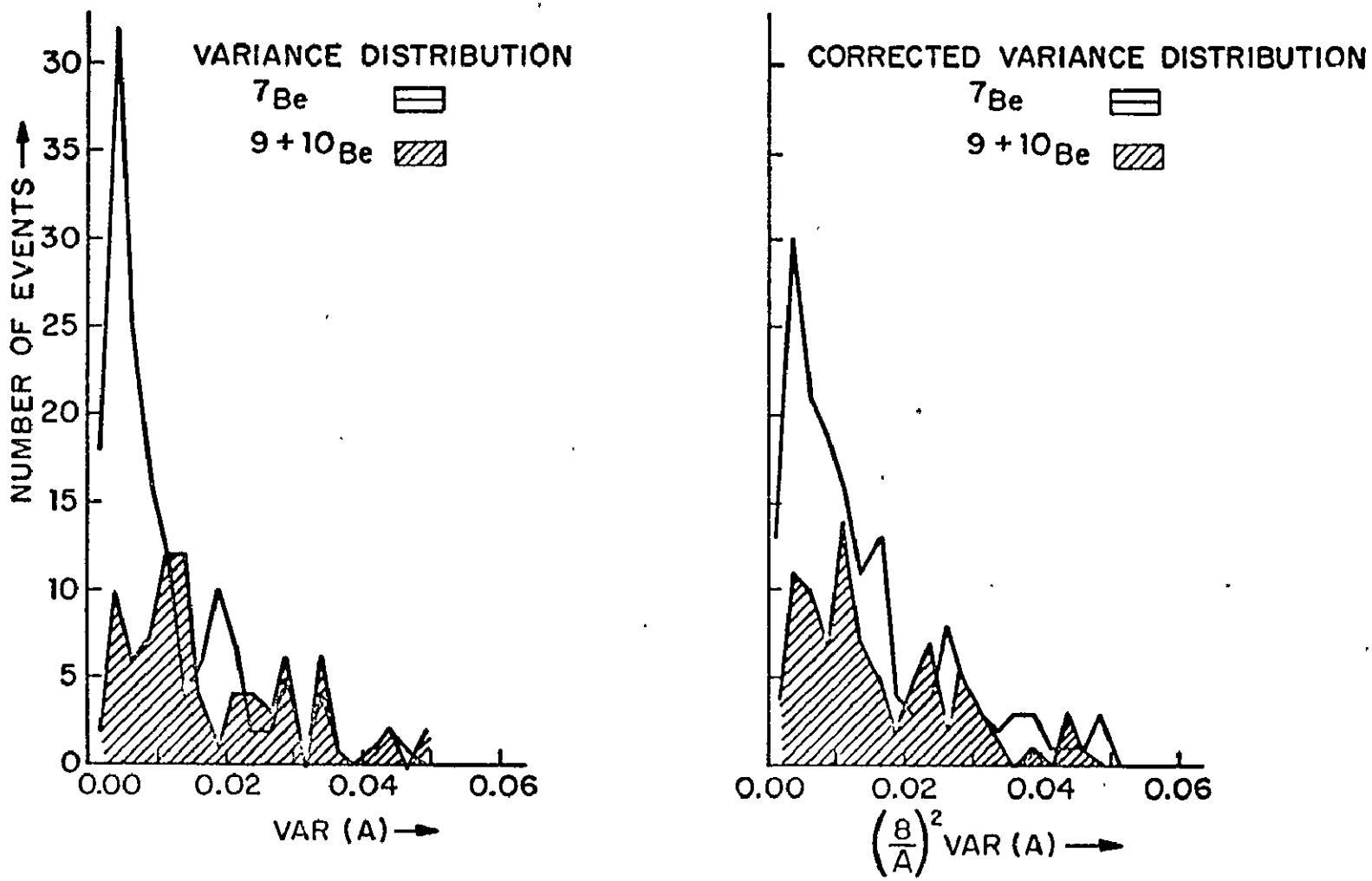

Figure III.12. Mass variance distributions (both uncorrected and corrected for assumed A^2 scaling) for Be events with $A > 8$ as compared to Be events with $A < 8$.

TABLE III.3: CORRECTION FACTORS APPLIED TO THE DATA

Isotope	Energy Windows: At Detector	Energy Windows: Interplanetary	Energy Windows: Interstellar	Energy Window Correction: A	Energy Window Correction: B	Detector Interaction Correction: C	Atmospheric Correction: To $0 gcm^{-2}$: D	Atmospheric Correction: To $3 gcm^{-2}$: E	Demodulation Correction: F	G	H	I	J	Observed and Corrected Abundances**: Observed	Atmospheric Correction: BCR	BCD	ACD	Interstellar: ACDF
^{7}Be	93-358	199-416	489-707	1.00*	1.00*	1.39	0.86	0.95	1.00*	1.00*	1.00*	1.00*	1.00*	52±4	50±4	50±5	43±5	42±4
^{9}Be	81-307	172-356	398-582	1.17	1.15	1.44	0.90	0.97	0.83	0.83	0.83	0.85	0.85	22±3	26±4	21±4	23±4	19±3
^{10}Be	76-288	161-334	363-537	1.40	1.23	1.47	0.75	0.91	0.81	0.70	0.69	0.71	0.71	9±2	11±4	8±3	10±4	8±3
^{10}B	98-378	209-440	464-695	0.93	0.95	1.42	0.99	1.00	0.97	0.98	0.98	1.06	1.07	89±9	88±10	89±12	80±10	76±10
^{11}B	93-356	198-415	429-646	0.99	1.00	1.45	1.07	1.03	0.90	0.92	0.91	1.00	1.00	188±10	205±13	184±13	197±14	175±12
^{12}C	109-424	233-494	488-749	0.85	0.87	1.48	1.17	1.06	1.02	1.01	1.02	1.15	1.16	928±17	927±25	928±33	932±33	936±33
^{13}C	104-403	222-470	457-705	0.88	0.91	1.50	1.04	1.02	0.95	0.97	0.97	1.11	1.12	72±10	73±8	72±9	68±8	64±8
^{14}N	118-467	256-546	510-800	0.79	0.82	1.50	1.08	1.03	1.06	1.04	1.04	1.23	1.25	126±23	116±23	126±27	111±23	117±25
^{15}N	114-447	245-522	483-760	0.81	0.84	1.52	1.12	1.04	1.01	1.01	1.01	1.21	1.23	163±17	159±18	164±20	155±19	154±19

* Normalization
** Normalized to C = 1000
A Based on local interplanetary spectra predicted by Garcia-Munoz et al. (1973)
B Based on local interplanetary ^{12}C spectrum according to Garcia-Munoz et al. (1973)
F Based on interstellar spectra as predicted by Garcia-Munoz et al. (1973)
G Based on interstellar spectra of the form $J = \alpha\gamma^{-2.60}$
H Based on interstellar spectra of the form $J = \alpha\gamma^{-2.75}$
I Based on interstellar spectra of the form $J = \alpha\rho^{-2.60}$
J Based on interstellar spectra of the form $J = \alpha\rho^{-2.75}$

ORIGINAL PAGE IS OF POOR QUALITY

where

$$b = 1 - 1.189 \exp\left[-0.05446 \, \mathrm{Min}(A, A_{tar})\right] \tag{III.43}$$

This relation has been fitted to the data of Lindstrom et al. (1975) for ^{12}C, ^{16}O and ^{40}A beams incident on various targets at the Bevatron, together with the data of Renburg et al. (1972) for proton beams. Finally, the number of particles stopping between R and R +dR, $\frac{d}{dR} {}^{A}_{Z}N_{tot}$, is computed as a function of charge from the data, with mass dependent effects (if any) being averaged out. This is required both by the problem of statistics, and the fact that most isotopes are not resolved on an event by event basis.

2. Energy Corrections. Since the experiment is sensitive to the various isotopes observed in energy windows of differing width and location, the results must be accordingly corrected before meaningful comparisons can be made with either theory or other experiments. The ideal way of presenting the data would be in the form of differential energy spectra, in which case the corrections would be minimized. However, this approach is of little advantage for isotopes of very low abundance, in which case the statistical errors severly limit the resolution obtainable. The alternative is to assume the shape of the spectra, which may then be used to normalize the results to some fixed energy. Ideally, the spectra used should be experimental, but a complete set does not exist which covers all isotopes of interest at the right time (i.e. in August 1973). We have therefore adopted the local interplanetary spectra for 1973 which have been calculated by Garcia Munoz et al. (1975b). They have assumed primary source spectra of the form $(E + 400)^{-2.6}$ which are then propagated to the vicinity of the sun using a leaky box model for the interstellar

propagation (to be discussed later in Chapter IV) with a mean pathlength of $\lambda_e \simeq 5$ g cm^{-2} and a density of interstellar matter given by $n \simeq 1$ atom cm^{-3}. They have then used the numerical technique of Fisk (1971) to modulate the spectra, and thus are able to predict the spectra observed near the earth. Wherever possible, the calculated spectra have been matched to observations by adjusting the available free parameters (mainly in the diffusion coefficient used for modulation). The resulting spectra may thus be regarded as extrapolations of the available experimental data to cover all isotopic species. The correction factors for the various energy windows in which the experiment is sensitive have been computed mapping the energy windows to the top of the atmosphere, then integrating the (predicted) spectra over both the extrapolated energy window and a standard energy window (233-494 MeV/nuc) corresponding to that in which the experiment was sensitive to ^{12}C. This is formulated mathematically by

$$ {}^{A}_{Z}C^{E} = \left[\int_{233\,\mathrm{MeV/nuc}}^{494\,\mathrm{MeV/nuc}} dE \; {}^{A}_{Z}J(E) \right] \left[\int_{E_1}^{E_2} dE \; {}^{A}_{Z}J(E) \right]^{-1} \qquad \text{(III.44)} $$

where $E_1 < E_2$ defines the extrapolated energy window, and ${}^{A}_{Z}J(E)$ represents the differential energy spectrum for particles of mass A and charge Z. The correction factors computed as just described are listed in column A of table III.3 together with the relevant energy windows at the detector and the top of the atmosphere. The energy window correction factors have also been computed on the basis of the assumption that all isotopes have the same spectral shape as ^{12}C. These are listed in column B of table III.3. This has been done in order to facilitate comparisons with the data of other experimenters, who have generally made this assumption in

correcting their data (Webber et al. 1973, Preszler et al. 1975, Garcia-Munoz 1975a). However, we feel that the former approach is superior, and have used it exclusively in the interpretation of our data. We expect that the difference between the two approaches will be most apparent when considering: 1) secondary components of the cosmic rays, whose spectra in interstellar space are expected to diverge from those of the primary species (e.g. ^{12}C) from which they are produced, and 2) isotopes which do not have $A \sim 2Z$ and are therefore affected differently by the solar modulation process than is ^{12}C. These observations are borne out by comparing the corrections computed for ^{10}Be (a very important isotope which satisfies both conditions above) under the two sets of assumptions. The correction we have adopted has the effect of giving more ^{10}Be in interstellar space.

3. Atmospheric Corrections. The production and destruction of the various isotopic species in the atmosphere above the detector has been corrected for using a model based on the semi-empirical formula of Silberberg et al. (1973) for the partial cross sections σ_{ij}^{k} (to produce species j from an interaction where species i is incident on species k). Equation III.42 has been assumed for the total cross sections. The semi-empirical formula has been normalized to the results of Lindstrom et al. (1975a) for the particular cases of ^{12}C and ^{16}O primaries. The normalization factors adopted are listed in table III.4.

We begin by temporarily treating the atmosphere as a slab of uniform thickness and known composition, the flux of species i surviving at depth X without undergoing any interaction is

$$J_{io}(X) = J_i(0)\, e^{-\lambda_i X} \qquad \text{(III.45)}$$

TABLE III.4

Correction Factors Applied to Semiempirical Formula for Partial Cross Sections (Silberberg et al. 1973), as Derived From Data of Lindstrom et al. 1975a

	Primary	
Secondary	^{12}C	^{16}O
^{7}Be	0.91	
^{9}Be	1.69	1.28
^{10}Be	1.56	
^{11}Be		0.57
^{12}Be		5.00
^{8}B	0.25	0.26
^{10}B	1.45	0.93
^{11}B		1.18
^{12}B		0.54
^{9}C	0.61	0.57
^{10}C	0.57	0.53
^{11}C	0.88	0.91
^{12}C		1.72
^{13}C		1.05
^{14}C		0.50
^{12}N		0.17
^{13}N		1.11
^{14}N		1.67
^{15}N		1.43
^{13}O		0.53
^{14}O		0.23
^{15}O		0.71

where

$$h_i = \sum_{tar} n(A_{tar})\, \sigma_{tot}(A_i, A_{tar}) \tag{III.46}$$

We can also write down a general formula for the flux of particles of species i at depth X which have undergone precisely k interactions:

$$J_{ik}(X) = \int_0^X dX'\, e^{-h_i(X-X')} \sum_{\substack{j \\ A_j > A_i}} g_{ij}\, J_{j(k-1)}(X') \tag{III.47}$$

where

$$g_{ij} = \sum_{tar} n(A_{tar})\, \sigma_{ij}^{tar} \tag{III.48}$$

Equations III.45-48 may be integrated in an iterative fashion, beginning with k = 1. The results, up to k = 3, are

$$J_{i0}(X) = J_i(0)\, e^{-h_i X}$$

$$J_{i1}(X) = \sum_j J_j(0)\, g_{ij} \left(\frac{e^{-h_i X}}{h_j - h_i} + \frac{e^{-h_j X}}{h_i - h_j} \right)$$

$$J_{i2}(X) = \sum_j J_j(0) \sum_k g_{ik}\, g_{kj} \times \left[\frac{e^{-h_i X}}{(h_j - h_i)(h_k - h_i)} + \frac{e^{-h_j X}}{(h_i - h_j)(h_k - h_j)} + \frac{e^{-h_k X}}{(h_i - h_k)(h_j - h_k)} \right] \tag{III.49}$$

$$J_{i3}(X) = \sum_j J_j(0) \sum_{k,l} g_{il}\, g_{lk}\, g_{kj} \times \left[\frac{e^{-h_i X}}{(h_j - h_i)(h_k - h_i)(h_l - h_i)} + \frac{e^{-h_j X}}{(h_i - h_j)(h_k - h_j)(h_l - h_j)} + \frac{e^{-h_k X}}{(h_i - h_k)(h_j - h_k)(h_l - h_k)} + \frac{e^{-h_l X}}{(h_i - h_l)(h_j - h_l)(h_k - h_l)} \right]$$

We thus have, for the total flux of species i arriving at depth X after an arbitrary number of interactions

$$J_i(X) = \sum_{k=0}^{\infty} J_{ik}(X) \tag{III.50}$$

In practice, the $J_{ik}(X)$ decrease monotonically with increasing k above some k'. For the present case ($X \cong 5$ g cm^{-2}), $k' \leqslant 1$, and terms beyond k = 3 are neglected. This is reasonable, since it is observed the $J_{i2} \leqslant 0.02\ J_i$ and $J_{i3} \leqslant 0.0005\ J_i$. It should be noted that the $J_{ik}(X)$ are all linear in the source abundances, $J_i(0)$, so that one may write the result III.50 in the form

$$J_i(X) = \sum_k {}^S D_{ik}(X)\, J_k(0) \tag{III.51}$$

Here the ${}^S D_{ik}(X)$ are determined directly from equations III.49,50. The matrix ${}^S D(X)$ may be regarded as the "propagator" matrix which propogates the cosmic-ray abundance vector $J_k(0)$ through a slab of thickness X. Now, in reality the atmosphere is not a slab for our case. The experiment does not remain at a constant altitude, and particles are incident at various zenith angles. The actual distribution of atmospheric depths (effective slab thicknesses), f(X), is easily determined from the spark chamber data, and is shown in figure III.13. This is readily incorporated into the analysis by merely replacing ${}^S D(X)$ by the atmospheric propagator matrix, ${}^A D$, defined by

$${}^A D = \int dX\, f(X)\, {}^S D(X) \tag{III.52}$$

where f(X) has been assumed to be normalized to unity. Then

$$J_i(X) = \sum_k {}^A D_{ik}\, J_k(0) \tag{III.53}$$

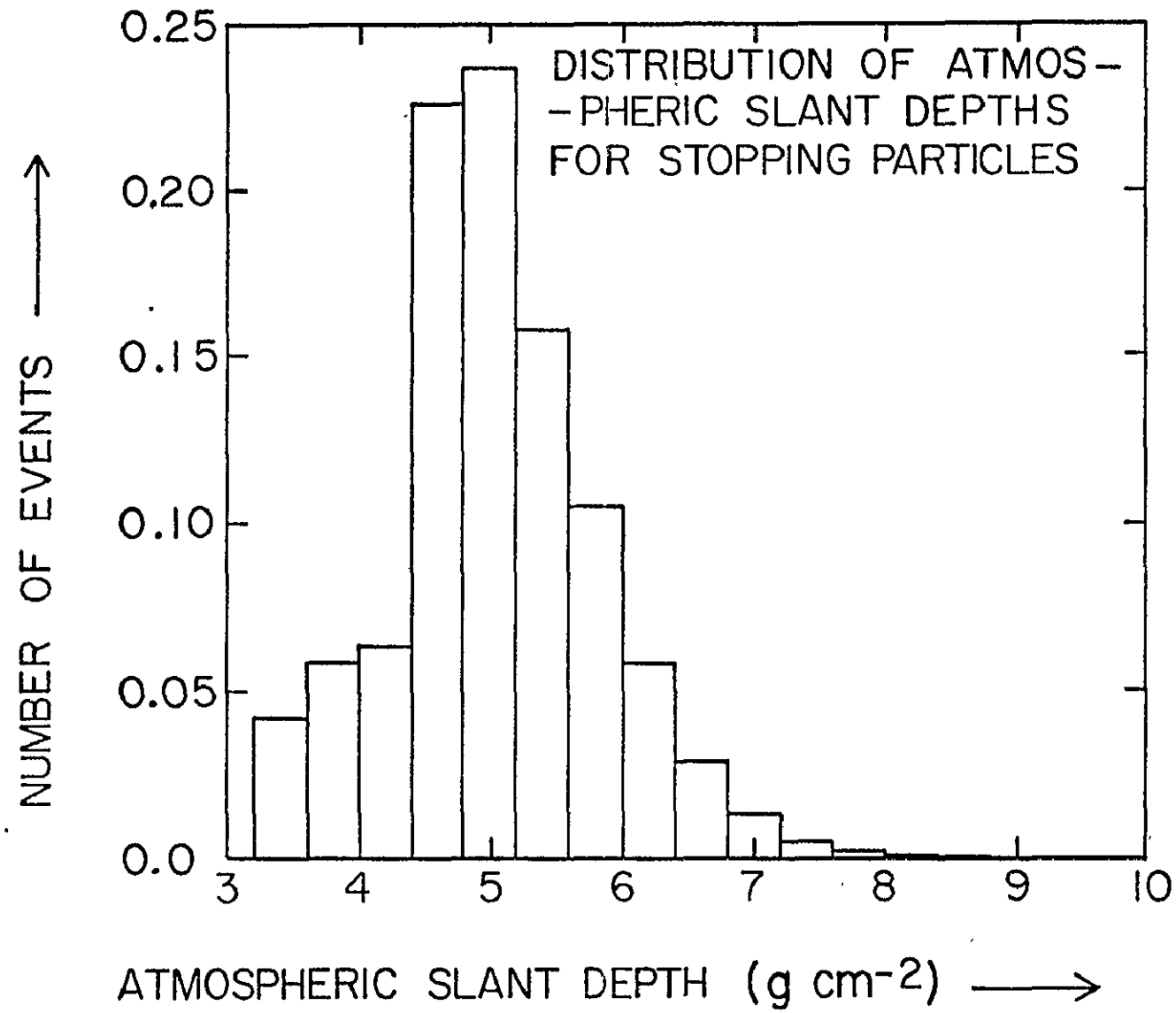

Figure III.13. Distribution of atmospheric slant depths.

The problem is now easily inverted to obtain the abundances at the top of the atmosphere in terms of those observed at the detector:

$$J_i(0) = \sum_k \left({}^{A}D^{-1}\right)_{ik} J_k(X) \qquad \text{(III.54)}$$

This is obviously the formulation of interest here.

The general form of the matrix ${}^{A}D^{-1}$ is triangular. The diagonal elements are positive and greater than one to correct for attenuation in the atmosphere, while the off-diagonal elements are negative to correct for contributions to the observed flux from spallation of heavier species. In order to compute the flux of species i at the top of the atmosphere, $J_i(0)$, it is thus necessary to know the $J_k(X)$ for all species as heavy or heavier (i.e. for $A_k \geq A_i$). Since we have only measured the isotopic abundances of the elements Be, B, C and N, it is therefore required to assume abundances for other species which might contribute. For this purpose, we have adopted the charge abundances measured by Ormes et al. (1975) using the same instrument in the CxS mode of analysis (i.e. D1-3 only) for $E \geq 570$ MeV/nuc. The relative abundances of the isotopes of each element were then taken from the predictions of Tsao et al. (1973) for the arriving cosmic rays. The various isotopes included in the calculation are indicated in table III.5.

In table III.6, the isotopic abundances both at the detector and as extrapolated to the top of the atmosphere are given. The present data have been corrected for interactions in the detector (column A of table III.3) and energy windows (column B of table III.3) before performing this calculation. The atmospheric correction factors listed in column D of table III.3 are computed by merely taking ratios of the abundances listed in table III.6. Once the $J_i(0)$ have been obtained,

TABLE III.5: Stability Selections in the Atmosphere

Z: \ N:	3	4	5	6	7	8	9	10	11	12	13	14	15	16	17	18	19	20	21	22	23	24	25	26	27	28	29	30	31	32	33	34
4	2		2	2																												
5			2	2																												
6				2	2																											
7					2	2																										
8						2	2	2																								
9					1			2																								
10								2	2	2																						
11										2																						
12										2	2	2																				
13												2																				
14												2	2	2																		
15														2																		
16														2	2	2		2														
17																2		2														
18																2	2	2		2												
19																		2	2	2												
20																		2	2	2	2	2		2								
21																						2										
22																						2	2	2	2	2						
23																								2	2	2						
24																								2	2	2	2	2				
25																										2	2	2				
26																										2	2	2	2	2		
27																														2		
28																												2		2		2

Decay Codes

1. e^+ Emission
2. Stable
3. e^- Emission
4. n Emission
5. p Emission
6. α Emission

All Decays Presumed Instantaneous

ORIGINAL PAGE IS
OF POOR QUALITY

TABLE III.6

Isotopic Abundances at Detector and Top of Atmosphere

	Detector ($\sim 4.5 gcm^{-2}$)	Top of Atmosphere
^{7}Be	57±4	43±4
^{9}Be	30±4	23±4
^{10}Be	15±4	10±4
^{10}B	93±10	80±10
^{11}B	214±12	197±12
^{12}C	924±17	932±17
^{13}C	76±8	68±8
^{14}N	119±22	111±23
^{15}N	160±17	155±18
^{16}O	879±18	924±19
^{17}O	23±3	21±3
^{18}O	18±3	17±3
^{19}F	28±3	26±3
^{20}Ne	114±6	119±7
^{21}Ne	15±2	13±2
^{22}Ne	26±3	26±3
^{23}Na	42±4	42±4
^{24}Mg	136±7	147±8
^{25}Mg	27±3	27±3
^{26}Mg	28±3	29±3
^{27}Al	36±4	38±4
^{28}Si	119±6	131±7
^{29}Si	10±2	10±2
^{30}Si	9±2	9±2
^{31}P	9±2	9±2
^{32}S	21±3	23±3
^{33}S	4±1	4±1
^{34}S	5±1	5±2
^{36}S	1±1	1±1
^{35}Cl	5±1	5±2
^{36}Cl	3±1	2±1
^{36}A	6±1	6±2
^{37}A	2±1	1±1
^{38}A	5±1	4±2
^{40}A	1±1	1±1
^{39}K	4±1	4±1
^{40}K	3±1	3±1
^{41}K	3±1	3±1

	Detector ($\sim 4.5 gcm^{-2}$)	Top of Atmosphere
^{40}Ca	10±2	11±2
^{41}Ca	1±1	1±1
^{42}Ca	4±1	4±1
^{43}Ca	3±1	3±1
^{44}Ca	3±1	3±1
^{45}Sc	6±1	7±2
^{46}Ti	4±1	4±1
^{47}Ti	4±1	4±1
^{48}Ti	4±1	4±1
^{49}Ti	1±1	1±1
^{49}V	4±1	3±1
^{50}V	2±1	2±1
^{51}V	1±1	1±1
^{50}Cr	2±1	2±1
^{51}Cr	5±1	4±2
^{52}Cr	6±1	6±2
^{53}Cr	1±1	1±1
^{54}Cr	1±1	1±1
^{53}Mn	6±1	7±2
^{54}Mn	4±1	4±1
^{55}Mn	4±1	4±1
^{54}Fe	5±1	6±2
^{55}Fe	3±1	3±1
^{56}Fe	58±4	70±5
^{57}Fe	1±1	2±1
^{58}Ni	2±1	3±1
^{60}Ni	1±1	1±1

Abundances and Errors for Be, B, C and N from Maximum Likelihood Fit (Table II.2), Other Charge Abundances from Ormes et al. (1975); Isotopic Abundances from Silberberg and Tsao (1973); Errors Scaled from 2% for ^{16}O.

they may be propagated back through the atmosphere as is shown in figure III.14. By using the abundances at 3 g cm^{-2} instead of at the top of the atmosphere, we may compute correction factors to an atmospheric depth of 3 g cm^{-2}, as given in column E of table III.3, in order to facilitate comparisons with experiments performed at this depth. From table III.6 and figure III.14, it is evident that the relative abundance of the important isotope ^{10}Be is strongly affected by the atmosphere. The various percentage contributions to the ^{10}Be abundance observed at the detector are listed in table III.7.

In general, the percentage errors on the abundances are increased by the atmospheric correction. The major contribution to this increase often has nothing to do with uncertainties on the cross sections or abundances of other species. This may be seen by rewriting equation III.54 in the form

$$J_i(0) = \left({}^{A}D^{-1}\right)_{ii} J_i(X) + \sum_{k \neq i} \left({}^{A}D^{-1}\right)_{ik} J_k(X) \qquad \text{(III.55)}$$

Since the ${}^{A}D^{-1}{}_{ik}$ are always negative (i.e. subtracting from the observed abundance what has been produced in atmospheric spallation reactions), we see that the percentage errors will be increased by the factor

$$\frac{\left({}^{A}D^{-1}\right)_{ii} J_i(X)}{J_i(0)} \qquad \text{(III.56)}$$

in performing the atmospheric correction. This factor approaches unity for species whose abundances at the detector are mostly primary (i.e. have not interacted in the atmosphere). For such cases,

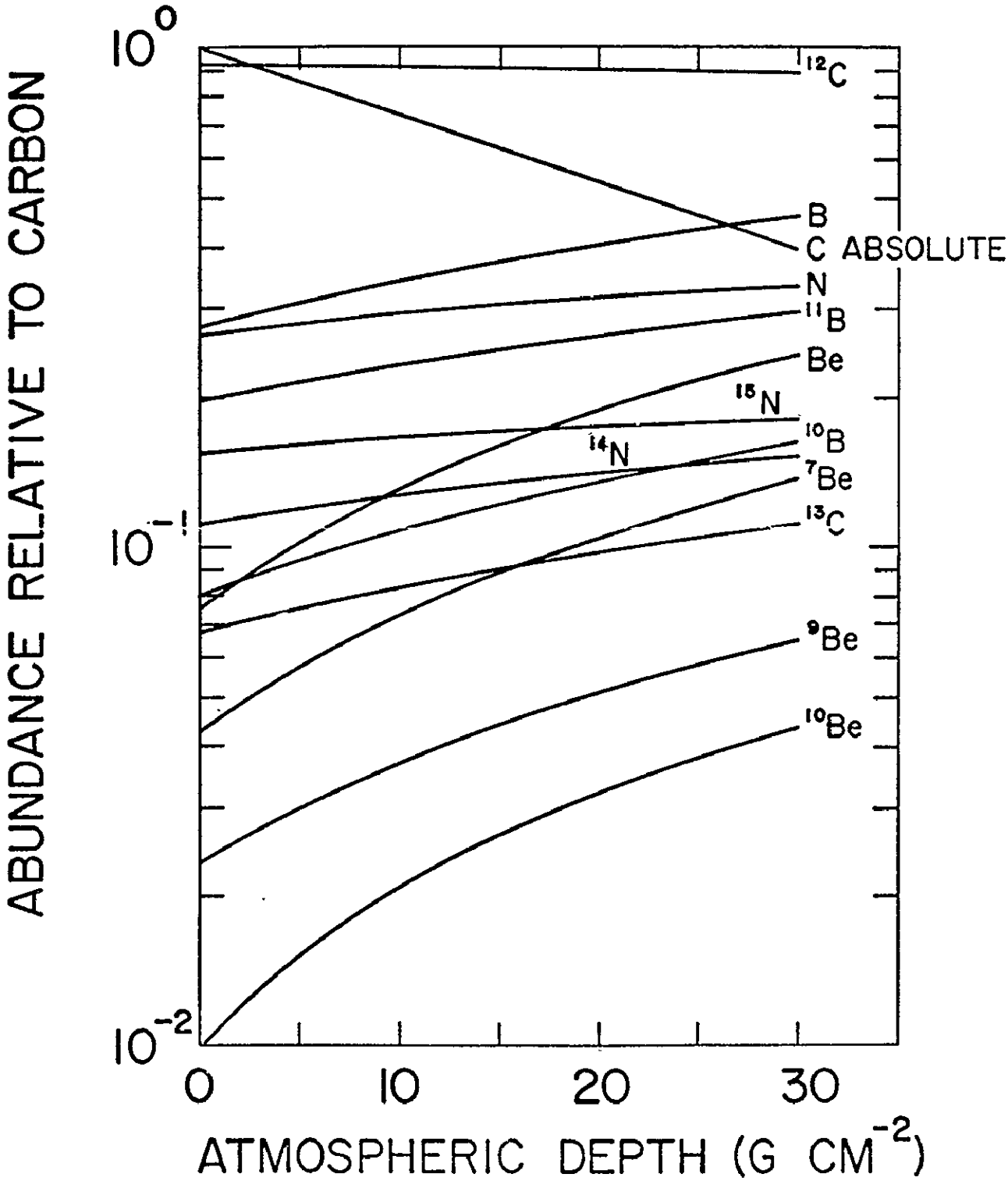

Figure III.14. Isotopic abundances relative to carbon as a function of depth in a slab model atmosphere.

ORIGINAL PAGE IS
OF POOR QUALITY

TABLE III.7

CONTRIBUTIONS TO OBSERVED ^{10}Be

Primary Isotope	Number of ^{10}Be per 10,000 Observed Originating in Atmospheric Interactions of Heavier Species
^{10}Be	6413
^{10}B	0
^{11}B	1118
^{12}C	741
^{13}C	84
^{14}N	60
^{15}N	175
O	594
F	26
Ne	132
Na	39
Mg	160
Al	34
Si	107
P	8
S	28
Cl	8
A	12
K	11
Ca	23
Sc	10
Ti	22
V	9
Cr	23
Mn	26
Fe	131
Co	0
Ni	6

$$\left({}^{A}D^{-1}\right)_{ii} J_i(X) \gg \sum_{k \neq i} \left({}^{A}D^{-1}\right)_{ik} J_k(X) \qquad \text{(III.57)}$$

Errors on the abundances of all species contributing to an observed abundance have been considered. In cases where the abundances at the detector have been inferred from the charge abundances measured by Ormes et al. (1975), the errors are taken to scale as $J_i^{\frac{1}{2}}$ with a 2% uncertainty for ^{16}O as the normalization. The uncertainties on the abundances both at the detector and as extrapolated to the top of the atmosphere are indicated in table III.3 and also table III.6.

4. Demodulation Corrections. Before any meaningful comparison of the results with model predictions can be made, the data must be corrected for the effects of solar modulation. Because of the large uncertainty involved in making this correction, it is not attempted in comparing with other experiments. It is only used for comparing the data with model predictions as discussed in Chapter IV. The procedure by which this correction is computed is completely analogous to that used for the energy correction discussed above. The model of Garcia-Munoz et al. (1975b), which was used to predict the local interplanetary spectra required for computing the energy corrections, also predicts spectral shapes in local interstellar space. Provided one can map the energy windows in which the experiment is sensitive to local interstellar space, relation III.44 may then be applied again with the substitution of interstellar spectra for the interplanetary spectra. The demodulation correction would then simply consist of the ratio of the correction to local interstellar space to the correction to local interplanetary space (i.e. the previous energy correction).

In order to extrapolate the energy windows to local interstellar space, it is required to understand the process of solar modulation. This process becomes increasingly important as the energy of a particle is decreased below ~ 1 GeV/nuc, and is thought to result in the virtual exclusion of particles below ~ 200 MeV/nuc. The process is not completely understood at the present time. Almost all current models, however, are derived from one first introduced by Parker (1958). In this approach, the modulation process is modeled in terms of a one dimensional diffusion of the cosmic rays into the solar system along magnetic field lines being convected outward from the sun by the solar wind. The quantitative formulation of the model is given by (see Parker 1958, 1963; Gleeson et al. 1968; Fisk et al. 1969 for further details)

$$\frac{1}{r^2}\frac{\partial}{\partial r}\left(r^2 V n_i^{CR}\right) - \frac{1}{r^2}\frac{\partial}{\partial r}\left(r^2 K \frac{\partial n_i^{CR}}{\partial r}\right) = \frac{1}{3r^2}\frac{\partial}{\partial r}\left(r^2 V\right)\frac{\partial}{\partial E}\left(\underline{\alpha} E n_i^{CR}\right) \tag{III.58}$$

where

$$\underline{\alpha} = 2 - \frac{1}{\gamma} = \frac{2E + mc^2}{E + mc^2} \tag{III.59}$$

n_i^{CR} is the number density of cosmic rays of species i, $V \approx 400$ km sec^{-1} is the velocity of the solar wind, r is the heliocentric distance, K is the parallel diffusion coefficient and E is the kinetic energy. Here the first term describes the convection of the cosmic rays in the solar wind, the second describes diffusive effects due to scattering of the cosmic rays from inhomogeneities encountered along the magnetic field lines, and the last term accounts for adiabatic energy losses in the expanding solar wind. This model deals only with motion confined entirely to the equatorial plane of the solar system, and thus ignores parameters which are

thought to be important, but have not yet been investigated experimentally (Cecchini et al. 1975, Fisk 1975, Moraal et al. 1975). Equation III.58 has been solved numerically by Fisk (1971). However, if the streaming of cosmic rays

$$\varphi_i^{CR} = \left[1 - \frac{1}{3n_i^{CR}} \frac{\partial}{\partial E}\left(\alpha E n_i^{CR}\right)\right] V n_i^{CR} - K \frac{\partial n_i^{CR}}{\partial r} \qquad \text{(III.60)}$$

vanishes, then it is possible to obtain an analytic solution to III.58. This is known as the force field solution, and is due to Gleeson and Axford (1968). The result may be formulated as

$$J_i^P(P_a, r_a) = J_i^P(P_b, r_b) \qquad \text{(III.61)}$$

where

$$\int dP\, P^2 J_i^P = \int dE\, J_i \qquad \text{(III.62)}$$

relates the differential rigidity and energy spectra, and

$$\int_{r_a}^{r_b} \frac{V dr}{3K_r} = \int_{r_a}^{r_b} \frac{K_P Z P\, dP}{E + mc^2} \qquad \text{(III.63)}$$

(with $K = \beta K_r K_P$ assumed) relates r_a and r_b. Thus the differential rigidity spectra at r_a and r_b are simply related to each other. Garcia-Munoz et al. (1975b) at the University of Chicago have used the numerical technique of Fisk (1971) to obtain forms of the diffusion coefficient, K, and interstellar differential energy spectra, J_i, which are consistent with the spectral shapes observed near the earth. The result is

$$K_r = \begin{cases} \infty & \text{for } r > 50\ \text{AU} \\ \exp\left[\left(\frac{r}{1\text{AU}} - 1\right)/33\right] & \text{for } r \leq 50\ \text{AU} \end{cases} \tag{III.64}$$

$$K_P = \left(\frac{P}{1\text{GV}}\right) \times 10^{22}\ \text{cm}^2\ \text{sec}^{-1} \qquad \text{for } P \geq 0.4\ \text{GV}$$

for

$$J_i \propto (E + 400\ \text{MeV})^{-2.6} \tag{III.65}$$

at the cosmic-ray source. Using equation III.64 for the diffusion coefficient, equation III.63 may be integrated to give the mean energy loss of particles penetrating from outside the solar cavity ($r_b \to \infty$) to the orbit of the earth ($r_a \sim 1$ AU):

$$E_b - E_a \cong 509\ Z\ \text{MeV} \tag{III.66}$$

We emphasize that equation III.66 gives only the average energy loss experienced by a particle of given Z, A and β in penetrating the solar cavity, and cannot be meaningfully applied to individual particles (e.g. see Goldstein et al. 1970).

The demodulation correction factors computed as described above (i.e. using the force field approximation to map the energy windows to the local interstellar space and assuming the interstellar spectral shapes calculated by Garcia-Munoz et al. 1975b) are listed in column F of table III.3, along with the extrapolated interstellar energy windows. Due to the uncertainty introduced by the process of solar modulation, the local interstellar spectra are not well known at low energies. The best one can say with any certainty, is that they probably lie somewhere between pure power laws in rigidity and pure power laws in total relativistic energy per nucleon (Ramadurai et al. 1972). It is thus desirable

to see the latitude which might be introduced by the assumption of various possible spectral shapes on the correction factors applied to the observed isotopic abundances. This has been done in table III.3 for the cases of interstellar spectra which are pure power laws in rigidity (total relativistic energy per nucleon, or Lorenz factor) with spectral index -2.60--column I(G)--and spectral index -2.75--column J(H). These can be compared to column F, which gives the correction factor we have actually used in correcting the data. This correction is based on more realistic forms of the interstellar spectra, and in particular takes account of differences in the spectra of primary and secondary components of the cosmic rays. Evidently, the various demodulation corrections all affect the isotopic abundances corresponding to a given element in roughly the same way. The major difference is in the pronounced charge dependence of the correction factors based on the assumption of rigidity power laws.

F. Discussion of Results.

The results of the present experiment are essentially contained in tables III.2 and III.3. Although the resolution is not quite good enough to see a separate peak for ^{10}Be, it is comparable to what has been reported by other experimenters. Since ^{10}Be and ^{9}Be are not clearly separated in the data, a fitting procedure has been relied upon to determine the relative abundances of Be isotopes. Furthermore, the uncertainty in the ^{10}Be abundance is increased from 25% to 40% by the presence of the atmosphere above the detector. The factor limiting the resolution is probably the detector normalization. This is closely related to the necessity of using semirelativistic particles to determine detector normalizations, and also differences in the scintillator response functions

from detector to detector. A detailed accelerator calibration of the instrument would thus be of immediate value in improving the resolution obtained.

G. Comparisons with Other Experiments.

In the following section, the results of the present experiment are compared with those of other experimenters. Experiments using the geomagnetic cutoff technique (Juliusson 1975, Dwyer et al. 1975) have been excluded from the comparison for the following reasons: 1) the geomagnetic cutoff experiments are generally performed at substantially higher energies ($\geq$ 0.7 GeV/nuc) than is the present experiment ($\sim$ 0.2 GeV/nuc); 2) the cutoff experiments so far have not yielded more than mean masses for the various elements although it is in principle possible to derive the actual isotopic composition (Peters 1974); and 3) the assumptions which go into the cutoff technique (especially with respect to energy spectra) are at best approximations, the reliability of which make the interpretation of the results somewhat uncertain. Insofar as a comparison <u>is</u> possible, however, there are no outstanding discrepancies between the present results and those of experiments using the geomagnetic rigidity cutoff technique.

In table III.8, we have compared the present data with the results of other experiments. Included are the pioneering results of Webber et al. (1973), which are balloon observations carried out at an atmospheric depth of $\sim$ 3 g cm^{-2} and about the same energy as the present experiment. This group has also recently reported results of an improved experiment (Preszler et al. 1975), which is also included in the table. Finally, the IMP 7 and IMP 8 results of Garcia-Munoz et al. (1975a) are also included. These are satellite observations taken outside the

TABLE III.8: COMPARISONS WITH OTHER EXPERIMENTS

Experiment	GSFC	NHAM-1	NHAM-2	GSFC	CHIC-1	CHIC-2
Corrections+	BCE	---	---	BCD	---	---
Energy (MeV/nuc)	~250	~200	~200	~250	~100	~100
Atmospheric Depth ($g cm^{-2}$)	(3.0)	2.9	3.1	(0)	0	0
Abundance Ratio:						
$^{7}Be/Be$	0.57 ±0.05	0.57	0.60	0.63 ±0.07	0.66 ±0.05	0.60 ±0.08
$^{9}Be/Be$	0.30 ±0.05	0.34	0.33	0.27 ±0.05	0.30 ±0.05	0.40 ±0.06
$^{10}Be/Be$	0.13 ±0.04	0.09	0.08	0.10 ±0.04	0.04 +0.08 -0.04**	0.00 +0.04 -0.00**
Be/C	0.087±0.007	0.087*	0.085	0.079±0.009	0.056±0.003	0.063±0.004
$^{10}B/B$	0.30 ±0.04	0.25	0.33	0.33 ±0.04	0.36 ±0.02	0.33 ±0.03
$^{11}B/B$	0.70 ±0.04	0.75	0.67	0.67 ±0.05	0.64 ±0.03	0.67 ±0.04
B/C	0.293±0.014	0.240	0.263	0.273±0.018	0.258±0.007	0.246±0.009
$^{12}C/C$	0.93 ±0.03			0.93 ±0.03		
$^{13}C/C$	0.07 ±0.01			0.07 ±0.01		
C/C	1.000±0.026		1.000	1.000±0.036	1.000±0.014	1.000±0.017
$^{14}N/N$	0.42 ±0.08		0.40	0.43 ±0.09		
$^{15}N/N$	0.58 ±0.07		0.60	0.67 ±0.08		
N/C	0.275±0.017		0.271	0.290±0.026	0.229±0.007	0.228±0.008

*Normalization **90% Confidence Limit
+See table III.3

GSFC	This Experiment	NHAM-2	Webber et al. (1975)	
NHAM-1	Webber et al. (1973)	CHIC-1	Garcia-Munoz et al. (1975)	IMP 7
		CHIC-2	Garcia-Munoz et al. (1975)	IMP 8

ORIGINAL PAGE IS
OF POOR QUALITY

atmosphere and magnetosphere of the earth, at energies roughly half those at which the present data are taken. The results of these various experiments are referred to by NHAM-1, NHAM-2, CHIC-1 and CHIC-2, respectively. In each case, our results have been corrected in such a manner as to be most consistent with these observations at the respective detectors. In particular, the present data have been corrected to an atmospheric depth of 3 g cm^{-2} (column E of table III.3) for comparisons with NHAM-1 and NHAM-2, and to the top of the atmosphere (column D of table III.3) for comparisons with CHIC-1 and CHIC-2. In all cases, the data have been corrected for interactions in the detector (column C of table III.3) and for energy windows assuming that the energy spectra of all isotopes have the same shape as that of ^{12}C (column B of table III.3). The agreement among the various experiments considered in table III.7 is generally quite good. The only significant discrepancy among the relative isotopic abundances reported concerns the isotope ^{10}Be. All of the results reported are consistent with $\frac{^{10}Be}{Be} \cong 0.6$, except for those of CHIC-2, which are most consistent with the complete absence of ^{10}Be. The low ^{10}Be abundance observed by CHIC-2 is compensated by the largest $\frac{^{9}Be}{Be}$ ratio of any of the experiments reported. All the remaining discrepancies concern the relative charge abundances. These are as follows: 1) CHIC-1 and CHIC-2 both obtain a smaller value of the ratio Be/C than does either NHAM-2 or the present experiment; 2) the present experiment observes the largest B/C ratio of any of the results reported; and 3) CHIC-1 and CHIC-2 both observe a smaller N/C ratio than does either NHAM-2 or the present experiment. Finally, we note that the present results agree reasonably well with other results on the charge composition obtained at similar energies (e.g. see Shapiro et al. 1973). There is also a reasonable agreement with the results of Ormes et al. (1975), which were

obtained from the same experiment (in the C x S mode of analysis) at somewhat higher energies ($\geqslant$ 570 MeV/nuc) and with superior statistical weight.

Let us now consider the degree of consistency of the results presented in table III.8. In particular, we will concentrate on the ratio $\frac{^{10}Be}{Be}$, which represents the only significant discrepancy among the relative isotopic abundances compared.

We first note that all of the results except CHIC-2 would be consistent with the value $\frac{^{10}Be}{Be} \simeq 0.06$ at the top of the atmosphere. Of the other results, the largest deviation from this value is by the present experiment, which is one standard deviation high. We recall from the discussion in section C.5 that our observed ^{10}Be abundance may be reduced by about one standard deviation if we assume that some of the observed ^{10}Be is due to an asymmetry in the ^{9}Be mass distribution. Although such an effect would considerably reduce the scatter in $\frac{^{10}Be}{Be}$ among experiments other than CHIC-2, it cannot by itself make the present result consistent with the complete absence of ^{10}Be in the cosmic rays. The above consideration represented the only reasonable possibility for error in our observed value of $\frac{^{10}Be}{Be}$. Other possibilities which were considered not probable included a breakdown in the mass scaling of the variance selection threshold and the standard response curves, and an error in the atmospheric correction to the data due to the use of erroneous cross sections. Thus it is quite difficult to see how the present experiment could be made consistent with $\frac{^{10}Be}{Be} \rightarrow 0$. In particular, only an improbably large error in the atmospheric correction could at once make the present results and those of NHAM-1 and NHAM-2 consistent with the absence of ^{10}Be. However, this seems to be very unlikely.

We next observe that, while the Chicago group observes the smallest value of $\frac{^{10}Be}{Be}$ at the lowest energies (~ 100 MeV/nuc), the present experiment observes the largest value at the highest energies (~ 250 MeV/nuc). Thus there exists the possibility of a real energy dependence of the ratio $\frac{^{10}Be}{Be}$. One possibility for understanding such an energy dependence can be seen from the assumption that the mean pathlength traversed by cosmic rays, λ_e, is a constant independent of energy, at least below 1 Gev/nuc. In this case, equation I.1 predicts that the mean confinement time of cosmic rays in the galaxy, τ_e, will vary as $1/\beta$. A second effect which may contribute concerns the energy dependences of the various cross sections for the production of ^{10}Be from interactions of heavier species with the interstellar medium. Both of these points have been taken into account in the propagation calculations of Garcia-Munoz et al. (1975b) which predict a decrease in the ratio $\frac{^{10}Be}{Be}$ of about 20% in going from 250 MeV/nuc to 100 MeV/nuc. This of course assumes a mean energy loss of ~ 250 MeV/nuc per particle in penetrating the solar cavity. If we disregard solar modulation, then the ratio $\frac{^{10}Be}{Be}$ changes by 50% between 250 and 100 MeV/nuc. Clearly even this is inadequate to explain the observations. Thus if there exists a real energy dependence of the ratio $\frac{^{10}Be}{Be}$, then there appears to be no ready explanation for its magnitude.

Before concluding, we wish to make a few general remarks with respect to the various experiments. Both the present experiment and those of the University of New Hampshire group are balloon borne experiments performed under a residual layer of the earth's atmosphere. The IMP 7 and IMP 8 experiments of the Chicago group, on the other hand, are performed well outside the atmosphere and thus avoid any effects of the atmosphere on the observed data. However, we have seen that the cross

sections used to make the atmospheric corrections to the present data are not likely to be sufficiently in error to have a significant effect. Thus the principle disadvantage imposed by the presence of the atmosphere is to increase the uncertainty of the observed ^{10}Be abundance from 25% to 40% after extrapolation to the top of the atmosphere. On the other hand, the present experiment and those of the University of New Hampshire group are performed at significantly higher energies than are those of the University of Chicago. Although this does not directly affect the measurement, it does significantly affect its interpretation. This follows since a highly uncertain correction for the effect of solar modulation is required before a meaningful comparison with theory is possible, and the uncertainty of this correction increases with decreasing energy. Finally, we feel that the means by which background is removed in the present experiment is superior to that used by either of the other groups. This derives essentially from the fact that only the present experiment is capable of "continuously" monitoring the identity of a particle over its entire trajectory in the experiment.

CHAPTER IV

DISCUSSION OF RESULTS

Once the experimental results have been derived and corrected to yield isotopic abundances in the local interstellar medium, comparisons may be made with the predictions of the various models for the propagation and origin of cosmic rays. Although some models have been proposed in which the cosmic rays fill some extended region of extragalactic space (e.g. see Setti et al. 1971, Brecher et al. 1971 and Sitte 1972), most current models propose the confinement of the cosmic rays either to the galactic disk or some extended region (known as the galactic halo) surrounding it. The actual existence of the galactic halo is highly controversial, and it is an objective of the present thesis to definitively answer the question of whether it is required in order to confine the cosmic rays.

A. The Diffusion Model

1. Halo Model. Most currently popular models for the propagation of cosmic rays in the galaxy are based upon the diffusion model first introduced by Ginzburg (Ginzburg et al. 1964). The essential observation is that although cosmic rays of all but the highest energies (i.e. $E \leqslant 10^{14}$ eV/nuc) are constrained to closely follow magnetic field lines through the interstellar medium, these field lines are sufficiently randomly oriented in space that even a very small drift (or scattering) across the field lines (as would be caused by irregularities encountered in the magnetic field) essentially randomizes the trajectory of a particle through space. Ginzburg postulated that the cosmic rays originated in the galactic disk, probably as a result of supernova events, then diffused freely throughout a quasi-spherical region surrounding the disk known as

the galactic "halo". Although the magnetic field intensity and gas density postulated to exist in the halo ($\sim 10^{-8}$ gauss and $\sim 10^{-2}$ cm^{-3}, respectively) are two orders of magnitude less than those characteristic of the disk ($\sim 10^{-6}$ gauss and 1 cm^{-3}), particles were imagined to both escape from the disk into the halo and re-enter the disk freely. Ginzburg found that a diffusion coefficient given by $K_H \cong 10^{29}$ cm^2 sec^{-1} to be appropriate for such a model. This results in an effective scattering mean free path given by $\lambda_H \cong \frac{3K_H}{c} \cong 3pc$, and a mean escape time for cosmic rays from the halo given by $\tau e \cong \frac{r_H{}^2}{2K_H} \cong 2 \times 10^8$ yr (where $r_H \cong 12$ kpc) is the halo radius. This gives a reasonable value for the mean pathlength traversed by cosmic rays ($\lambda_e \cong 5$ g cm^{-3}) as deduced from the abundances of the elements Li, Be and B (presumed to be absent in the source) relative to their progenitors, such as C and O. In addition, the scattering mean free path obtained is of the same order as the inhomogeneities observed in the galactic magnetic fields (Allan 1972). Finally, the cosmic rays are scattered sufficiently before observation ($\sim 10^7$ times) to lose all memory of their points of origin (i.e. source locations), which is important in order to reproduce the high level of isotropy observed in the cosmic rays. A further advantage of such a model is that it considerably reduces (by a factor $\sim 10^4$) the time required for particles to escape from the system, and thus considerably reduces the energy requirement on the cosmic-ray sources (i.e. the rate at which they must produce cosmic rays in order to replace those escaping and, thus, maintain the cosmic-ray density at a constant level). In quantitative terms, for the observed cosmic-ray energy density $w_{CR} \cong 1$ eV cm^{-3}, the power required of the cosmic-ray sources is $P_{CRS} \cong 5 \times 10^{40}$ erg sec^{-1} for a halo volume of $\sim 2 \times 10^{68}$ cm^3. For comparison the power available

from supernova explosions is $P_{SN} \leqslant 10^{41}$ erg sec^{-1}, assuming a supernova rate of $\leqslant$ 1/50 years and $\leqslant 10^{50}$ erg/supernova in cosmic rays produced. The power required of the cosmic-ray sources in the case where cosmic rays freely escape from the galaxy is $\sim 10^4$ times that required in the Ginzburg diffusion model, as may be seen by comparing τ_e and r_H/c. Thus it is clear that supernovae can be the primary source of energy for cosmic rays in the galaxy only if there is some mechanism available to restrict their escape, as (for example) diffusion in the Ginzburg model. This is important since supernovae are among the most powerful local sources of energy we can imagine.

It is apparent from the foregoing discussion that the model of Ginzburg, which postulates diffusion of the cosmic rays in a galactic halo, meets the main requirement of a cosmic-ray propagation model. It is possible to reproduce the characteristic mean pathlength traversed by cosmic rays ($\lambda_e \sim 5$ g cm^{-2}) and also their high degree of isotropy ($\delta \leqslant 10^{-4}$ for $E \geqslant 100$ GeV/nuc; Allan 1972). At the same time, the cosmic rays are confined in the galaxy sufficiently long that an unreasonable burden is not placed on the sources. This is all accomplished with a diffusion coefficient $K_H \sim 10^{29}$ cm^2 sec^{-1} in a halo of radius $r_H \sim$ 12 kpc with gas density $n_H \sim 10^{-2}$ cm^{-3} and magnetic field intensity $B_H \sim 10^{-8}$ gauss, all of which is quite reasonable. Halos have been observed around various other galaxies (not by any means all, however) by means of the synchrotron radio emission of the cosmic-ray electrons trapped in them (Baldwin 1954). The existence of a similar halo around our own galaxy, however, is by no means firmly established and is, in fact, strongly questioned by radio astronomers (Burke 1967).

2. <u>Disk Model</u>. The disk model, a variant on the halo diffusion

model of Ginzburg, would confine the cosmic rays predominantly to the galactic disk (Owens 1975; Dickinson et al. 1975), and thus circumvent the problem imposed by the failure to observe a galactic radio halo around our own galaxy. We note that this model does not preclude the existence of a cosmic-ray halo, but merely postulates that the re-entry of cosmic rays into the disk from the halo is negligible. Both the gas density and the magnetic field intensity in the disk ($n_D \sim 1$ cm^{-3} and $B_D \sim 10^{-6}$ gauss, respectively) are about two orders of magnitude greater than the values characteristic of the halo. The former consideration requires an escape time two orders of magnitude smaller than that in the halo model (i.e. $\tau_e \cong 2 \times 10^6$ yr) if the observed mean pathlength traversed by the cosmic rays ($\lambda_e \cong \langle m \rangle n_D c \tau_e \cong 5$ g cm^{-2}) is to be maintained. Since most particles will reach the top or bottom face of the disk before reaching its circumference, the half thickness of the disk ($z_D \cong 0.25$ kpc) replaces the halo radius in relating the escape time to the diffusion coefficient: $\tau_e \cong \frac{3z_D^2}{2K_D}$. We thus deduce a diffusion coefficient, $K_D \cong 10^{28}$ cm^2 sec^{-1}, which is an order of magnitude smaller than that appropriate to the halo model. This corresponds to a correspondingly smaller effective scattering mean free path, $\lambda_D \cong \frac{3K_D}{c} = 0.3$ pc. In this model, the power required of the cosmic-ray sources, $P_{CRS} \cong 1.5 \times 10^{41}$ erg sec^{-1} is only three times that required in the halo model, and still within reason.

The halo and disk diffusion models for the propagation of cosmic rays which have been discussed above characterize the two extremes of a continuum of models in which the halo is gradually flattened, and eventually merges into the disk. All of these models can be made consistent with observations. Perhaps the most sensitive test of which model is correct would be the direct determination of the mean matter density, n, in the

region where the propagation takes place, or alternatively the mean escape time, τ_e, to which it is inversely proportional (by virtue of the known leakage pathlength, $\lambda_e \cong \langle m \rangle$ nc τ_e). The radioactive secondary isotope, ^{10}Be, with a mean decay time, $\tau_d = 2.2 \times 10^6$ yr, provides an ideal tool for doing this.

Other variations on the basic diffusion model have also been proposed. These include the assumption of boundary layers (i.e. for the disk, halo, etc.) which are either partially or totally reflective. Such boundaries may, for instance, be set up by self-generated magnetohydrodynamic waves. One may also replace the continuous distribution of sources in space and time by a more realistic distribution of discrete sources, which is especially important in the case where one of the discrete sources happens to be quite nearby. Diffusion in only one dimension (i.e. along magnetic field lines) may also be considered, or alternatively "compound diffusion" in which one considers separate diffusion processes for the random walk of magnetic field lines in space and the motion of particles along the field lines. As a final example, one may consider multiple confinement regions, each of which is characterized by a different magnetic field intensity and gas density. In particular, supernova envelopes with characteristically high gas densities and magnetic field intensities may well surround the cosmic-ray sources. The cosmic rays would then be required to escape from these before entering the galactic disk.

B. The Leaky Box Approximation

A rather general formulation of cosmic-ray transport in the diffusion model is given by

$$Q_i(\vec{p},\vec{r},t)$$

$$= \frac{\partial}{\partial t} J_i(\vec{p},\vec{r},t) + \frac{\partial}{\partial \vec{p}} \cdot \left[J_i \left(\frac{d\vec{p}}{dt} \right)_i \right] + \frac{\partial}{\partial \vec{r}} \cdot \left[-\overleftrightarrow{K}_i(\vec{p},\vec{r},t) \cdot \frac{\partial J_i}{\partial \vec{r}} \right] \tag{IV.1}$$

where $J_i(\vec{p},\vec{r},t)$ represents the differential flux of cosmic rays of species i and momentum $\vec{p}$ at position $\vec{r}$ and time t. $Q_i(\vec{p},\vec{r},t)$ represents the source function for species i, and includes production and loss in nuclear interactions and radioactive decay, and $\overleftrightarrow{K}_i$ is the diffusion tensor for species i. If the cosmic-ray flux is isotropic, we may then replace $\vec{p}$ by γ everywhere in equation IV.1, noting that

$$J_i(\vec{p},\vec{r},t)\, p^2 dp = J_i(\gamma,\vec{r},t)\, d\gamma \tag{IV.2}$$

relates the differential momentum and energy spectra. It is usual to replace the diffusion tensor by a scalar since there are no distinguishable directions in the problem. Furthermore, the diffusion coefficient is often taken to be independent of γ, $\vec{r}$ and t. To the best of our knowledge, the cosmic-ray intensity, J_i, has been constant over at least the last $\sim 10^9$ yr (Van Loon 1973), so that it is reasonable to formulate a steady state model by neglecting the first term of equation IV.1. Consider next the second term. For $\gamma \gtrsim 1.5$, we may put

$$\begin{aligned} \frac{d\gamma}{dt} &\cong \rho\beta c \left(5\,\mathrm{MeV}\, g^{-1} cm^2\right) \left(\frac{Z^2}{A m_p c^2} \right) \\ &\cong (1 \times 10^{-3}) \rho c A \end{aligned} \tag{IV.3}$$

Assuming energy spectra which are power laws in total energy per nucleon of spectral index ~ -2.7, we have

$$\frac{\partial}{\partial \gamma} \left[\frac{d\gamma}{dt} J_i(\gamma,\vec{r},t) \right] \cong (4 \times 10^{-3}) \frac{\rho c A J_i}{\gamma} \tag{IV.4}$$

For comparison, one term which contributes to Q_i is the loss to nuclear interactions. Taking the total inelastic cross section to be $\sigma_{tot} \cong 50\ A^{2/3}$mb, this term is

$$J_i\, n\, c\, \beta\, \sigma_{tot} \cong (3\times10^{-2})\, \rho\, c\, A^{2/3} J_i \tag{IV.5}$$

We thus see that the second term of equation IV.1 is negligible for $\gamma \gtrsim 1.5$, at least at the 10% level. After applying all of the approximations discussed above, equation IV.1 is reduced to

$$-\frac{\partial}{\partial \vec{r}} \cdot \left[K_i \frac{\partial J_i}{\partial \vec{r}} \right] = Q_i(\gamma, \vec{r}) \tag{IV.6}$$

which is a commonly used formulation of the diffusion model. We have already seen in section II.A that the mean time for cosmic rays to escape from the system in the halo (disk) model is $\sim 2 \times 10^8$ yr ($\sim 2 \times 10^6$ yr), which corresponds to a total distance traveled of $\sim$ 60 Mpc ($\sim$ 0.6 Mpc). This is $\sim$ 5000 (2000) times the distance to the nearest boundary, and suggests a picture in which the cosmic rays approach the boundaries often in their lifetimes with a low probability of escape each time. A reasonable approximation in this case is to neglect the positional dependences and integrate equation IV.6 over all space interior to the boundaries:

$$\oint_V dV \frac{\partial}{\partial \vec{r}} \cdot \left[K_i \frac{\partial J_i}{\partial \vec{r}} \right] = \oint_S d\vec{S} \cdot K_i \frac{\partial J_i}{\partial \vec{r}} \cong \frac{-V \bar{J}_i(\gamma)}{\tau_e} \tag{IV.7}$$

Here the surface integral is interpreted as the rate at which particles cross the boundary surface, and is approximated by the last equality. Here $\bar{J}_i(\gamma)$ is the mean differential cosmic-ray intensity inside the boundary and τ_e is the mean time it takes a typical cosmic-ray particle

to leave the bounded volume. We may now write the result

$$\bar{Q}_i(\gamma) = \frac{\bar{J}_i(\gamma)}{\tau_e} \tag{IV.8}$$

This is known as the leaky box model of cosmic-ray propagation. It may be interpreted in terms of a leaky box (i.e. the boundary surface) in which the cosmic rays are confined. The probability that a given cosmic ray will escape from the box (i.e. leak out) in time dt is merely $\frac{dt}{\tau_e}$, and this loss is exactly compensated by the production of $\bar{Q}_i(\gamma)dt$, new cosmic rays, either directly by sources or in the spallation (or radioactive decay) of heavier species. The leakage time, τ_e, may be related to the diffusion coefficient, K, according to

$$\tau_e \cong \frac{r_{char}^2}{2K} \cong \begin{cases} 2\times10^8\,yr & \text{halo model} \\ 2\times10^6\,yr & \text{disk model} \end{cases} \tag{IV.9}$$

where r_{char} is the net distance a particle must propagate from its source (on the average) in order to cross the boundary. We have assumed that the diffusion coefficient K (and hence also τ_e) is independent of species. We proceed by expanding the source term, $\bar{Q}_i(\gamma)$, in equation IV.8 to show explicitly the contributions of production and loss in nuclear spallation reactions and radioactive decays:

$$\frac{\bar{J}_i(\gamma)}{\tau_e} = \bar{Q}_i(\gamma)$$

$$= \bar{Q}_i^s(\gamma) + \sum_j \left[nc\beta \langle \sigma_{ij}^k \rangle_k + \frac{1}{\gamma\tau_d(j\to i)} \right] \bar{J}_j(\gamma) - \left[nc\beta \langle \sigma_{tot}(A_i, A_k) \rangle_k + \frac{1}{\gamma\tau_d(i\to *)} \right] \bar{J}_i(\gamma) \tag{IV.10}$$

Here $\bar{Q}_i^s$ denotes that part of the source term which is directly due to cosmic-ray sources, and specifically does not include nuclear spallation or radioactive decay. $\langle \rangle_k$ denotes an average over the target atoms in the confinement volume (V), n is the number density of such targets and

$\tau_d(j \to i) \ll \frac{\bar{J}_j}{\bar{J}_i} \tau_e$ is required. The divergence of the term $\tau_d^{-1}(i \to *)$ $\bar{J}_i$ in equation IV.10 then requires either that $J_i(\gamma) \to 0$ with $\tau_d(i \to *)$ or that $\bar{Q}_i^s$ become large in order to balance the divergence of this term. The latter alternative is clearly unphysical except as an extreme assumption. Consequently, $J_i(\gamma) \to 0$ and species i does not contribute significantly to any other species except the one to which it decays, species j. Thus species i may be absorbed into species j by the substitutions

$$\sigma_{jm}^{k} \longrightarrow \sigma_{jm}^{k} + \sigma_{im}^{k} \tag{IV.13}$$

and

$$\bar{Q}_j^s \longrightarrow \bar{Q}_j^s + \bar{Q}_i^s \tag{IV.14}$$

Radioactive isotopes which do not clearly fall into either of the two categories described above (i.e. long or short mean lifetime against decay) are most rigorously retained as they appear in the calculation. However, it often happens that such isotopes contribute negligibly to the production of other species (through the partial cross sections, σ_{ij}^k) because of their relatively low abundances. In such cases, $\tau_d(j \to i) \to \infty$ may still be an adequate approximation for the calculation of the source abundances, $\bar{Q}_i^s(\gamma)$, from equation IV.11 as a function of the leakage pathlength, λ_e. The calculation may then be inverted using the actual value of $\tau_d(j \to i)$ in order to determine the gas density, n, in the propagation region, or equivalently the mean escape time, τ_e. This will, in fact, be the approach taken below for the case of ^{10}Be. It should be noted that the approximations of long or short lifetimes of radioactive isotopes against decay as described above are not required in order to apply equation IV.11 to the data. In particular, they do not serve to

eliminate from the problem any unknowns which would otherwise prevent its solution. The main advantage of the approximations lies in the resulting simplifications, particularly in the number of species which must be considered in constructing the leaky box propagator matrix, ${}^{LB}D$.

1. Pathlength. The application of the leaky box model to the interpretation of experimental data is now a simple matter. One has only to calculate the leaky box propagator matrix, ${}^{LB}D$, for assumed values of the leakage lifetime, τ_e, and the density of matter in the confinement region, n. Given the observed abundances of the arriving cosmic rays, $\bar{J}_i(\gamma)$, the source abundances, $\bar{Q}_i^s(\gamma)$, may then be calculated. The values of τ_e and n are then adjusted so that the abundances of all components assumed absent in the source actually do vanish. Examples of such isotopes would be those of Li, Be and B (which cannot survive in the hot environment of a star), and perhaps also isotopes such as ${}^{13}C$ and ${}^{15}N$, which are not easily produced in the chains of nuclear reactions thought to be relevant to the cosmic-ray nucleosynthesis.

Various authors have applied the leaky box model, essentially as formulated above, to the interpretation of the observed charge composition of the cosmic rays (e.g. see Shapiro et al. 1973). In such cases, it is also required to make assumptions regarding the isotopic composition of the various elements in the cosmic rays, either at the source or as observed. This is usually done using the observed solar system abundances (Cameron 1973) as a standard. The results are insensitive to the survival or decay of the few radioactive isotopes for which it is questionable, so that only the leakage pathlength, λ_e, is determined with any precision. The results range from $\lambda_e \sim 3$ g cm^{-2} to $\lambda_e \sim 7$ g cm^{-2} at moderate energies of a few hundred MeV/nuc to a few GeV/nuc. Results at

$\tau_d(j \to i)$ denotes the mean lifetime against radioactive decays taking species j to species i (* denotes "anything"). As formulated in equation IV.10, the leaky box models have two characteristic parameters which may be adjusted in order to achieve the optimum agreement with observations: the leakage time, τ_e, and the number density of target atoms in the "box", n. The relative abundances of the various target atoms are assumed to be sufficiently well known (i.e. ~ 90% H and 10% He by number) as to introduce no extra degrees of freedom. For stable isotopes not subject to radioactive decay, $\lambda_e = \rho\beta c\tau_e = \langle m\rangle\beta c(n\tau_e)$ is the only free parameter ($\langle m\rangle$ is the mean mass of the target atoms). We note that equation IV.10 is a matrix equation for the source abundances, $\overline{Q}_i^s(\gamma)$, in terms of the observed cosmic-ray abundances, $\overline{J}_i(\gamma)$, i.e.

$$\overline{Q}_i^s(\gamma) = \sum_j \left({}^{LB}D^{-1}\right)_{ij} \overline{J}_j(\gamma) \tag{IV.11}$$

where

$$\left({}^{LB}D^{-1}\right)_{ij} = \left[nc\beta\langle\sigma_{ij}^{k}\rangle_k + \frac{1}{\gamma\tau_d(j\to i)}\right] - \left[\frac{1}{\tau_e} + nc\beta\langle\sigma_{tot}(A_i, A_k)\rangle_k + \frac{1}{\gamma\tau_d(i\to *)}\right]\delta_{ij} \tag{IV.12}$$

defines the leaky box propagator matrix.

The application of equations IV.10 through IV.12 to the interpretation of experimental data is often facilitated by various assumptions regarding the stability of the radioactive isotopes. The terms involving τ_d $(j \to i)$ may be altogether neglected in equations IV.10 through IV.12 if the lifetime against radioactive decay is sufficiently long. The condition for this approximation to hold is $\tau_d(j \to i) \gg \tau_e$ if $\overline{J}_j(\gamma) \leq \overline{J}_i(\gamma)$; otherwise, τ_d $(j \to i) \gg \frac{\overline{J}_j}{\overline{J}_i}\tau_e$ is required. If the radioactive decay is very rapid, on the other hand, one may put $\tau_d(j \to i) \cong 0$. The condition for this to hold is τ_d $(j \to i) \ll \tau_e$ if $\overline{J}_j(\gamma) \geq \overline{J}_i(\gamma)$; otherwise

higher energies seem to indicate a systematic decrease in λ_e as one goes to progressively higher energies (Lezniak et al. 1975, Juliusson et al. 1975).

The results of a similar calculation, as applied to the present results, are shown in figure IV.1. Here the cosmic-ray source abundances are computed as a function of the assumed value of the leakage pathlength, λ_e, on the assumption that ^{10}Be is stable. The cross sections used in this calculation are based on the same formulae as were used in computing the atmospheric corrections (section III.E.3). The cross sections have been computed based on an assumed propagation energy E = 600 MeV/nuc, and assuming the composition of the interstellar medium to be 10% helium and 90% hydrogen by number. The assumptions regarding the stability of the various isotopes considered in the calculation are given in table IV.1. For each isotope, the range of source abundances consistent with zero has been determined based on the statistical errors assigned to the observed isotopic abundances based on the maximum likelihood method. This is indicated by the darkened portion of the curve for each isotope. The dashed extensions to these error limits also take into account estimated uncertainties in the cross sections used in the calculation, estimated to be ~ 10% for total cross sections and ~ 15% for partial cross sections. This has been carried through the corrections for interactions in the detector and the atmosphere as well as the leaky box propagation. The best value of λ_e for each isotope (assuming it is entirely secondary in origin) is that at which its source abundance is exactly zero. The error limits on λ_e are then estimated from the range of values of λ_e for which the calculated source abundance is consistent with zero, i.e. that range over which the curves in figure IV.1 are

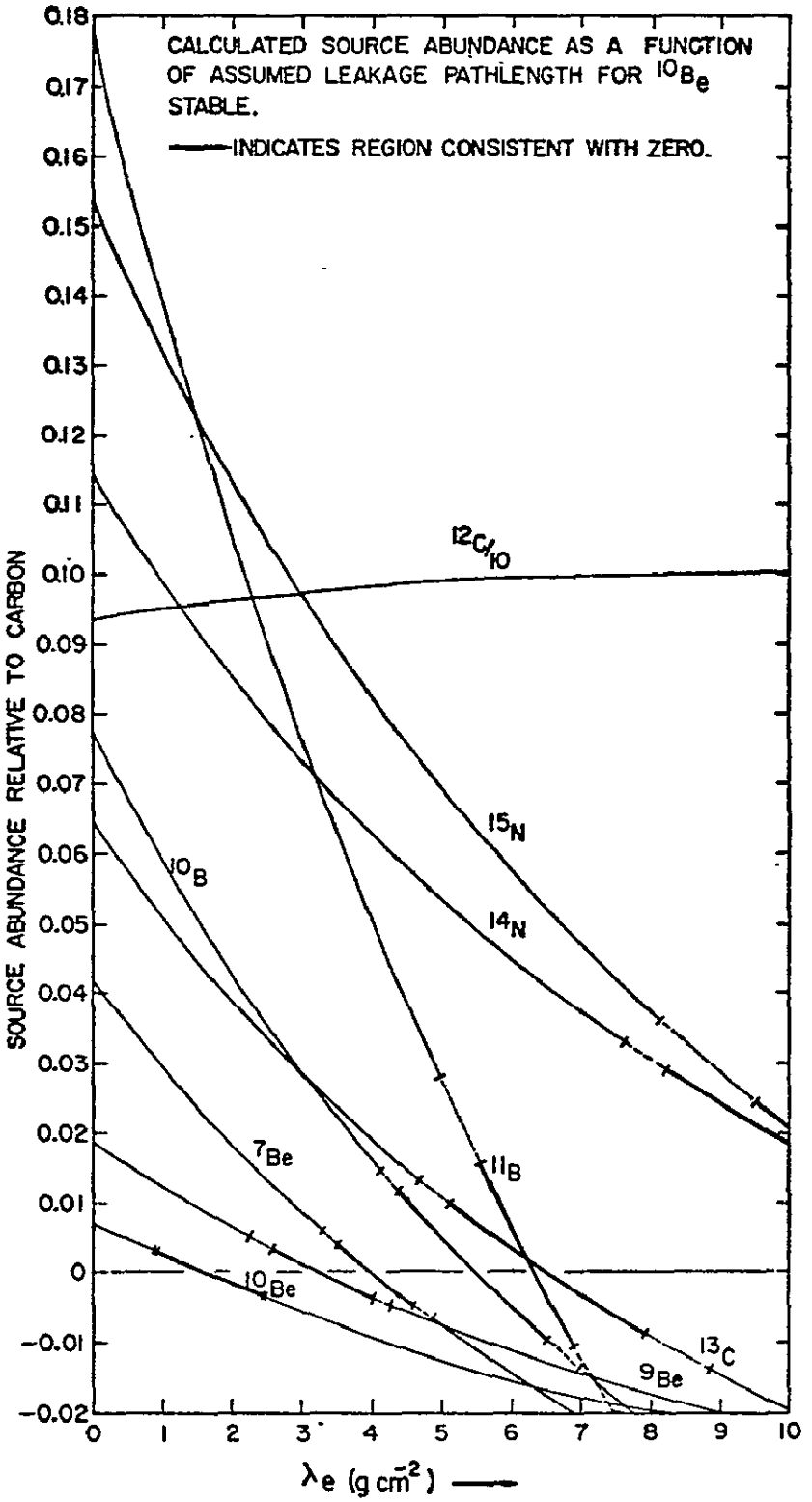

Figure IV.1. Isotopic abundances at the cosmic-ray source relative to carbon as a function of mean leakage pathlength, λ_e, assumed. ^{10}Be assumed stable. Heavy portions of curves indicate values consistent with zero if only uncertainties on isotopic abundances are considered. Dashed extensions include effects of cross section uncertainties assumed to be 10% for total and 15% for partial cross sections.

TABLE IV.1: Stability Selections in the Interstellar Medium

Z: \ N:	3	4	5	6	7	8	9	10	11	12	13	14	15	16	17	18	19	20	21	22	23	24	25	26	27	28	29	30	31	32	33	34	35	36
4	2		2	2	3	3																												
5			2	2	3	3																												
6		1	1	2	2	3	3	3																										
7			1	1	2	2	3	3	3																									
8			1	1	1	2	2	2	3	3																								
9					1	1	1	2	3	3	3																							
10					1	1	1	2	2	2	3	3																						
11						5	1	1	1	2	3	3	3																					
12							1	1	1	2	2	2	3	3																				
13									1	1		2	3	3	3																			
14									1	1	1	2	2	2	3	3																		
15											1	1	1	2	3	3	3																	
16											1	1	1	2	2	2	3	2	3	3														
17													1	1	1	2	3	2	3	3	3													
18													1	1	1	2	2	2	3	2	3	3	3											
19															1	1	1	2	2	2	3	3	3	3	3	3								
20															1	1	1	2	2	2	2	2	3	2	3	2	3	3						
21																	1	1	1	1	1	2	3	3	3	3	3	3						
22																	1		1	1	1	2	2	2	2	2	3	3						
23																				1	1	1	1	2	2	2	3	3	3					
24																				1	1	2	1	2	2	2	2	2	3	3				
25																							1	1	1	2	1	2	3	3	3			
26																								1	1	2	2	2	2	2	3	3	3	
27																									1	1	1	2	1	2	3	3	3	3
28																										2	1	2	2	2	2	2	3	2

Decay Codes

1. e^+ Emission
2. Stable
3. e^- Emission
4. n Emission
5. p Emission
6. α Emission

All Decays Presumed Instantaneous

ORIGINAL PAGE IS
OF POOR QUALITY

darkened. The resulting estimates of the leakage pathlength for each isotope measured are tabulated in table IV.2, and illustrated in figure IV.2. These results are compatible with those of other authors, and apparently indicate a real discrepancy between the values of the leakage pathlength obtained based on the Be isotopes (i.e. $\lambda_e \cong 3.5$ g cm^{-2}) and those obtained using other isotopes (i.e. $\lambda_e \cong 6$ g cm^{-2}). We also note that the only isotopes which significantly affected by the survival or decay of ^{10}Be are ^{10}Be itself and, to a much lesser extent, ^{10}B. Thus the leakage length obtained for ^{10}Be is increased if part of this isotope has decayed, while that for ^{10}Be is somewhat decreased. Finally, the contribution to the total error in the pathlength determination from uncertainties in the cross sections used is observed to be generally less than or about equal to that from the uncertainties in the measured isotopic abundances.

2. <u>Lifetime</u>. In order to estimate the density of matter, n, in the cosmic-ray confinement volume consider equation IV.10 for the specific case of ^{10}Be (denoted by putting i = 10):

$$\bar{J}_{10}(\gamma)\left[\frac{1}{\lambda_e} + \frac{1}{\langle m\rangle\, nc\beta\gamma\tau_d(10\to *)} + \frac{\langle\sigma_{tot}(A_{10}, A_k)\rangle_k}{\langle m\rangle}\right] = \sum_j \frac{\langle\sigma_{10j}^{k}\rangle_k}{\langle m\rangle}\,\bar{J}_j(\gamma) \tag{IV.15}$$

Here we have substituted $\lambda_e = \langle m\rangle\, nc\beta\gamma\tau_e$, taken $\bar{Q}^s_{10}(\gamma) = 0$, and noted explicitly that no other isotopes decay into ^{10}Be. Observing that the right hand side is independent of the survival or decay of ^{10}Be, we may write equation IV.15 again for the case where ^{10}Be does not decay:

$$\bar{J}^{ND}_{10}(\gamma)\left[\frac{1}{\lambda_e} + \frac{\langle\sigma_{tot}(A_{10}, A_k)\rangle_k}{\langle m\rangle}\right] = \sum_j \frac{\langle\sigma_{10j}^{k}\rangle_k}{\langle m\rangle}\,\bar{J}_j(\gamma) \tag{IV.16}$$

TABLE IV.2

Leakage Pathlengths Derived from Various Isotopes
($g\ cm^{-2}$ units)

Isotope	Lower Limit B	Lower Limit A	Best Value	Upper Limit A	Upper Limit B
^{7}Be	3.28	3.49	4.01	4.53	4.88
^{9}Be	2.46	2.58	3.24	4.04	4.27
^{10}Be*	0.89	0.91	1.60	2.40	2.46
^{10}B*	4.09	4.37	5.50	6.48	7.07
^{11}B	4.93	5.54	6.33	6.88	8.02
^{12}C	----	----	----	----	----
^{13}C	4.70	5.10	6.53	7.89	8.87
^{14}N	7.61	8.22	----	----	----
^{15}N	8.12	9.53	----	----	----

A: No Cross Section Errors Included

B: Cross Section Errors Included in Interaction Correction, Atmospheric Correction and Leaky Box Calculation

*^{10}Be assumed Stable

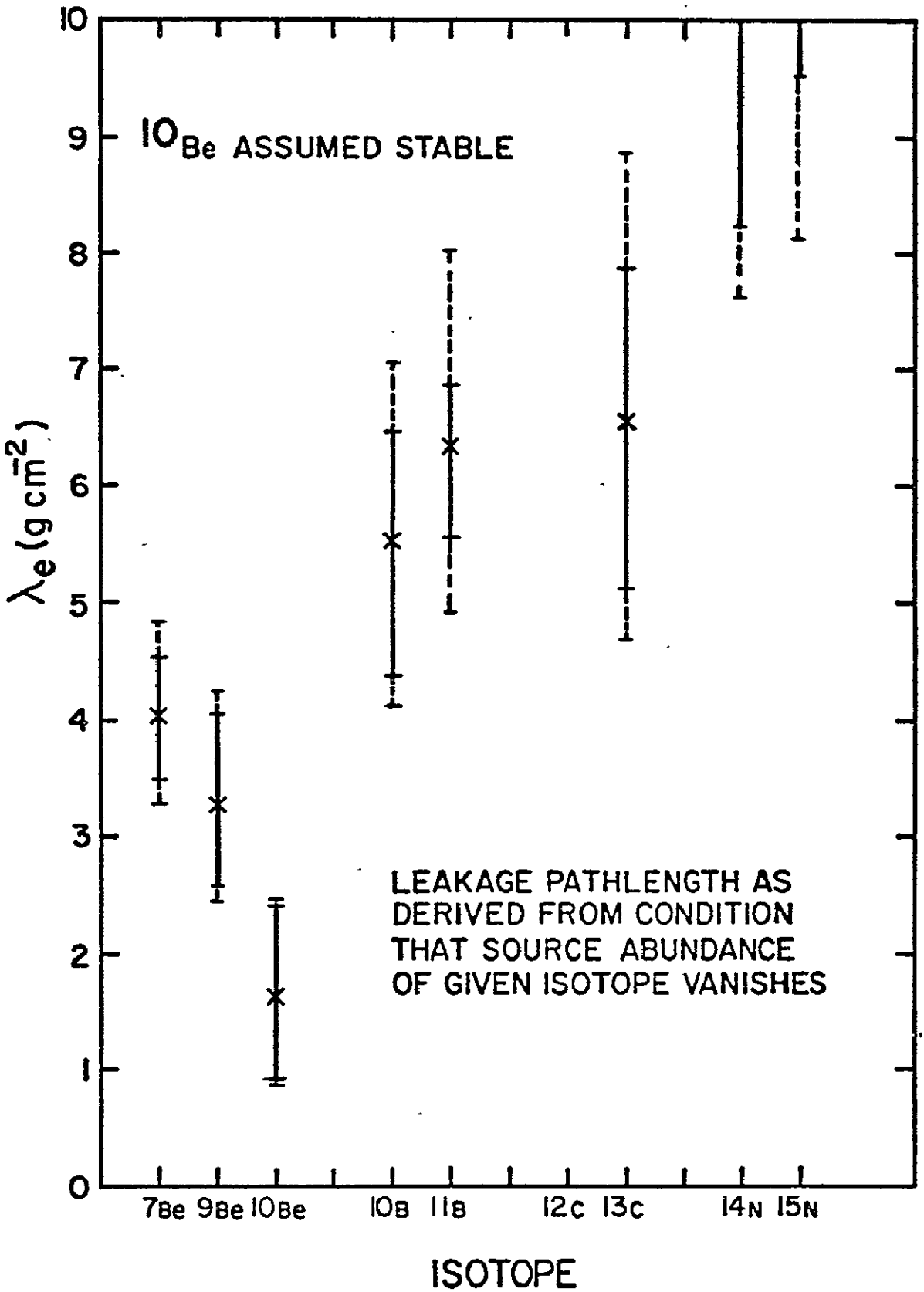

Figure IV.2. Mean leakage pathlength, λ_e, as derived from condition that source abundances of various isotopes vanish. Dashed extensions to error limits include contributions of cross section uncertainties assumed to be 10% for total and 15% for partial cross sections.

We may now eliminate the right hand sides of equations IV.15 and IV.16, and solve for the density, n. The result is

$$n = \left[\langle m\rangle c\beta\gamma\tau_d(10\to *)\right]^{-1}\left[\frac{\bar{J}_{10}^{ND}(\gamma)}{\bar{J}_{10}(\gamma)} - 1\right]^{-1}\left[\frac{1}{\lambda_e} + \frac{\langle\sigma_{tot}(A_{10}, A_k)\rangle_k}{\langle m\rangle}\right]^{-1} \qquad \text{(IV.17)}$$

Assuming the interstellar medium is mainly H, with a 10% admixture of He, we have $\langle m\rangle$ = 1.3 amu. Taking the propagation energy to be E = 600 MeV/nuc, and putting τ_d (10 → *) = 2.2 x 10^6 yr (Yiou et al. 1972), we have

$$\left[\langle m\rangle c\beta\gamma\tau_d(10\to *)\right]^{-1} = 0.17\ g^{-1}cm^{-1} \qquad \text{(IV.18)}$$

Using equation III.42 for the total cross section, we also have

$$\frac{\langle\sigma_{tot}(A_{10}, A_k)\rangle_k}{\langle m\rangle} = 9.3\ g^{-1}cm^2 \qquad \text{(IV.19)}$$

It now remains only to estimate the abundance of ^{10}Be expected if none decays, $\bar{J}_{10}^{ND}$. This can be done by inverting equation IV.11 to calculate the expected observed abundances given an assumed set of source abundances:

$$\bar{J}_i(\gamma) = \sum_j {}^{LB}D_{ij}\,\bar{Q}_j^S(\gamma) \qquad \text{(IV.20)}$$

The source abundances used are, of course, based on the results of the previous calculation, when the leakage pathlength, λ_e, was estimated. This has been done by Tsao et al. (1973) at high energies (E ≳ 2300 MeV/nuc) using the observed charge abundances and assuming the isotopic composition of the various elements in the cosmic rays at their source is the same as that observed for solar system material. In table IV.3 we show the predictions of a similar calculation for the arriving cosmic rays, where we have adopted the source composition of Silberberg and Tsao,

TABLE IV.3: Comparisons With Models++

Model	Observed	Z	Y	X	W	V	U
λ_e (g cm^{-2})		5	6	5	5	5	5
Energy (MeV/nuc)		600	600	1200	600	600	600
Gas Composition (percent He)		10	10	10	0	10	10
Cross Section Modifications+		b	b	b	b	a	c
Abundance Ratios:							
^{7}Be/Be	0.61 ±0.07	0.53 ±0.04	0.53 ±0.04	0.54 ±0.04	0.52 ±0.04	0.58 ±0.05	0.55 ±0.04
^{9}Be/Be	0.28 ±0.05	0.28 ±0.02	0.28 ±0.02	0.26 ±0.02	0.28 ±0.02	0.23 ±0.02	0.28 ±0.02
^{10}Be/Be	0.11 ±0.04**	0.19 ±0.02**	0.19 ±0.02**	0.20 ±0.02**	0.20 ±0.02**	0.19 ±0.02**	0.16 ±0.01**
Be/C	0.069±0.008	0.090	0.103	0.101	0.098	0.085	0.087
^{10}B/B	0.30 ±0.04	0.32 ±0.03	0.32 ±0.03	0.31 ±0.03	0.32 ±0.03	0.30 ±0.03	0.33 ±0.03
^{11}B/B	0.70 ±0.05	0.68 ±0.06	0.68 ±0.06	0.69 ±0.06	0.68 ±0.06	0.70 ±0.06	0.67 ±0.06
B/C	0.251±0.017	0.222	0.248	0.218	0.251	0.222	0.225
^{12}C/C	0.94 ±0.03	0.95 ±0.04	0.94 ±0.04	0.95 ±0.04	0.94 ±0.04	0.95 ±0.04	0.95 ±0.04
^{13}C/C	0.06 ±0.01	0.05 ±0.01	0.06 ±0.01	0.05 ±0.01	0.06 ±0.01	0.05 ±0.01	0.05 ±0.01
C/C	1.000±0.036	1.000	1.000	1.000	1.000	1.000	1.000
^{14}N/N	0.43 ±0.09	0.62 ±0.03	0.61 ±0.03	0.62 ±0.03	0.61 ±0.03	0.61 ±0.03	0.62 ±0.03
^{15}N/N	0.57 ±0.07	0.38 ±0.05	0.39 ±0.05	0.38 ±0.05	0.39 ±0.05	0.39 ±0.05	0.38 ±0.05
N/C	0.271±0.024	0.247	0.260	0.243	0.263	0.243	0.247

* With Corrections ACDF (see table III.3)

** ^{10}Be Stable

\+ Cross Section Modification Schemes:
- a - pure semiempirical formula
- b - semiempirical formula normalized to results of Lindstrom et al. (1975) for C & O primaries (see table III.4)
- c - semiempirical formula normalized to results of Lindstrom et al. (1975) for C & O primaries (see table III.4) and data given by Silberberg et al. (1973) for $^{11}B \rightarrow {}^{10}Be$ (correction factor 0.59), $^{11}B \rightarrow {}^{10}B$ (2.33), and $^{56}Fe \rightarrow {}^{11}B$ (0.69)

++ Error limits on model calculations estimated assuming 10% uncertainties on all total cross sections and 15% uncertainty on partial cross sections

ORIGINAL PAGE IS OF POOR QUALITY

and performed the same calculation at a lower energy (E = 600 MeV/nuc) which is more appropriate to the present application. Table IV.3 shows the effects of varying various parameters involved in this calculation. The specific examples include a leakage pathlength $\lambda_e = 6$ g cm^{-2} (rather than 5 g cm^{-2}), an interstellar medium consisting of pure H (without the 10% He admixture), a propagation energy E = 1200 MeV/nuc (rather than 600 MeV/nuc), and the correction of the partial cross sections used for discrepancies with the experimental values tabulated by Silberberg and Tsao (1973) in cases not covered by the data of Lindstrom et al. (1975a). From the talbe, it is clear that the relative abundances predicted for the Be isotopes are quite insensitive to the above variations. By comparing the predicted and observed abundances of ^{10}Be, we estimate that (55 $\pm$ 21)% of the ^{10}Be survives in the cosmic rays. Although the error here is estimated solely from the statistical errors on the observed ^{10}Be abundance as assigned by the maximum likelihood fit, it would not be significantly increased if cross section uncertainties were included. One thus has

$$\left[\frac{\bar{J}_{10}^{ND}(\gamma)}{\bar{J}_{10}(\gamma)} - 1 \right]^{-1} = 1.2 \begin{smallmatrix} +2.0 \\ -0.7 \end{smallmatrix} \tag{IV.21}$$

If the leakage pathlength is $\lambda_e = 5$ g cm^{-2}, we now have from equation IV.17

$$n = \left(0.7 \begin{smallmatrix} +1.0 \\ -0.4 \end{smallmatrix}\right) \text{cm}^{-3} \tag{IV.22}$$

and, consequently,

$$\tau_e = \left(5 \begin{smallmatrix} +6 \\ -3 \end{smallmatrix}\right) \times 10^6 \text{ yr} \tag{IV.23}$$

Since the leakage pathlength is a rather uncertain parameter (even within the present data, as may be seen from figures IV.1 and IV.2), the explicit dependences of n and τ_e on λ_e are shown in figures IV.3 and IV.4, respectively. As can be seen from these figures, the above conclusions are not substantially altered by reasonable fluctuations in the leakage pathlength, λ_e.

C. Conclusions

The results given by equations IV.22 and IV.23 lie between the extremes of the disk and halo models, as discussed in section A. This is to be expected. However, the result is substantially more consistent with the disk model than the halo. In fact, if there is a halo at all, the present result seems to indicate that it should be substantially flattened.

This interpretation of the experimental data is obviously model dependent. In particular, in writing equation IV.10 it has been assumed that the gas densities encountered by the cosmic rays along their trajectories through interstellar space is everywhere constant. If this is not the case, then the density of interstellar gas, n, should be replaced in the model by

$$\bar{n} = \frac{1}{\bar{J}_i(\gamma)} \frac{1}{V} \oint dV\, n\, J_i(\gamma) = \frac{\overline{n J_i(\gamma)}}{\bar{J}_i(\gamma)} \qquad \text{(IV.24)}$$

Thus the density given by equation IV.22 is not a simple average of the gas density over the confinement volume, but rather a weighted average with the cosmic-ray intensity as the weighting function. This weighted average reduces to a simple average in cases where there is no correlation between cosmic-ray intensity and gas density.

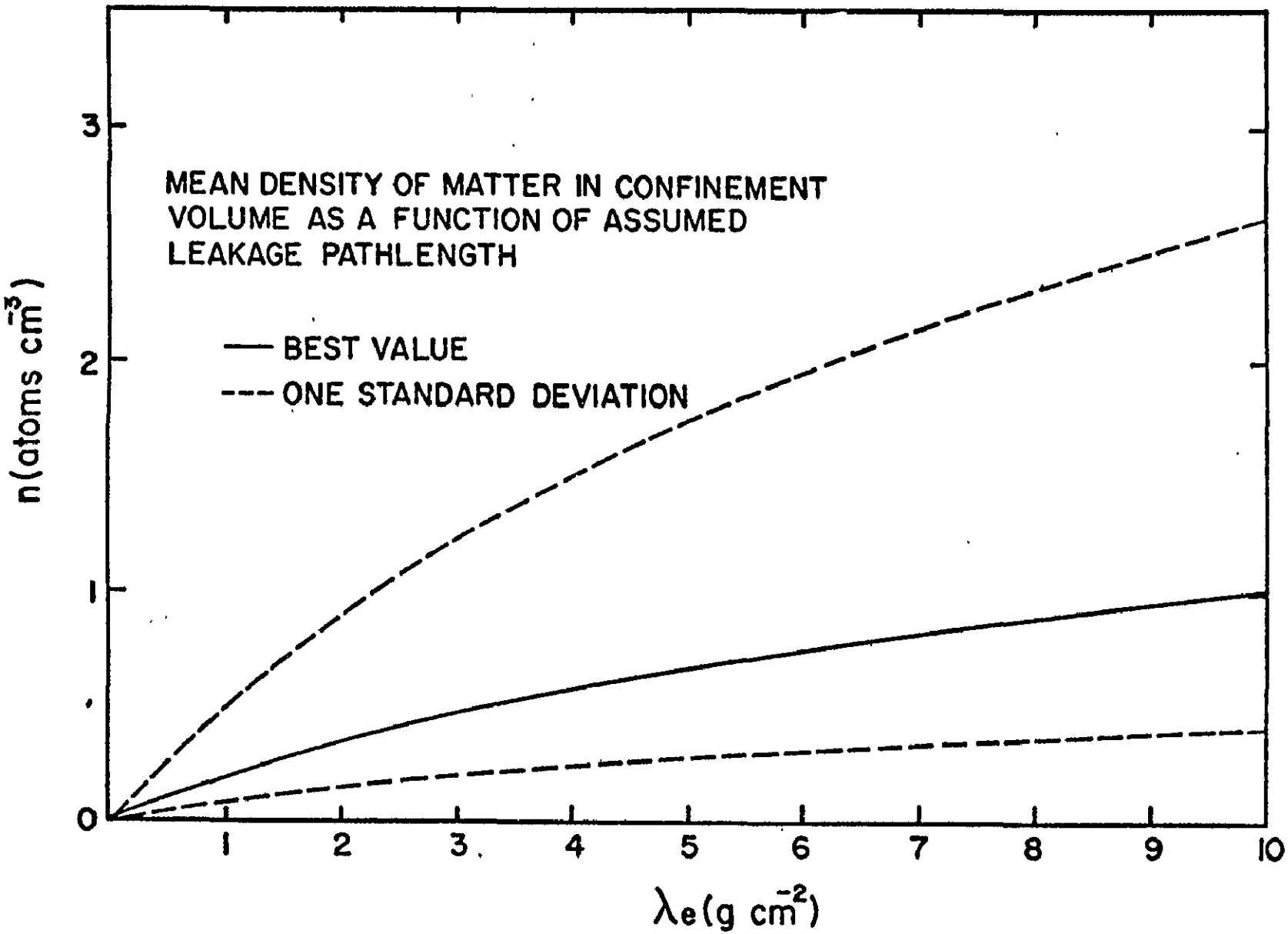

Figure IV.3. Matter density in cosmic-ray confinement volume as a function of mean escape pathlength.

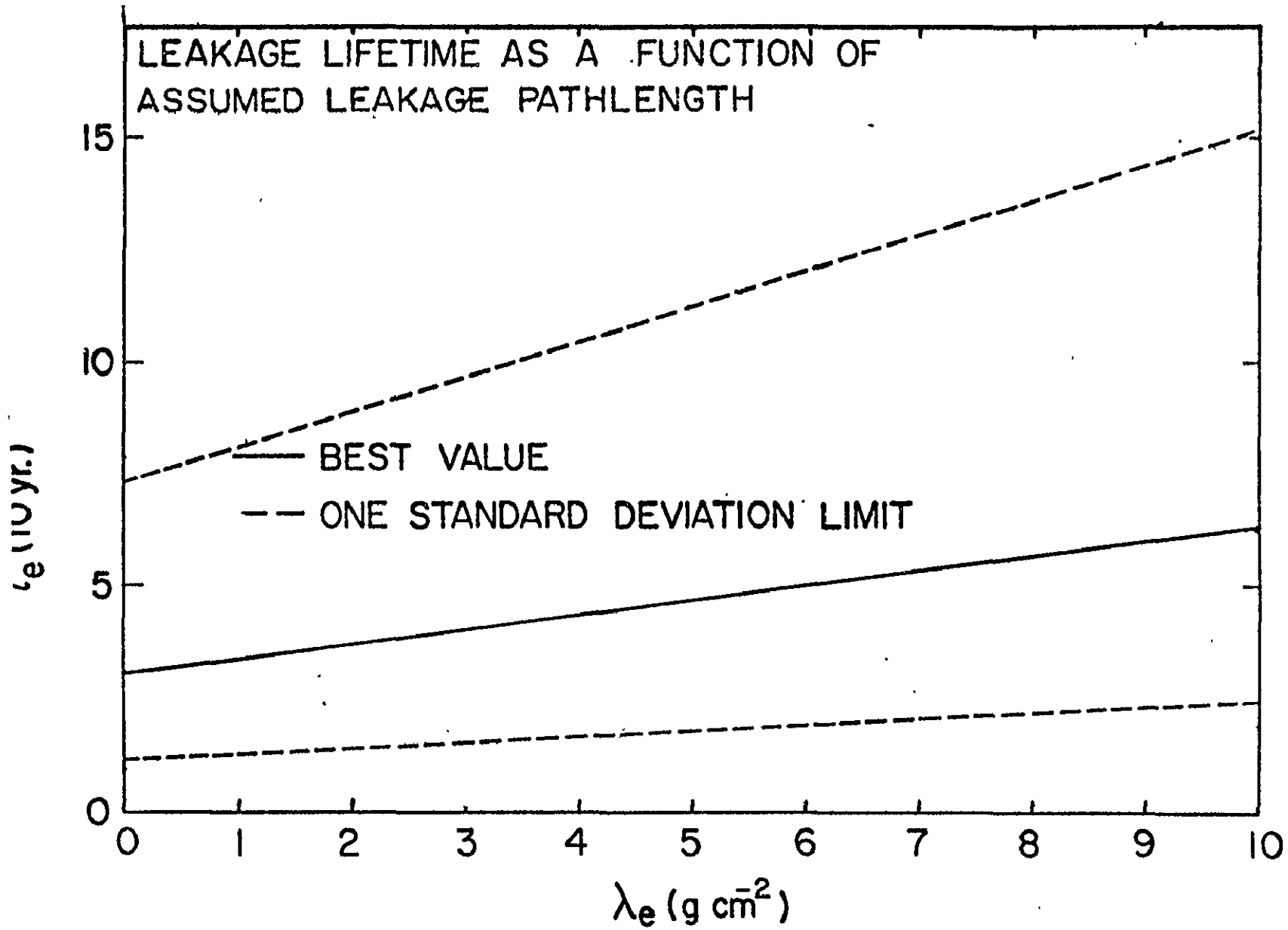

Figure IV.4. Mean lifetime against escape for cosmic rays as a function of mean pathlength for escape.

Models which have been constructed to explain the gamma-ray emission of the galactic disk generally require a positive correlation between cosmic-ray intensity and gas density. Such a correlation would tend to make $\bar{n}$ somewhat larger than a simple average over the confinement volume of the gas density. Consider for example the model of Bignami et al. (1975), in which the cosmic-ray intensity is taken to be proportional to the gas density. In this model, the confinement volume is taken as the galactic disk, which is considered approximately equally divided between spiral arms and interarm regions. The gas densities in the spiral arms are taken as roughly a factor of two greater than those characteristic of the interarm regions. We then estimate that the weighted average gas density, $\bar{n}$, is only a factor of $\frac{10}{9}$ greater than the simple average of the gas density over the galactic disk. Thus it seems probable that $\bar{n}$ does not deviate significantly (at the current level of resolution) from a simple average of the gas density.

If the relative composition of the cosmic rays (as opposed to intensity) is correlated with gas density, then the weighted average gas density, $\bar{n}$, should also depend upon the cosmic-ray species from which it is determined. This dependence would also be reflected in the pathlength $\lambda_e = \langle m \rangle \bar{n} \beta c \tau_e$. Such variations in $\bar{n}$, however, should be no more than those estimated above for intensity variations, and thus are almost certainly negligible for purposes of interpreting the present data.

In general, the cosmic-ray source function used in the leaky box model, $\overline{Q_i^s}(\gamma)$, represents an average over space and time of the true source function, $Q_i^s(\gamma,\vec{r},t)$. Thus the true source function, which is almost certainly a highly discrete function of space and time, is replaced in the leaky box model by a constant in space and time. As we have already

noted, this is generally a good approximation as long as none of the discrete sources are too close to the observer in space and/or in time. However, if a significant part of the pathlength, λ_e, is traversed in a high density region near the source (e.g. a supernova envelope), we would expect to observe a smaller surviving fraction of ^{10}Be than if the density were constant everywhere along the typical cosmic-ray trajectory. Thus both the mean escape time, τ_e, and the gas density in the corresponding confinement volume, n, would tend to be overestimated under such conditions.

If the cosmic-ray electron component is assumed to be produced by the same sources and to be confined to the same "leaky box" as the nuclear component, then the mean escape time, τ_e, should be reflected in a break observed in the electron energy spectrum. So far, no such break has been seen in observations extending from roughly 10 GeV (below which the spectrum is significantly affected by solar modulation) to about 1000 GeV. The interpretation of this observation is substantially clouded by the differences among the results reported by the various experimenters, which are significantly outside of the quoted experimental errors. Observations of the electron energy spectrum have been reported described as power laws with spectral indices ranging all the way from ~ 2.7 (which would be consistent with the nuclear component) to ~ 3.4. Until the experimental situation is improved, it is not clear that observations of the electron spectrum can be used to place significant constraints on the mean confinement time of cosmic rays, τ_e. Furthermore, such a result requires additional assumptions before it can be related to the parameter, τ_e, which has been estimated in the present thesis. In particular, one generally assumes that the sources, confinement volume and mean escape

time of the electron component are identical to those of the nuclear component, none of which is established. For further details on this problem, see Meegan et al. (1975) and references therein.

Let us now consider the resolution of the present experiment, and how it might be improved. The most obvious possibility would be to perform the same experiment at the top of the atmosphere. This would improve the uncertainty on the ^{10}Be abundance at the top of the atmosphere from 40% to ~ 25%. The improvement would not be as marked for other isotopes, however, since the fraction of the observed abundances of these isotopes originating in atmospheric interactions of heavier species is generally much smaller than for ^{10}Be. One might also hope to benefit from improved statistics due to the increased exposure time of an experiment done at the top of the atmosphere (i.e. a satellite experiment).

The alternatives discussed above decrease the mathematical uncertainty in the result without a corresponding increase in the mass resolution of the experiment. Thus the credibility of the result may not in fact be significantly improved. The most important possibility for improving the actual mass resolution of the experiment would be an improved calibration of the various detectors. Such a calibration would most probably be performed at an accelerator and include the internormalization of the detector responses, a detailed investigation of the

shapes of the response functions of the various detectors for various particles of various incident velocities, and the mapping of positional variations in detector response. A knowledge of the shape of the response function is particularly important if we are to improve the credibility of the present result; specifically, the question of a possible asymmetry in the mass distributions for Be isotopes urgently requires resolution. The mass resolution may also be improved by as much as a factor of two by going to completely unsaturating scintillators (if such can be found). This would also help to improve the situation with respect to the internormalization of the detectors, since the response functions of such scintillators would be expected to be more nearly uniform. We see from the above discussion that there is a large potential for achieving improved mass resolution from experiments of this type. Furthermore, only a small part of this potential need actually be achieved before a valley begins to separate the ^{9}Be and ^{10}Be distributions, as discussed in Chapter II. Such a situation would, of course, markedly improve the credibility of the present results.

Ideally, future experiments should be done at higher energies in order to minimize the importance of corrections for solar modulation. Energies $\geqslant$ 1 GeV/nuc would be most advantageous if achievable. One possibility for an isotope experiment operating at such energies would be to measure the parameters rigidity, Cerenkov radiation and $\frac{dE}{dx}$, as was suggested in Chapter II. This has the advantage of not requiring that all a particle's energy be absorbed before the measurement can be carried out. The correction for interactions in the detector is accordingly less severe. On the other hand, experiments where the particle must be stopped in the experiment suffer increasing losses to interactions

in the detector as particle energies increase, and their statistical weight is accordingly reduced. In addition, all classes of experiment must contend with energy spectra which are rapidly falling with increasing energy. Thus, experiments to directly measure the abundances of rare isotopes such as ^{10}Be in the cosmic rays at high energies ($E \gtrsim$ 1 GeV/nuc) may not be practical without long exposure times such as might be obtained in satellite experiments, for example.

APPENDIX A

DETECTOR CALIBRATION

This appendix deals with the detailed calibration of the instrumental response using in flight data. In order to do this, it is required to determine the gain and zero offset (a_{ij} and b_{ij}) associated with each gain range of each pulse height analyzer (i.e. see equation III.8), and the correction function (M_i) for positional and temporal variations in detector response.

1. Gain Change Factors. The output of the pulse height analyzers is an integer pulse height together with a two bit code to indicate the appropriate gain range. The use of automatic gain switching was required in order to obtain a dynamic range of 10^5. This necessitated the reconversion of the resulting pulse heights to a linear scale before the reduction of the data could proceed further. Assuming the pulse height analyzers and amplifiers are linear in all gain ranges, we recall equation III.8:

$$H_i = a_{ij}\left(H'_{ij} + b_{ij}\right) \tag{A.1}$$

Here H_i is the final, linearized pulse height characterizing the response of detector i, and is the same quantity as defined by equation III.2. H'_{ij} denotes the unnormalized pulse height from the jth gain range of detector i, while a_{ij} and b_{ij} refer to the gain and zero offset required to normalize it, respectively. The usual procedure would be to put the $b_{ij} = 0$, then observe that at a gain change boundary the same pulse height is measured twice, once in each of two different gain ranges:

$$a_{ij} H'_{ij} = a_{i(j+1)} H'_{i(j+1)} \tag{A.2}$$

TABLE A.1: Gain Change Factors

	a_{ij}							b_{ij}						
DETECTOR	1	2	3	4	5	6	7	1	2	3	4	5	6	7
D1	0.142	3.96	4.14	4.00	----	----	----	2.99	0	0	0	----	----	----
D2	0.179	8.58	----	----	----	----	----	0	0	----	----	----	----	----
D3	0.142	0.389	3.13	23.4	0.188	0.755	3.02	3.30	-3.86	1.61	3.03	-32.82	-4.20	
D4	0.394	2.55	2.40	2.52	2.16	2.50	----	8.48	2.14	-1.99	1.07	1.89	-0.76	----
D5	0.420	2.24	2.72	2.22	2.39	2.25	----	10.05	1.89	-1.67	0.64	1.89	-0.84	----
D6	0.367	2.34	2.56	2.28	2.25	2.25	----	8.31	4.63	-1.75	1.47	1.78	-0.79	----
D7	0.0923	2.37	2.44	2.42	2.09	2.35	----	16.14	1.26	0.27	2.81	2.89	-1.23	----
D8	0.0983	2.30	2.63	2.28	2.23	2.31	----	19.13	1.84	-1.15	0.67	3.37	-1.46	----
D9	0.1117	2.45	2.43	2.39	2.05	2.11	----	3.48	3.68	0.23	0.13	5.12	-2.43	----
D10	0.1040	2.28	2.68	2.20	2.34	2.16	----	13.27	1.65	-1.23	0.56	2.85	-1.32	----
D11	0.1037	2.30	2.53	2.47	2.09	2.38	----	10.13	0.17	1.28	-1.36	2.57	-1.08	----
D12	0.1070	2.34	2.67	2.21	2.30	2.09	----	17.66	2.86	-2.00	1.02	2.66	-1.27	----
D13	0.0986	2.48	2.42	2.52	1.86	2.60	----	7.30	2.06	-0.79	0.54	5.00	-1.92	----
D14	0.0942	2.18	2.89	2.04	2.58	1.99	----	6.40	2.16	-0.86	0.65	2.42	-1.22	----

ORIGINAL PAGE IS
OF POOR QUALITY

$$\underline{a}_{ij} = a_{ij} / a_{i(j-1)}, \qquad \text{for } j > 1 \tag{A.3}$$

In the above, we note that gain ranges are numbered with decreasing gain. The a_{ij} for detector i are thus all determined in terms of a_{i1}, which is recognized as the normalization constant for detector i, and will be determined elsewhere. This is the procedure actually used for detectors D1, D2 and for the highest gain change of D3 (where the 256 channel analyzer has saturated, and no longer overlaps the 1024 channel analyzer). For the 1024 analyzers, the a_{ij} are thus determined to a maximum precision of about 0.5%. If the zero offsets, b_{ij}, are of the order of 5 channels, then additional errors of the order of ~ 2% could be introduced at each gain change. The a_{ij} resulting from the analysis just described, as applied to detectors D1, D2, and the last gain change of detector D3 are tabulated in table A.1.

A substantial innovation included in the current experiment was the use of dual pulse height analyzers with staggered gain ranges on detectors D4-14 and, to some extent, on D3. This offered the advantage of being able to determine both the a_{ij} and the b_{ij} much more accurately, in general, than would be possible using the method just described. In addition, this made it possible to detect and correct for noise, bit errors and other problems related to the amplifiers and pulse height analyzers at a very early stage of the data reduction. If we again order the gain ranges (from either pulse height analyzer) with j increasing as gain decreases we have, from equation (A.1),

$$H'_{ij} = \left[H'_{i(j+1)} + b_{i(j+1)} - \frac{b_{ij}\, a_{ij}}{a_{i(j+1)}} \right] \frac{a_{i(j+1)}}{a_{ij}} \tag{A.4}$$

$$H'_{ij} = \underline{a}_{i(j+1)}\left[H'_{i(j+1)} + \underline{b}_{i(j+1)}\right] \tag{A.5}$$

for the region where the gain ranges j and j+1 overlap. Thus the gains, a_{ij}, and zero intercepts, b_{ij}, can all be determined in terms of a_{i1} and b_{i1}, which are recognized as the absolute normalization and zero intercept parameters for detector i (as a whole), and will be determined later. Figure A.1 shows a representative plot of the type just described, in this case for H'_{71} and H'_{72}. In most cases, we feel the relative gain factors, $\underline{a}_{ij}$, have been determined to within ~ 0.1%, while the zero offsets, $\underline{b}_{ij}$, have been determined to within ~ 0.2 channels by this approach. The detectors D8 and D9 show the presence of substantial amounts of noise, probably originating in the spark chamber, and are accordingly not as well calibrated. Figure A.2 shows H'_{92} versus H'_{93}, which is by far the worst case. In addition to noise, diagrams such as figure A.1 are sensitive to bit errors, which appear as points well off of the calibration line. Nonlinearities in the amplifiers can also be detected and corrected. Finally, the use of an additional pulse height analyzer for each detector increased the resolution immediately after a gain change by a factor of about 2.3 over the case where only one pulse height analyzer is used for each detector. This follows since the resolution is determined by the largest of the two pulse heights which (after the first gain change) is never less than about 90; for the same signal, the smaller pulse height (i.e. the one which has just gain changed) is about 40.

The pulse heights from the two pulse height analyzers for detector i, H'_{ij} and $H'_{i(j+1)}$ were combined to obtain a single value, H_i, according to the relation

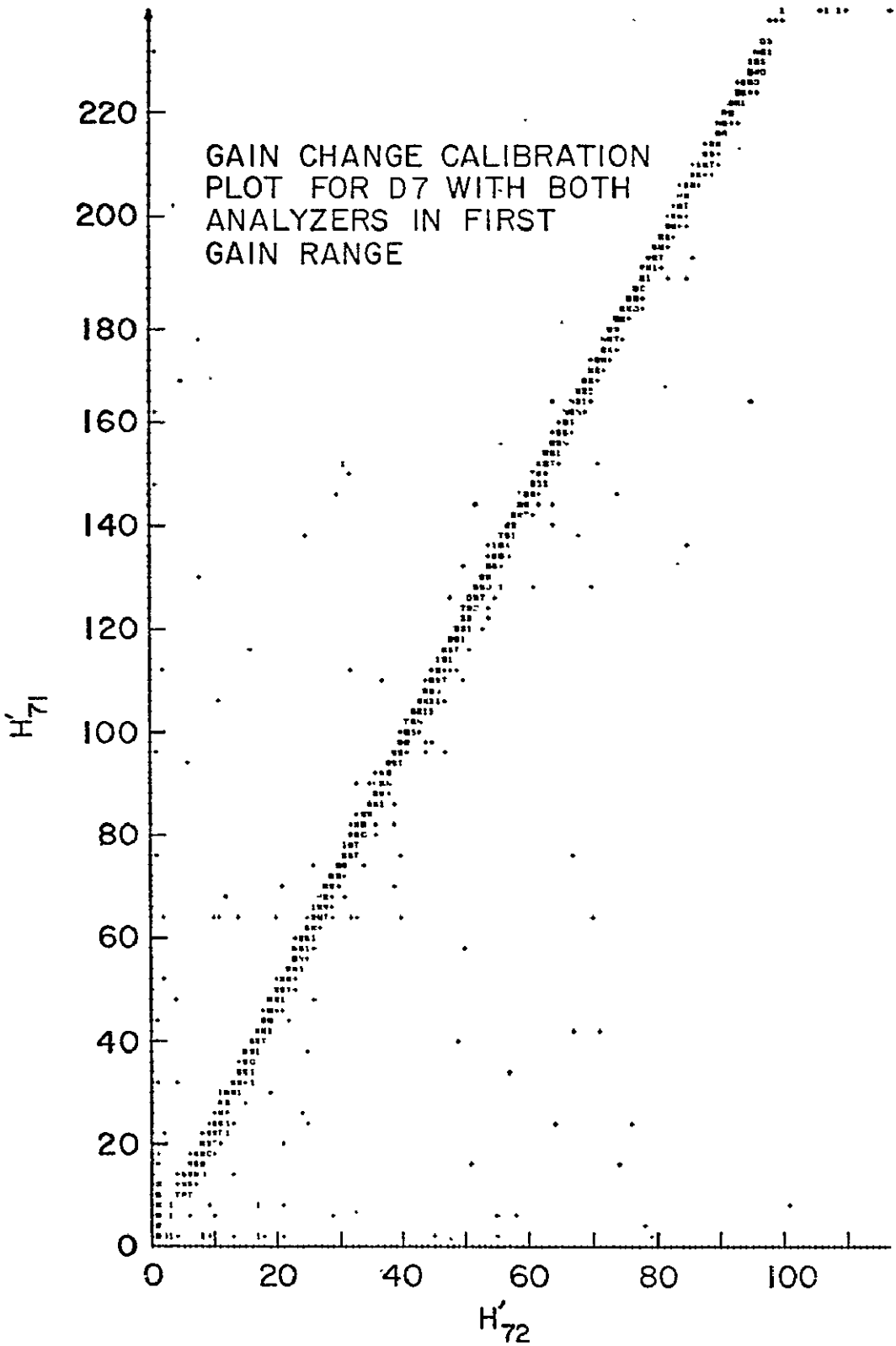

Figure A.1. Typical gain change calibration plot: H'_{71} versus H'_{72}.

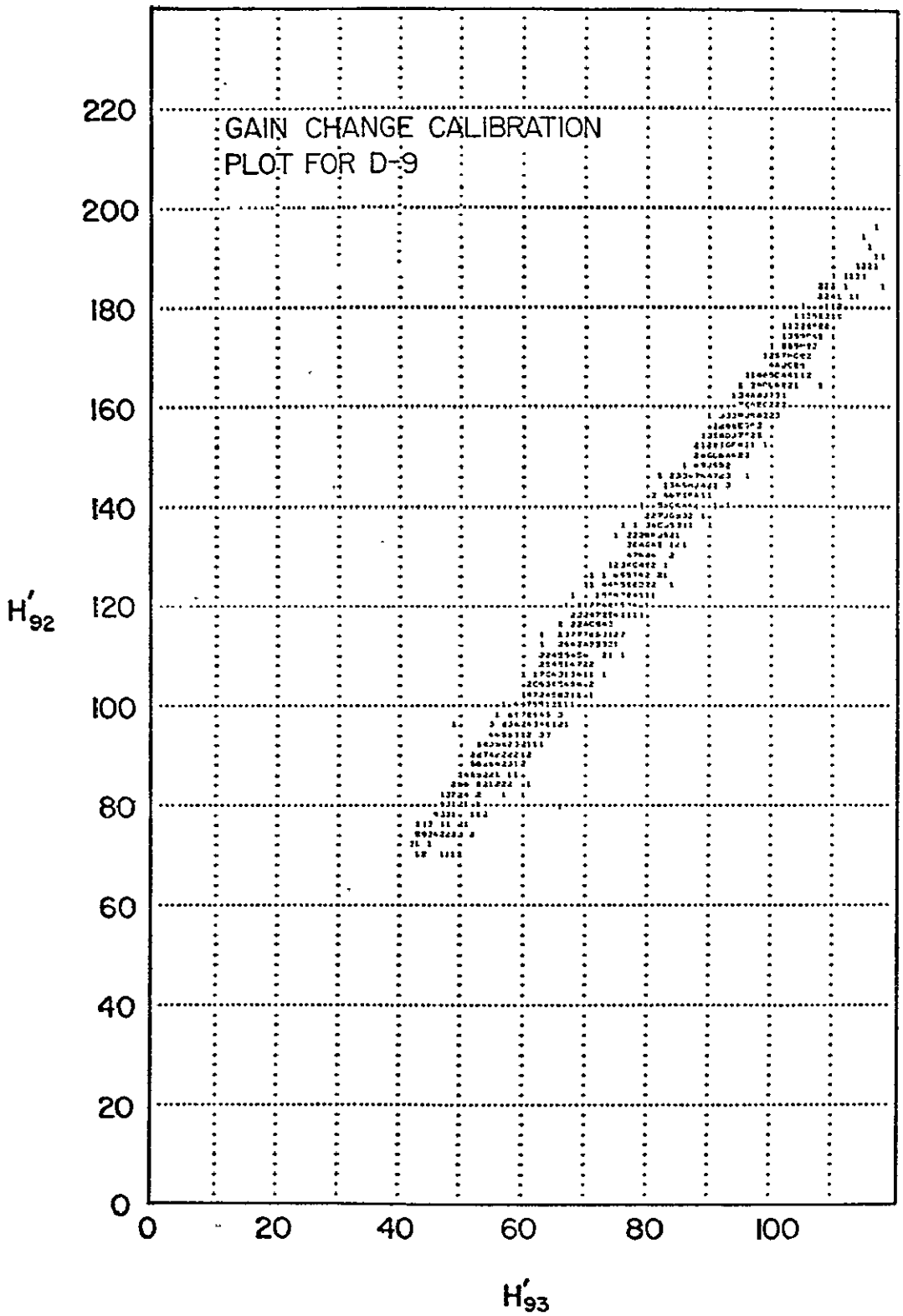

Figure A.2. Noisy gain change calibration plot: H'_{92} versus H'_{93}.

$$H_i = \frac{a_{ij}^2 a_{i(j+1)} \left[H'_{i(j+1)} + b_{i(j+1)}\right] + a_{i(j+1)}^2 a_{ij} \left(H'_{ij} + b_{ij}\right)}{a_{ij}^2 + a_{i(j+1)}^2} \tag{A.6}$$

Here it is assumed the resolutions of the pulse height analyzers (in channels) are given by

$$\sigma_{H'_{ij}} = \sigma_{H'} = constant \tag{A.7}$$

so that we have

$$\sigma_{H_{ij}} = a_{ij} \sigma_{H'} \tag{A.8}$$

from equation A.1. This is equivalent to taking the normal from the experimental point (H'_{ij}, $H'_{i(j+1)}$) to the appropriate calibration line. The resolution of H_i is given by

$$\sigma_{H_i} = \sigma_{H'} \left[a_{ij}^{-2} + a_{i(j+1)}^{-2}\right]^{-\frac{1}{2}} \cong 0.92\, a_{i(j+1)} \sigma_{H'} \tag{A.9}$$

where $a_{i(j+1)} \cong 2.4$ has been assumed. Putting $\sigma_{H'} \leqslant 0.5$ channels, we have

$$\sigma_{H_i} \lesssim 0.46\, a_{ij_{max}} \tag{A.10}$$

where j_{max} is the gain range giving the largest pulse height, H'_{ij}, corresponding to H_i.

Events which lie clearly off the calibration are tagged and, usually, thrown out in the analysis. This is intended mainly to remove events with bit errors. The resolution for doing this is generally a factor of about 2.4 worse for the larger of the two pulse heights, because of the slope of the calibration line.

For detector D3, all but the last gain change of the 1024 channel

analyzer were calibrated in the fashion just described. Since the last gain range of the 256 channel analyzer had saturated before the last gain change of the 1024 channel analyzer was reached, this last gain change factor was determined by the same procedure as for D1 and D2. The values of $\underline{a}_{ij}$ and $\underline{b}_{ij}$ obtained by the above procedure for detectors D3-14 are tabulated in table A.1.

2. Detector Nonlinearities. The amplifiers used (especially with the 256 channel analyzers) were known exhibit some nonlinearities. A pulser calibration of a representative amplifier - pulse height analyzer combination is shown in figure A.3. It is apparent from the figure that, above channel 32 the response is nearly linear with the nonlinearity being manifested mainly in a large zero offset. For this reason, the calibration lines (e.g. figure A.1) were fitted neglecting data below channel 32 in either pulse height analyzer. The nonlinearities have otherwise been neglected. This can only significantly effect the analysis for extremely low pulse heights in the first gain range (i.e. $\leqslant$ 15 x minimum for D4-6 and $\leqslant$ 5 x minimum for D7-14).

3. Detector Normalization. Originally it had been intended to use highly relativistic carbon and oxygen triggering the experiment in the penetrating mode to determine the detector normalization factors, a_{i1}, and to provide a first order estimate of the zero offsets, b_{i1}. This could be done for example by selecting $b_{11} = 0$, then making a plot of the relativistic peaks (times minimum units) of various elements in D1 against their expected (after normalization) values for an ideal, non-saturating scintillator. Because of scintillator saturation (non-linearity) effects which increase with increasing charge, the result would be a curve asymptotic to a straight line through zero in the limit $Z \rightarrow 0$.

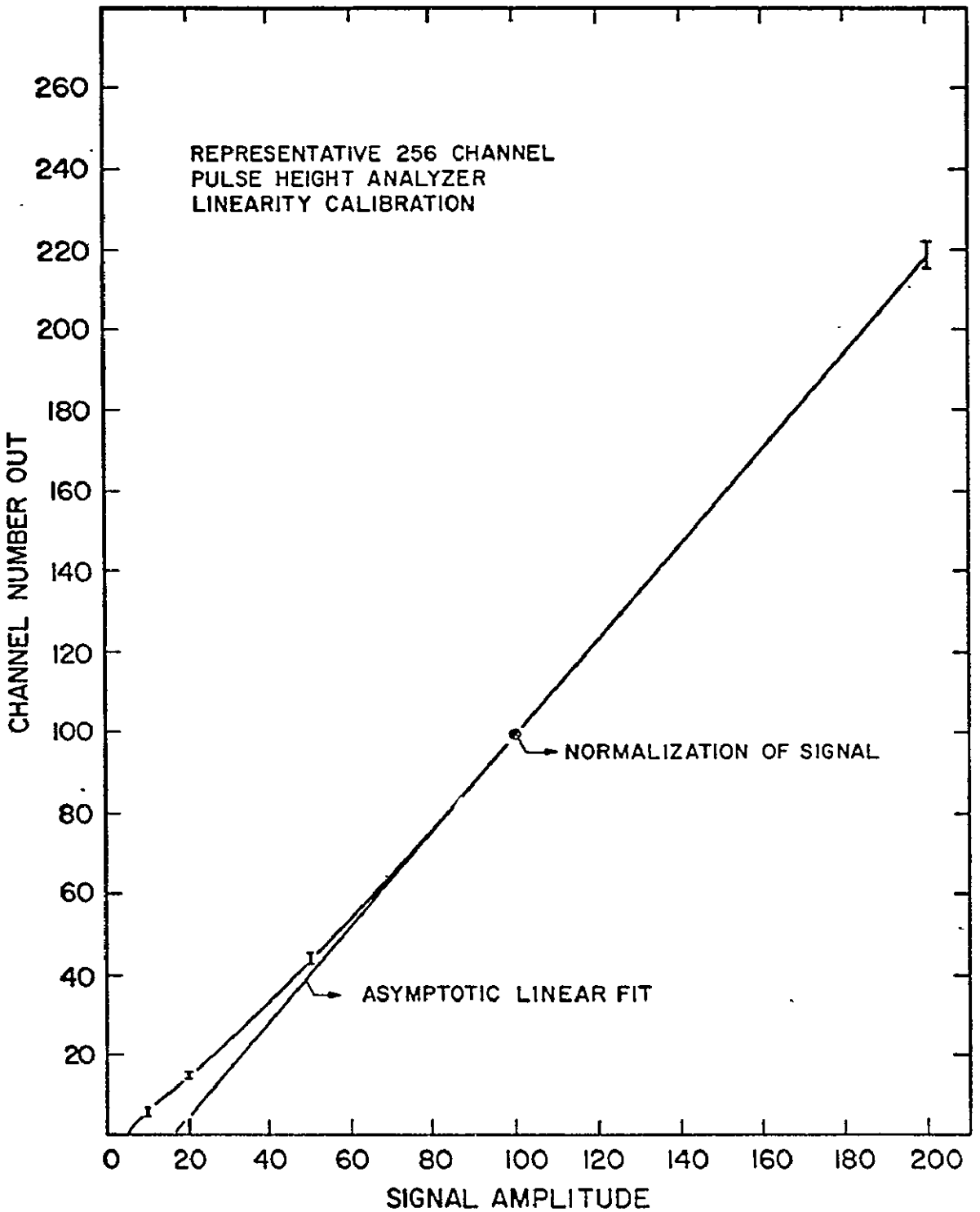

Figure A.3. Representative calibration of nonlinearity of a 256 channel analyzer with a pulser.

The slope of this line would then be identified with the parameter a_{11}. The remainder of the scintillation detectors, D3-14, would then be easily normalized by adjusting the a_{ij} and b_{ij} so that both relativistic carbon and oxygen fall in the same channel as for D1. The Cerenkov detector was indeed finally normalized on this basis (i.e. by setting relativistic carbon equal to 36 x minimum and choosing $b_{21} = 0$); however, it was found that the above procedure could not be directly applied to the normalization of the scintillation detectors.

When the various scintillation detector pulse heights (unnormalized) were plotted against the Cerenkov, it was noticed that the scintillator response to the most highly relativistic particles increased as one went deeper into the stack. This was attributed to very high energy delta rays which penetrated several detectors. Thus it was decided to use for the normalizations semi-relativistic particles whose velocities were not sufficient to give rise to such high energy delta rays. In order to use these particles, however, one must correct for the slowing down of the particles as they penetrate into the stack. This was done by first determining a particle's range from the top of the Cerenkov detector, R_2, from equation III.6:

$$C_2' = \frac{H_2(\beta)}{H_2(\beta\to 1)} = \frac{1}{Z^2 T_2 \sec\theta}\int_{R_2 - T_2\sec\theta}^{R_2} C\, dR'$$

$$\cong \frac{C}{Z^2} = \left(\frac{1}{n^2-1}\right)\left(n^2 - \frac{1}{\beta^2}\right) \qquad \text{(A.11)}$$

Here the range-energy tables (Barkas and Berger, 1964) are used to relate the range to the velocity, together with the assumption that mass and charge are related according to A = 2Z (this is excellent for C, O, Mg and Si; in any case, the corrections are small enough that the

departures from this relation enter as second order terms, and may be neglected). The approximation in equation A.11 is that the particle does not slow down significantly in traversing the Cerenkov radiator, D2; this is not required for the analysis. The parameter C_2' is unity for highly relativistic particles, and zero for particles which emit no Cerenkov light. If the rate of radiation of Cerenkov light changes significantly over the Cerenkov detector, the solution of A.11 is by an iterative procedure.

The quantity

$$C_i' = \frac{1}{Z^2 T_i \sec\theta} \int_{R_i - T_i \sec\theta}^{R_i} C \, dR' \tag{A.12}$$

is now evaluated for each detector, i. The particles are selected for the analysis according to $0.1 \leq C_i' \leq 0.8$, which is essentially the restriction to semi-relativistic particles mentioned above. It is then noted that a plot of C_2' against $1/2\ (H_1 + H_3)$ shows a very nearly linear behavior (for a given charge) in this region, as is shown in figure A.4:

$$C_2' = \frac{\nu}{2}(H_1 + H_3) + \eta \tag{A.13}$$

It is assumed that H_i and C_i' should be related by exactly the same coefficients (ν and η) if the detectors are all properly normalized, i.e.

$$C_i' = \nu H_i + \eta = \nu a_{i1}(H_{i2}' + b_{i1}) + \eta \tag{A.14}$$

Using equation A.14, the a_{i1} and b_{i1} for all scintillation detectors may be related to those of one standard detector by plotting

$$H_i^{cal} = \frac{1}{\nu}(C_i' - \eta) \tag{A.15}$$

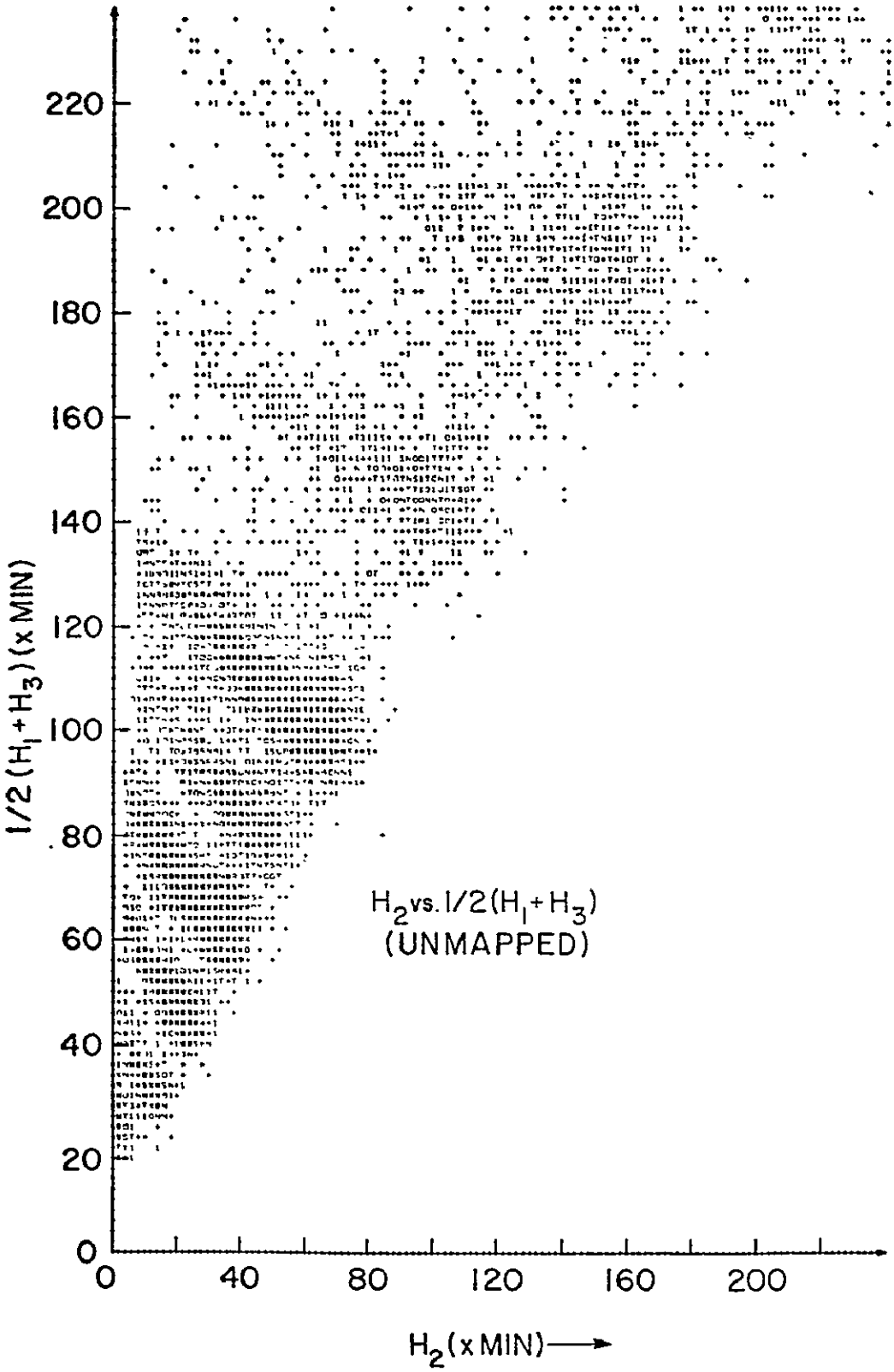

Figure A.4. Unmapped Cerenkov versus scintillator plot. Pulse heights are in times minimum units such that a particle of velocity $\beta=1$ and charge $Z=1$ gives a pulse height of 1, regardless of detector thickness or angle of incidence.

against H'_{i2}. The standard detector gives the optimal values for the parameters ν and η. As the analysis is described above, this role would be played by the combination of D1 and D3 (see equation A.13). However, because of the unique response functions characterizing these two detectors, it was preferred to use D4 as the standard detector. The normalization constant a_{41} was determined from the relation (see equation III.3).

$$\frac{dL}{dE}(\beta \to 1) = \left\langle \frac{H_i \cos\theta}{T_i \frac{dE}{dX}} \right\rangle_{\perp \vec{r}_4, \theta, \phi, t, C_2' \geq 0.8} \tag{A.16}$$

where the average is over all data with $C_2' \geq 0.8$ and

$$1 = \langle M_i \rangle_{\perp \vec{r}_4, \theta, \phi, t, C_2' \geq 0.8} \tag{A.17}$$

has been assumed for the normalization of the mapping function, M_i. The normalization is then obtained from the condition

$$\lim_{Z \to 0} \frac{dL}{dE}(\beta \to 1) = 1 \tag{A.18}$$

so that

$$\frac{1}{a_{41}} = \lim_{Z \to 0} \left\langle \frac{H_i \cos\theta}{T_i \frac{dE}{dX}} \right\rangle_{\perp \vec{r}_4, \theta, \phi, t, C_2' \geq 0.8} \tag{A.19}$$

if we choose $b_{41} = 0$. This is shown in figure A.5. As is evident from the figure, the missing data from the light ($1 \leq Z \leq 3$) nuclei (which should have been admitted in the calibration mode) would have been very useful for this purpose.

Because of scintillar non-linearities which varied from detector to detector, it was found that the interdetector normalization plots

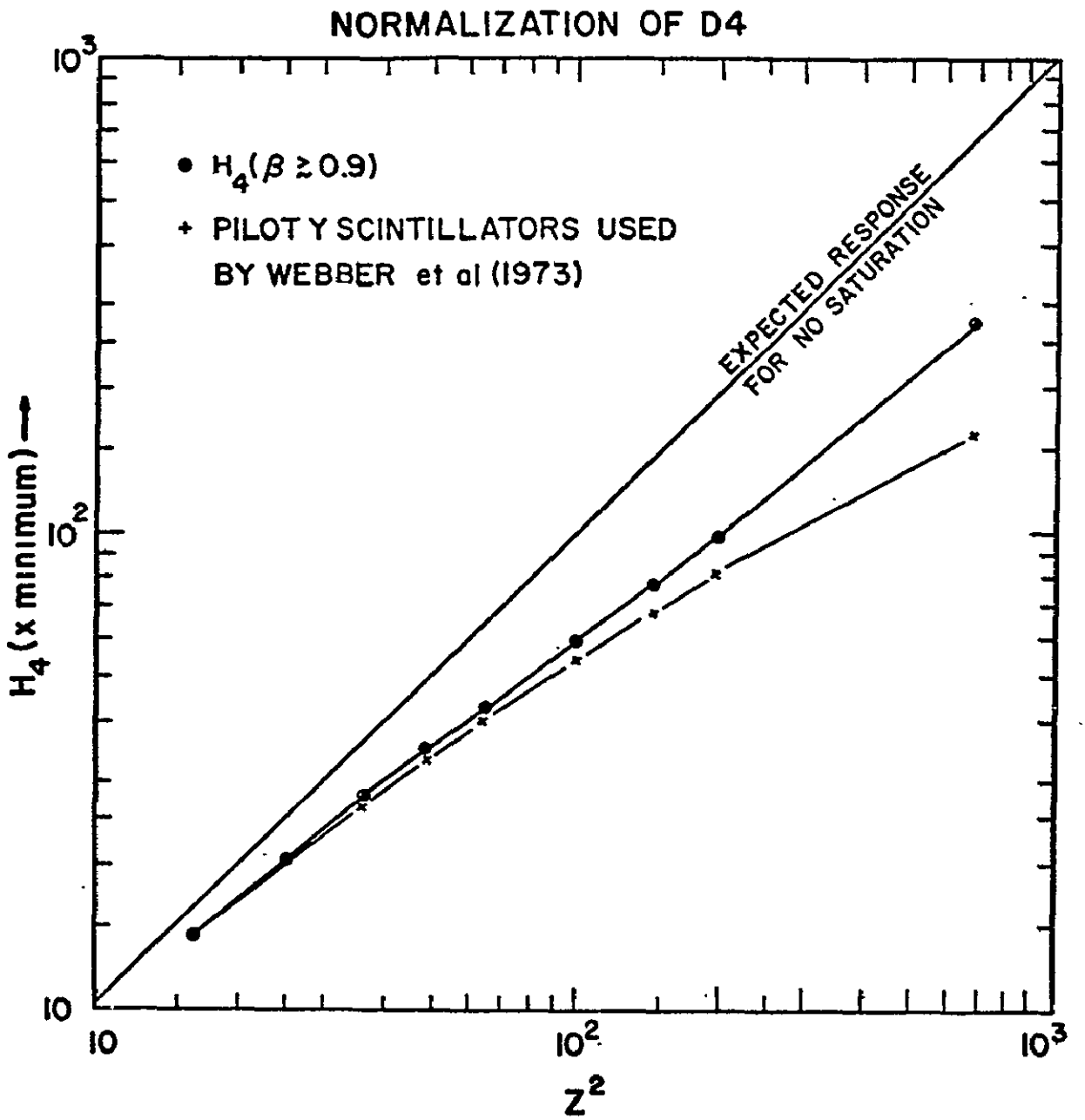

Figure A.5. Absolute calibration of D4. See fig. A.4 for definition of x minimum units.

just described did not always display linear correlations over the entire range of charges. In fact, the deviations from linearity became marked for highly charged particles, and especially for iron. It was therefore decided to use only particles with $Z < 10$ in the normalization.

The normalization of detector responses obtained by the procedure just described are throught to be accurate to within 2% for most cases. This is determined primarily by the available statistics; consequently, the accuracy is reduced for detectors deep in the stack where there are less particles available for the calibration.

4. Positional and Temporal Nonuniformities. The variations in response of each detector (except the Cerenkov) as a function of position were corrected using a polynomial fit to the response of the detector to relativistic ($C_2' \geq 0.8$) carbon and oxygen nuclei. If we now assume that $M_i({}_\perp\vec{r}_i,t)$ is separable into a time dependent part, $M_i^T(t)$, and a position dependent part, $M_i^P({}_\perp\vec{r}_i)$, we have from equation III.3

$$\langle H_i \cos\theta \rangle_{\theta,\phi,t,C_2' \geq 0.8} = M_i^P \, T_i \langle M_i^T \rangle_t \frac{dL}{dE}(\beta \to 1) \frac{dE}{dx}(\beta \to 1) \tag{A.20}$$

One then obtains

$$M_i^P = \frac{\langle T_i \rangle_{{}_\perp\vec{r}_i, C_2' \geq 0.8} \langle H_i \cos\theta \rangle_{\theta,\phi,t,C_2' \geq 0.8}}{T_i \langle H_i \cos\theta \rangle_{{}_\perp\vec{r}_i,\theta,\phi,t,C_2' \geq 0.8}} \tag{A.21}$$

where

$$1 = \langle M_i^P \rangle_{{}_\perp\vec{r}_i, C_2' \geq 0.8} \tag{A.22}$$

has been assumed. It has also been assumed that the relative fluctuations in M_i^P and T_i are small.

The function M_i^P is approximated by an 11 x 11 polynomial in x_i

and y_i ($x_i = {}_\perp\vec{r}_i \cdot \hat{e}_x$ and $y_i = {}_\perp\vec{r}_i \cdot \hat{e}_y$),

$$M_i^P = \frac{\langle T_i \rangle_{{}_\perp\vec{r}_i,\, c_i' \geq 0.8}}{T_i} \sum_{j,k=1}^{11} {}_i m_{jk} x_i^j y_i^k \tag{A.23}$$

whose coefficients ${}_i m_{jk}$ are determined by a maximum likelihood fit. Since there are few experimental points near the edges of the scintillators, an imaginary border was introduced around each scintillator with dummy data in order to prevent the rapid divergence of M_i^P near the edges. The number of points available for fitting (equation A.23) decreases by a factor of 2.5 as one goes from D1 to D14. Hence the accuracy of the map obtained for a detector decreases with increasing depth of the detector in the stack. The resolution of the fit (equation A.23) to M_i^P thus varies from $\sigma \simeq 0.4\%$ for D1 to $\sigma \simeq 1.5\%$ for D14. Figures A.6 and A.7 present contour diagrams of the response of D1 to relativistic carbon and oxygen nuclei (x minimum units), and the map fit to the data, respectively. The effectiveness of the map in correcting the D1 response may be seen by a comparison of figures A.4 and A.8.

Slow drifts of the responses of the various detectors were discovered by observing the relativistic carbon and oxygen peaks as functions of time. It was found that the fractional deviations of oxygen and carbon peaks from their optimum values were the same, so that there was no need to distinguish the two cases. This meant that there were no (observable) zero offsets involved, and we had only to determine gain variations of the various detectors with time. This is corrected by the factor M_i^T, which is normalized so that

$$\langle M_i^T \rangle = 1 \tag{A.24}$$

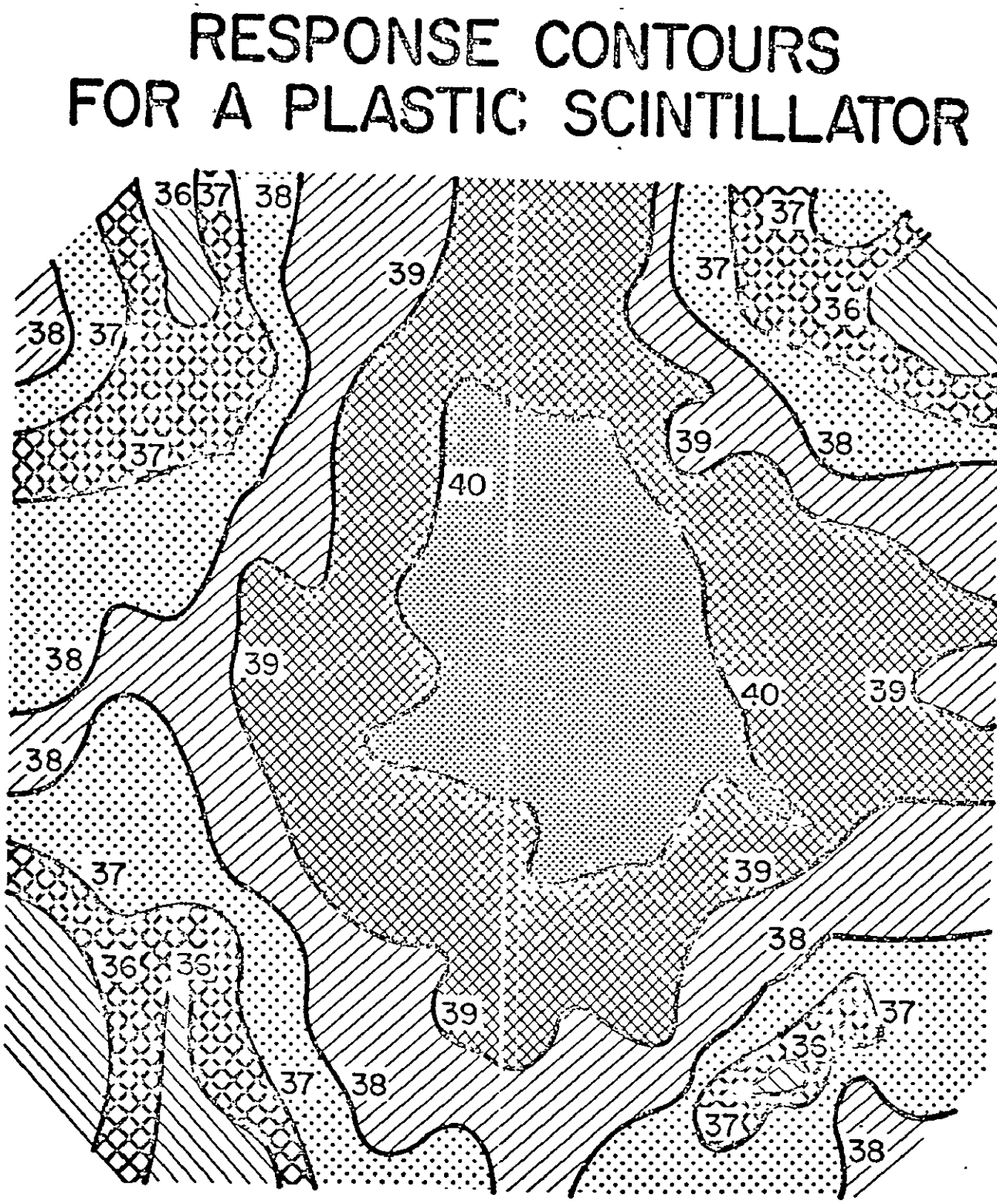

Figure A.6. Contour plot of D1 response to carbon in x minimum units (see fig. A.4 for definition).

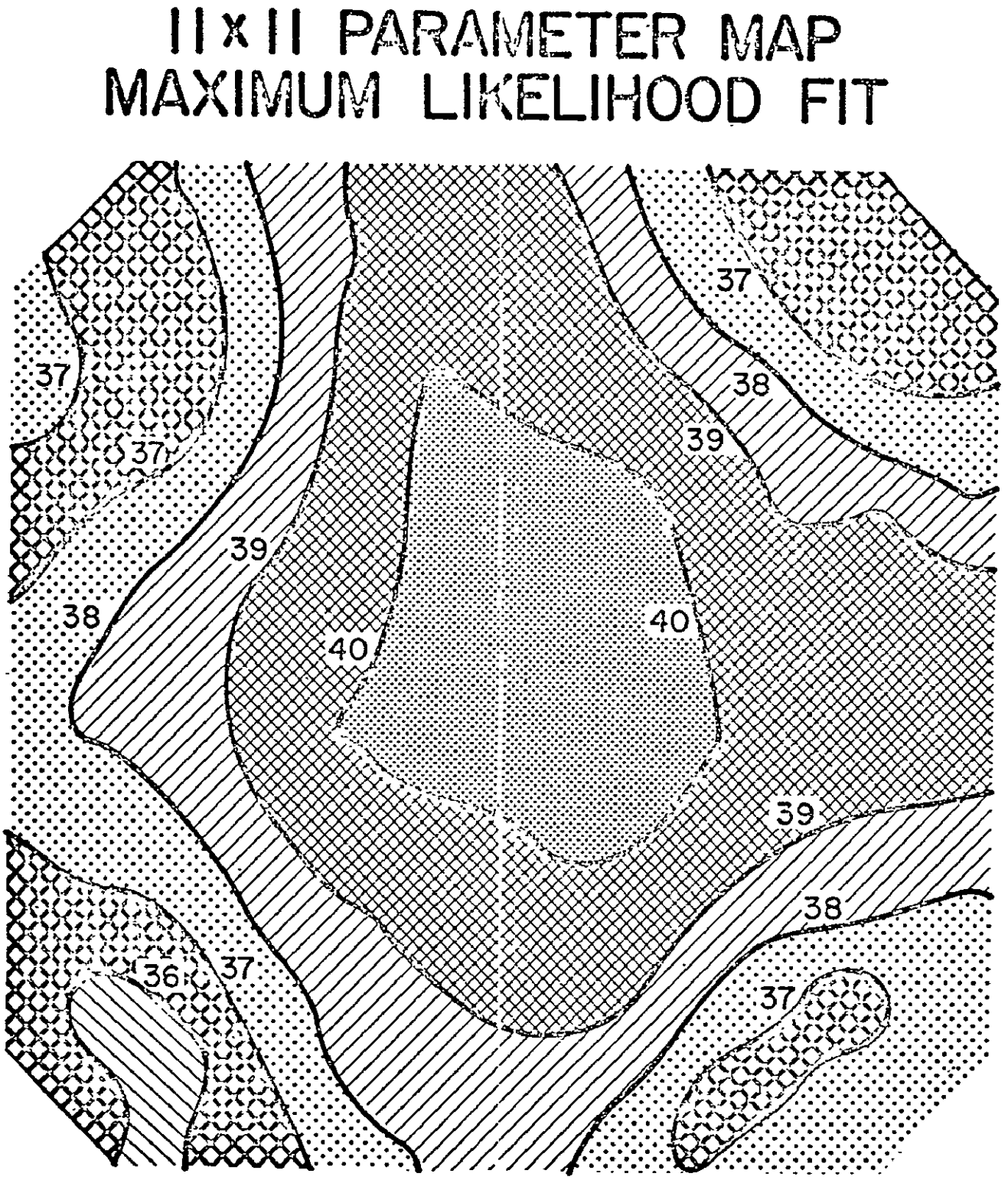

Figure A.7. Contour plot of D1 map, M_1^P, fitted to data of figure A.6.

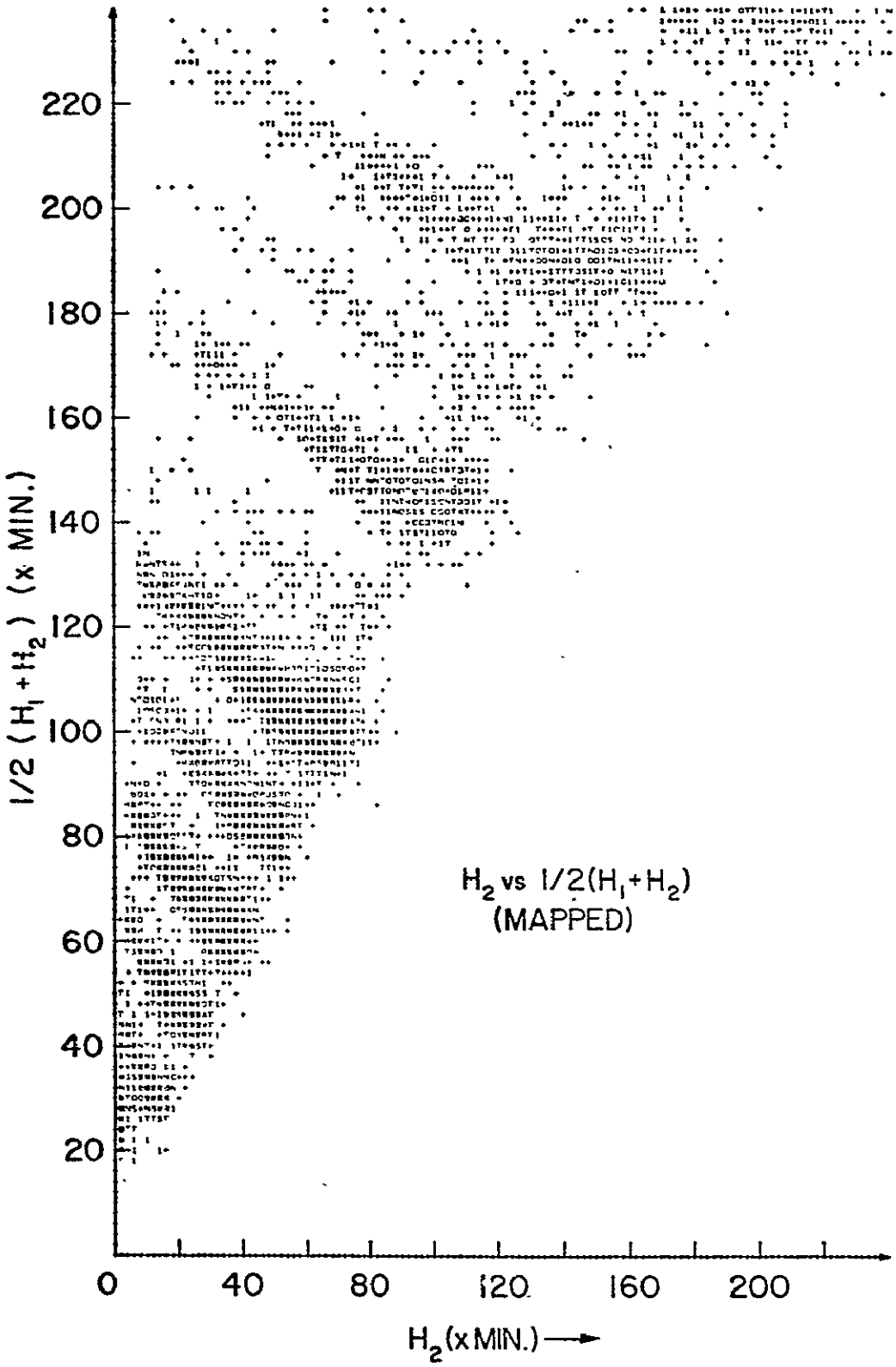

Figure A.5. Cerenkov versus scintillator plot for mapped data. This should be compared to figure A.4.

in order to preserve detector normalizations. The function M_i^T is then determined by

$$M_i^T = \frac{\langle H_i \cos\theta \rangle_{\vec{r}_i, \theta, \phi}}{\langle H_i \cos\theta \rangle_{\vec{r}_i, \theta, \phi, t}} \tag{A.25}$$

The M_i^T are linearly correlated, as is shown in figure A.9 for the case of $M_1^T(t)$ and $M_7^T(t)$. One thus has

$$M_i^T = \alpha_i^T M_1^T + \beta_i^T \tag{A.26}$$

and all the $M_i^T(t)$ are determined in terms of $M_1^T(t)$, the coefficients α_i^T and β_i^T, being determined by least squares fits to data such as that of figure A.9. Using the α_i^T and β_i^T, M_1^T is then approximated by a least squares spline technique (Thompson 1973) using equation A.25 and data from all detectors. The result is shown in figure A.10, together with the corresponding temperature profile in the gondola. There seems to be some correlation between the two. The normalization condition (equation A.24) is apparently not satisfied in this figure since the initial phases of the data reduction were carried out using only a fraction of the available data which was taken near the end of the flight. The normalizations were then all based on this sample of the data, even when the analysis was expanded to include the entire data set. Within experimental error, the function M_i^T was parameterized using a least squares spline fitting routine (Thompson 1973). Since fluctuations in the data were in general very much larger than the effects we were trying to measure, the data supplied to the fitting routine consisted of ~ 10 miniute averages of the actual data.

Because of the statistics involved, we have been able to

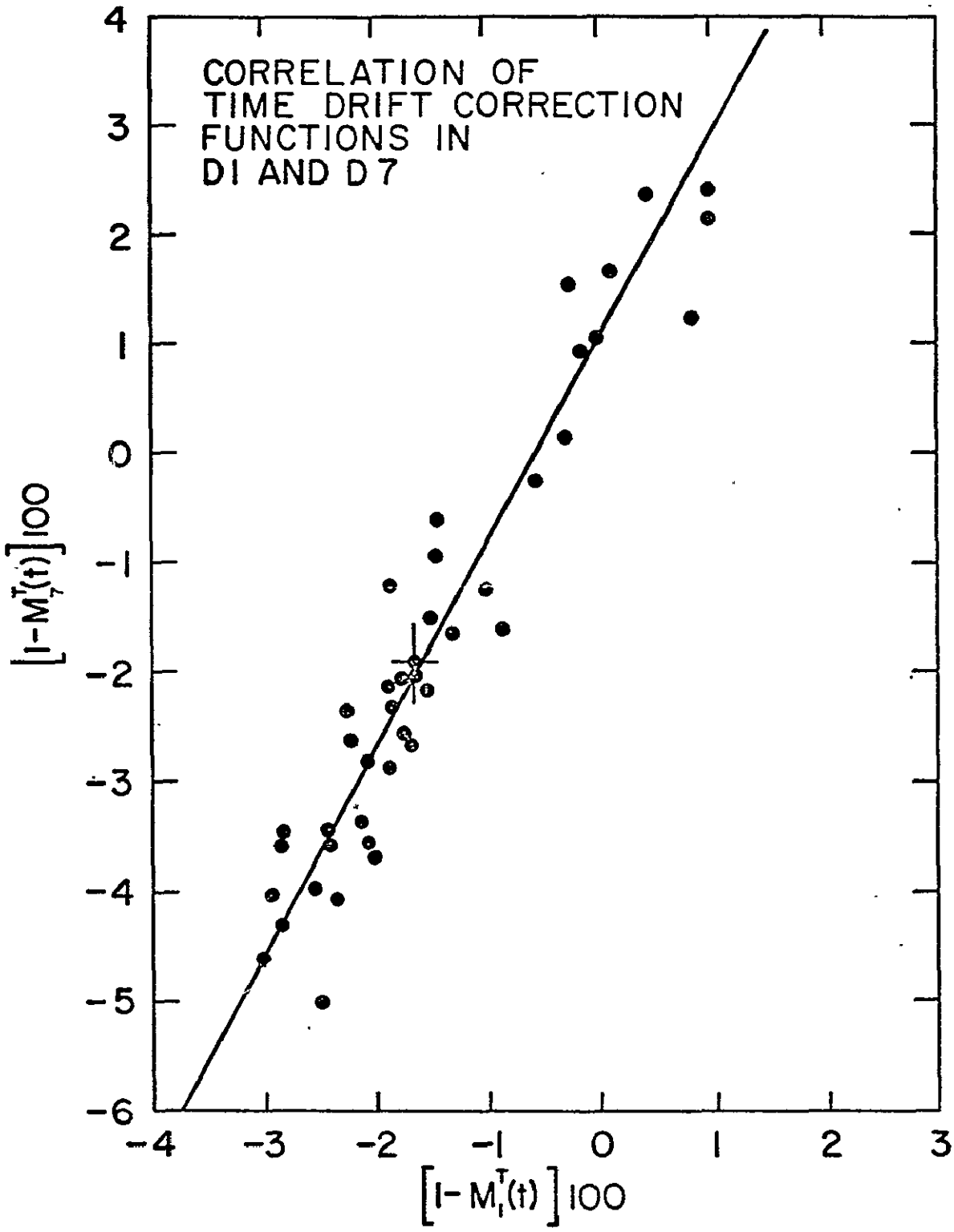

Figure A.9. Linear correlation of drift functions M_1^T and M_7^T.

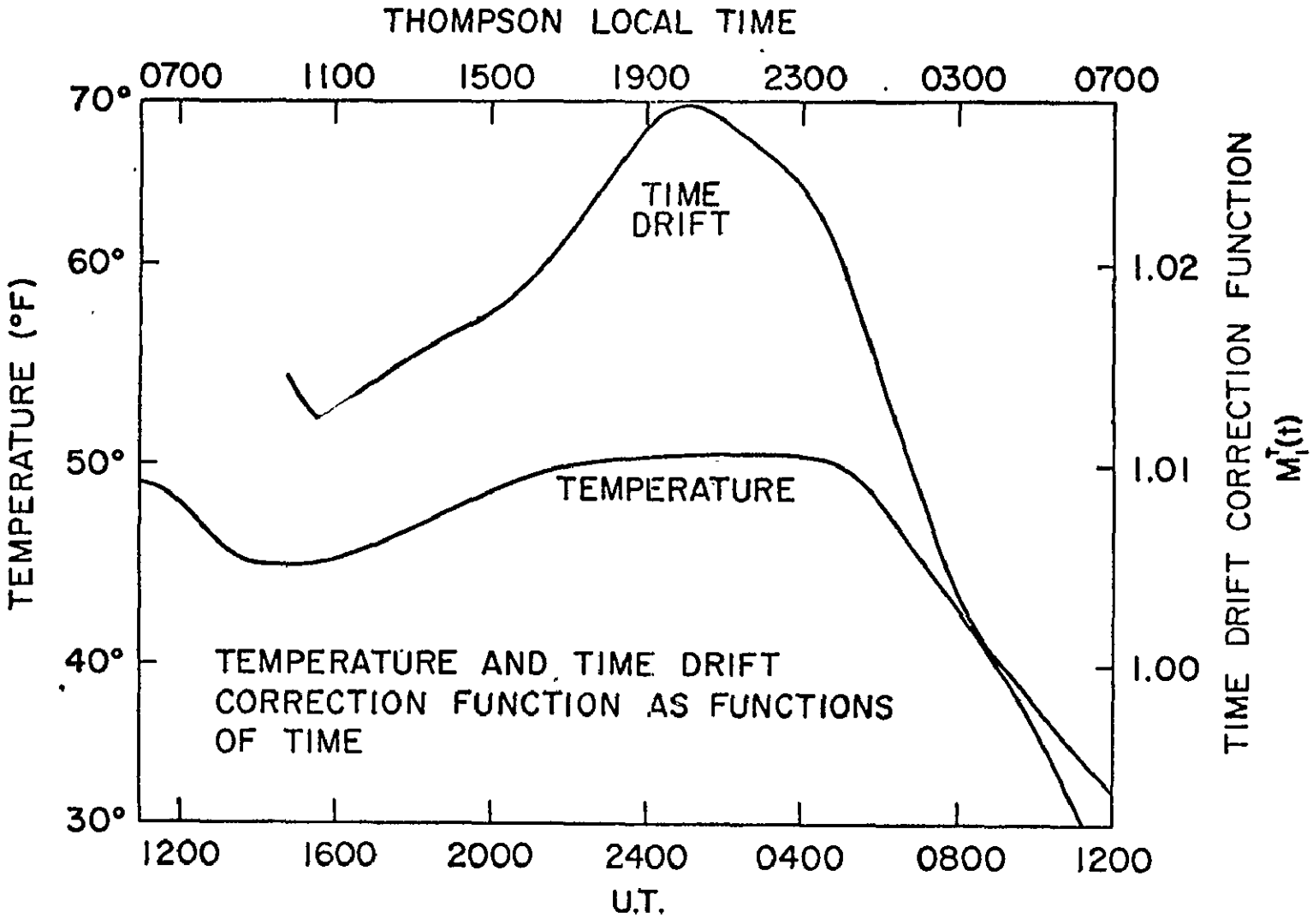

Figure A.10. M_1^T and temperature as functions of time.

accurately determine M_i^T only on time scales greater than about one hour. Although it is conceivable that variations in response on shorter time scales may be present (such as might be expected from a rotation of the gondola in the earth's magnetic field, for instance), we have no way to see or correct for these.

5. Detector Thicknesses. The thickness of each detector was measured on a two inch grid after the flight. The thickness function, T_i, was then approximated by linear interpolations between these points. This correction was necessary because of the large fluctuations in the thickness of certain detectors--up to 10% in extreme cases. As an example, we have listed in table A.2 the thicknesses of the various detectors at each of their four corners. We feel the detector thicknesses are known to $\sim$ 0.1%.

TABLE A.2

Thicknesses of Detectors D4-14 at Corners (in.)

	A	B	C	D
D4	0.388	0.352	0.356	0.377
D5	0.377	0.361	0.355	0.395
D6	0.366	0.361	0.355	0.371
D7	1.344	1.431	1.367	1.338
D8	1.442	1.362	1.366	1.388
D9	1.429	1.345	1.353	1.351
D10	1.356	1.434	1.381	1.371
D11	1.284	1.335	1.348	1.351
D12	1.325	1.376	1.369	1.498
D13	1.387	1.390	1.399	1.615
D14	1.388	1.619	1.395	1.374

APPENDIX B

DEFINITIONS OF SYMBOLS USED IN THIS THESIS

a_{ij} = gain factor for j^{th} gain range of detector i.

$\underline{a}_{ij}$ = gain factor for j^{th} gain range of detector i relative to $(j - 1)^{th}$ gain range.

A = mass number.

A_i = mass deduced from the experimental point (L_i, R_i).

$A_i(\beta)$ = mass as a function of velocity and charge as deduced from the observation of one of the observables i = E, $\frac{dE}{dx}$, R, P or C.

A_s = mass characterizing a standard response curve.

b_{ij} = zero offset for j^{th} gain range of detector i.

$\underline{b}_{ij}$ = zero offset for j^{th} gain range of detector i relative to $(j - 1)^{th}$ gain range.

B = magnetic field intensity.

$B_D \cong 10^{-6}$ gauss = magnetic field intensity characteristic of the galactic disk.

$B_H \cong 10^{-8}$ gauss = magnetic field intensity characteristic of the galactic halo.

$c = 2.998 \times 10^{10}$ cm sec^{-1} = speed of light.

C' = Cerenkov pulse height.

C'_i = value of C' expected if detector i is actually a Cerenkov detector of the same thickness.

${}^{A}_{Z}C^{Atmos}$ = atmospheric correction factor for particles of mass A and charge Z.

${}^{A}_{Z}C^{E}$ = correction factor for energy windows for particles of mass A and charge Z.

${}^{A}_{Z}C^{Inter}$ = correction factor for losses to interactions in the detector (including the gondola) for particles of mass A and charge Z.

A_D = atmospheric propagator matrix (= weighted slab propagator matrix).

LB_D = leaky box propagator matrix.

S_D = slab propagator matrix.

$\hat{e}_x$ = unit vector orthogonal to $\hat{e}_z$ directed towards electronics package.

$\hat{e}_y$ = $\hat{e}_z \times \hat{e}_x$.

$\hat{e}_z$ = unit vector pointing towards zenith.

${}^{A}_{Z}E(\beta) = (\gamma-1)\, mc^2$ = kinetic energy of a particle of mass A, charge Z and velocity β.

${}^{A}_{Z}\left[\frac{dE}{dx}(\beta)\right]$ = ionization energy loss or stopping power of a particle of mass A, charge Z and velocity β.

$f(X)$ = distribution of atmospheric depths.

$\frac{1}{g_{ij}}$ = mean free path for production of species j from spallation of species i.

G = geometrical factor.

$\frac{1}{h_i}$ = mean free path for destruction of species i.

H_i^{cal} = calibration pulse height for detector i as predicted from Cerenkov and D4.

${}^{A}_{Z}H_i(\beta)$ = energy deposited in detector i by particle of mass A, charge Z and velocity β.

H'_{ij} = (integer) pulse height from j^{th} gain range of detector i.

H_R = ratio of light observed in last two detectors to that observed in last detector.

$I(Z) \cong 12.5Z$ eV = average ionization potential of atom of atomic number Z.

J_i = differential energy intensity of species i.

$\overline{J}_i$ = J_i averaged over space.

J_i^P = differential rigidity intensity of species i.

$J_i(X)$ = flux of species i observed under a slab of thickness X.

$J_{ik}(X)$ = flux of species i observed under a slab of thickness X which has undergone exactly k interactions.

K = diffusion coefficient.

$K_D \cong 10^{28}$ cm^2 sec^{-1} = diffusion coefficient characteristic of the galactic disk.

$K_H \cong 10^{29}$ cm^2 sec^{-1} = diffusion coefficient characteristic of the galactic halo.

K_p = rigidity dependent part of diffusion coefficient $K=\beta K_r K_p$.

K_r = radial dependent part of diffusion coefficient $K=\beta K_r K_p$.

${}^A_Z L_i(\beta)$ = total light observed due to particle of mass A, charge Z and velocity β coming to rest in detector i.

${}^A_Z\left\{\frac{dL_i}{dE}(\beta)\right\}$ = differential saturation function for response of scintillator i to a particle of charge Z, mass A and velocity β. Usually taken to be independent of mass and detector number.

m = mass.

$m_e = 9.11 \times 10^{-28}$ g = electron mass.

$m_p = 1.672 \times 10^{-24}$g = proton mass.

x minimum unit = pulse height expected from a relativistic (β=1) particle of unit charge and mass which traverses the detector along the same trajectory as the particle in question.

$M_i(\vec{r}_i,t)$ = factor describing positional and temporal variations in detector response.

$M_i^P(\vec{r}_i)$ = position dependent part of $M_i = M_i^P\, M_i^T$.

$M_i^T(t)$ = time dependent part of $M_i = M_i^P\, M_i^T$.

n = number density.

$\underline{n}$ = index of refraction.

$n_D \cong 1$ atom cm^{-3} = atomic number density characteristic of the galactic disk.

n_i^{CR} = density of cosmic rays of species i

$n_H \cong 10^{-2}$ atom cm^{-3} = atomic number density characteristic of the galactic halo.

${}^{A}_{Z}N_{tot}$ = total number of events observed corresponding to mass A and charge Z.

${}^{A}_{Z}N(A')$ = number of events observed in dA' about A' corresponding to an isotope of actual mass A and charge Z.

$\underline{O}_i$ = (numerical) observed value of the observables i = E, $\frac{dE}{dx}$, R, P or C.

${}^{A}_{Z}O_i(\beta)$ = functional dependence of one of the observables i = E, $\frac{dE}{dx}$, R, P or C on Z, A and β.

p = $\gamma\beta mc$ = momentum.

P_{CRS} = power of the cosmic-ray sources.

${}^{A}_{Z}P(\beta)$ = rigidity of a particle of mass A, charge Z and velocity β.

Q_i = source function for species i (including nuclear interactions).

Q_i^s = source function for species i (excluding nuclear interactions).

$\overline{Q}_i^s$ = Q_i^s averaged over space.

r = heliocentric radius.

$r_c = \frac{\vec{p} \cdot \vec{B}c}{ZeB^2}$ = gyroradius of a particle of momentum, $\vec{p}$, and charge Z, in a magnetic field, B.

$r_e = 2.818 \times 10^{-13}$ cm = classical electron radius.

$r_H \cong 12$ kpc = radius of galactic halo.

$\vec{r}_i$ = positional vector with respect to the geometrical center of detector i.

R_i = range measured from the top of detector i.

${}^{A}_{Z}R(\beta)$ = range of a particle of mass A, charge Z and velocity β.

$\vec{S}$ = surface vector (orthogonal to surface, pointing out).

t = time.

$T_i(\vec{r}_i)$ = thickness of detector i as a function of position.

$V \cong 400$ km sec^{-1} = solar wind velocity.

V = volume

$w \cong 1$ eV cm^{-3} = local cosmic-ray energy density.

$z_D \cong 250$ pc = half thickness of the galactic disk.

Z = charge or atomic number.

α = coefficient

α_i^T = linear correlation coefficient (slope) for M_i^T versus M_1^T.

β = velocity relative to that of light.

β_i^T = zero intercept of linear approximation to M_i^T versus M_1^T.

β_o, β_{oi} = intercept parameter in linear approximation to $A_i(\beta)$.

$\gamma = (1 - \beta^2)^{-1/2}$ = relativistic Lorentz factor.

Δ_{ij} = mass resolution scale factor for contribution to total resolution from resolution of the measurement of the observable i = E, $\frac{dE}{dx}$, R, P or C in a two parameter analysis.

δ = exponent in power law approximation to range-energy relation.

$\delta_{CR} \leqslant 10^{-4}$ = cosmic-ray anisotropy.

η = zero intercept of C_2^1 versus $\frac{1}{2}(H_1 + H_2)$.

θ = zenith angle (with respect to detector normal).

$\lambda_e \cong 5$ g cm^{-2} = mean pathlength traversed by the cosmic rays.

μ = characteristic dimension of a luminescence center.

ν = slope of C_2^1 versus $\frac{1}{2}(H_1 + H_2)$.

ρ = mass density.

σ = resolution in terms of the standard deviation characterizing an (assumed) gaussian distribution.

$\sigma_{H'}$ = resolution of a pulse height analyzer (in channels).

$\sigma_{H_{ij}}$ = energy resolution of the jth gain range of detector i due to pulse height analyzer round off errors.

σ_{ij}^k = partial cross section for production of species j from interaction of species i with species k.

$\sigma_{tot}(A,A_{tar})$ = total inelastic (reaction) cross section for interaction of particles of masses A and A_{tar}.

$\tau_d(j \rightarrow i)$ = mean lifetime against radioactive decay taking species j to species i (* denotes "anything").

ϕ = azimuthal angle (about zenith).

φ_i^{CR} = streaming of cosmic rays of species i.

REFERENCES

Allan, H. R., 1972, Astrophys. Letters 12, 237.

Alvarez, L. W., and Compton, A. H., 1933, Phys. Rev. 43, 835.

Arens, J. F., and Ormes, J. F., 1974, NASA/GSFC document X-661-74-335.

Arnett, W. D., 1969, Ap. J. 157, 1369.

Badhwar, G. D., and Stephens, S. A., 1975, Conference Papers, 14th International Cosmic Ray Conference, Munich, 2, 639.

Baldwin, J. E., 1954, Nature 174, 320.

Barkas, W. H., and Berger, M. J., 1964, NASA document, SP-3013, Washington, D. C.

Bethe, H. A., 1930, Ann. Physik 5, 325.

Bignami, G. F., Fichtel, C. E., Kniffen, D. A., and Thompson, D. J., 1975, Ap. J. 199, 54.

Bloch, F., 1933, Ann. Physik 16, 285.

Bohr, N., 1913, Phil. Mag. 25, 10.

Bradt, H. L., and Peters, B., 1950, Phys. Rev. 80, 943.

Brecher, K., and Burbidge, G., 1971, Comm. Astrophys. Space Phys. 3, 140.

Buffington, A., Orth, C. D., and Smith, L. H., 1973, Conference Papers, 13th International Cosmic Ray Conference, Denver, 1, 225.

Burke, B. F., 1967, I.A.U. Symposium No. 31, Radio Astronomy and the Galactic System, edited by H. Van Voerden, Academic, London, p. 361.

Cameron, A. G. W., 1973, Proc. of Conference on Explosive Nucleosynthesis, Austin, Texas, p. 3.

Casse, M., Goret, P., and Cesarsky, C. J., 1975, 14th International Cosmic Ray Conference, Munich, 2, 646.

Cecchini, S., and Quenby, J. J., 1975, Conference Papers, 14th International Cosmic Ray Conference, Munich, 3, 911.

Colgate, S. A., 1969, Conference Papers, 11th International Cosmic Ray Conference, Budapest, 1, 353.

Dauber, P. M., 1971, "Isotopic Composition of the Primary Cosmic Radiation", edited by P. M. Dauber (Lyngby, Denmark), p. 89.

Dwyer, R., and Meyer, P., 1975, Conference Papers, 14th International Cosmic Ray Conference, Munich, 1, 390.

Dickinson, G. J., and Osborne, J. L., 1975, Conference Papers, 14th International Cosmic Ray Conference, Munich, 2, 665.

Ehrmann, C. H., Fichtel, C. E., Kniffen, D. A., and Ross, D. W., 1967, Nucl. Instr. and Meth. 56, 109.

Fisk, L. A., and Axford, W. I., 1969, J. Geophys. 74, 4973.

Fisk, L. A., 1971, J. Geophys. Res. 76, 221.

Fisk, L. A., 1975, Conference Papers, 14th International Cosmic Ray Conference, Munich, 3, 905.

Frier, P., Lofgren, E. J., Ney, E. P., Oppenheimer, F., Bradt, H. L. and Peters, B., 1948, Phys. Rev. 74, 213.

Garcia-Munoz, M., Mason, G. M., and Simpson, J. A., 1975, Conference Papers, 14th International Cosmic Ray Conference, Munich, 1, 325.

Garcia-Munoz, M., Mason, G. M., and Simpson, J. A., 1975a, Conference Papers, 14th International Cosmic Ray Conference, Munich, 1, 331.

Garcia-Munoz, M., Mason, G. M., and Simpson, J. A., 1975b, Ap. J. 202, 265.

Ginzburg, V. L., and Syrovatskii, S. I., 1964, "The Origin of Cosmic Rays", Permagon Press, New York.

Gleeson, L. J., and Axford, W. I., 1968, Ap. J. 154, 1011.

Gold, T., 1968, Nature 218, 731.

Golden, R. L., Adams, J. H., and Deney, C. L., 1974, Ap. J. 192, 747.

Goldreich, P., and Julian, W., 1969, Ap. J. 157, 869.

Goldstein, M. L., Fisk, L. A., And Ramaty, R., 1970, Phys. Rev. Lett. 25, 832.

Greiner, D. E., 1972, Nuc. Inst. and Meth. 103, 291.

Gunn, J. E., and Ostriker, J. P., 1971, Ap. J. 165, 523.

Hainebach, K. L., Norman, E. B., and Schramm, D. N., 1975, preprint, University of Chicago.

Hayakawa, S., Ito, K., and Terashima, 1958. Proc. Theor. Phys. Suppl. 6, 1.

Hewish, A., Bell, S. J., Pilkington, J. D. H., Scott, P. F., and Collins, R. A., 1968, Nature 217, 709.

Jelley, J., 1958, "Cerenkov Radiation and its Applications", Permagon, New York.

Johnson, T. H., 1933, Phys. Rev. 43, 834.

Jones, F. C., 1970, Phys. Rev. D2, 2787.

Juliusson, E., 1975, Conference Papers, 14th International Cosmic Ray Conference, Munich, 1, 355.

Juliusson, E., and Meyer, P., 1975, Conference Papers, 14th International Cosmic Ray Conference, Munich, 1, 256.

Katz, R., and Kobetich, E. J., 1968, Phys. Rev. 170, 397.

Kobetich, E. J., and Katz, R., 1968, Phys. Rev. 170, 391.

Lezniak, J. A., and Webber, W. R., 1975, Conference Papers, 14th International Cosmic Ray Conference, Munich, 12, 4107.

Lindstrom, P. J., Greiner, D. E., Heckman, H. H., Cork, B., and Bieser, F. S., 1975, Conference Papers, 14th International Cosmic Ray Conference, Munich, 1, 2315.

Lindstrom, P. J., Greiner, D. E., Heckman, H. H., Cork, B., and Bieser, F. S., 1975a, Phys. Rev. Lett. 35, 152.

Meegan, C. A., and Earl, J. A., 1975, Ap. J. 197, 219.

Mewaldt, R. A., Stone, E. C., Vidor, S. B., and Vogt, R. E., 1975, Conference Papers, 14th International Cosmic Ray Conference, Munich, 1, 349.

Meyer, A., and Murray, R. B., 1962, Phys. Rev. 128, 98.

Moraal, H., and Gleeson, L. J., 1975, Conference Papers, 14th International Cosmic Ray Conference, Munich, 12, 4189.

O'Dell, F. W., Shapiro, M. M., Silberberg, R., and Tsao, C. H., 1975, Conference Papers, 14th International Cosmic Ray Conference, Munich, 2, 526.

Ormes, J. F., Fisher, A., Hagen, F., Maehl, R., and Arens, J. F., 1975, Conference Papers, 14th International Cosmic Ray Conference, Munich, 1, 245, to be published.

Owens, A. J., 1975, Conference Papers, 14th International Cosmic Ray Conference, Munich, 2, 684.

Owens, A. J., 1975a, Conference Papers, 14th International Cosmic Ray Conference, Munich, 2, 678.

Pacini, F., 1973, Conference Papers, 13th International Cosmic Ray Conference, Denver, 5, 3285.

Parker, E. N., 1958, Phys. Rev. 110, 1445.

Parker, E. N., 1963, "Interplanetary Dynamical Processes", Interscience Publishers, New York.

Parker, E. N., 1965, Ap. J. 142, 584.

Peters, B., 1963, Pontif. Acad. Sci., Scripta Varia 25, 1.

Peters, B., 1974, Abstracts of Papers, Symposium on Measurements and Interpretation of the Isotopic Composition of Solar and Galactic Cosmic Rays.

Preszler, A. M., Kish, J. C., Lezniak, J. A., Simpson, G., and Webber, W. R., 1975, Conference Papers, 14th International Cosmic Ray Conference, Munich, 12, 4096.

Price, P. B., and Shirk, E. K., 1975, Conference Papers, 14th International Cosmic Ray Conference, Munich, 1, 268.

Ramadurai, S., and Biswar, S., 1972, Astrophys. and Space Science 17, 467.

Reeves, H., 1973, Conference Papers, 13th International Cosmic Ray Conference, Denver, 1, 478.

Renburg, P. U., Measday, D. G., Pepin, M., Schwalker, P., Favier, B., and Richard-Serre, C., 1972, Nuc. Phys. A183, 81.

Rossi, B., 1934, Ric. Sci. 5, 569.

Rossi, B., 1952, "High-Energy Particles", Prentice Hall, New Jersey.

Schein, M., Jesse, W. P., and Wollan, E. O., 1941, Phys. Rev. 59, 615.

Scott, J. S., and Chevalier, R. A., 1975, Ap. J. 197, L5.

Setti, G., and Woltjer, L., 1971, Nature 231, 57.

Shapiro, M. M., and Silberberg, R., 1968, Can. J. Phys. 46, S561.

Shapiro, M. M., and Silberberg, R., 1969, Conference Papers, 11th International Cosmic Ray Conference, Budapest, 1, 485.

Shapiro, M. M., Silberberg, R., and Tsao, C. H., 1973, Conference Papers, 13th International Cosmic Ray Conference, Denver, 1, 578.

Shapiro, M. M., and Silberberg, R., 1975, 14th International Cosmic Ray Conference, Munich, 2, 538.

Silberberg, R., and Tsao, C. H., 1973, Ap. J. Suppl. 25, 315.

Singer, S. F., 1958, "Progress in Elementary Particles and Cosmic Ray Physics", North-Holland, Amsterdam, 4, 205.

3

Sitte, K., 1972, Lett. Nuovo Cim. 5, 1033.

Soutoul, A., Casse, M., and Juliusson, E., 1975, Conference Papers, 14th International Cosmic Ray Conference, Munich, 2, 455.

Sternheimer, R. M., 1952, Phys. Rev. 88, 851.

Sternheimer, R. M., 1960, Phys. Rev. 117, 485.

Sternheimer, R. M., 1961, "Methods of Experimental Physics", (edited by L. C. L. Yuan and C. S. Wu, academic, New York) 5A, 4.

Suh, P. K., 1974, Astron. and Astrophys. 35, 339.

Symon, K. R., 1948, Ph.D. Thesis, Harvard University.

Taylor, C. J., Jentschke, W. K., Remley, M. E., By, F. S. E., and Kruger, P. G., 1951, Phys. Rev. 84, 1034.

Thompson, R. F., 1973, NASA/GSFC document X-692-73-321.

Truran, J. W., and Arnett, W. D., 1970, Ap. J. 160, 181.

Tsao, C. H., Shapiro, M. M., and Silberberg, R., 1973, Conference Papers, 13th International Cosmic Ray Conference, Denver, 1, 107.

Tschalar, C., 1968, Nuc. Instr. and Meth. 61, 141.

Tschalar, C., 1968a, Nuc. Instr. and Meth. 64, 237.

Van Loon, L. G., 1973, Nuovo Cim. 14B, 267.

Webber, W. R., and McDonald, F. B., 1955, Phys. Rev. 100, 1460.

Webber, W. R. and Kish, J., 1972, Nuc. Instr. and Meth. 99, 237.

Webber, W. R., Lezniak, J. A., Kish, J., and Damle, S. V., 1973, Astrophys. and Space Sci. 24, 17.

Webber, W. R., Lezniak, J. A., and Kish, J., 1973a, Nuc. Instr. and Meth. 111, 301.

Wenzel, D. G., 1973, Astrophys. and Space Science 23, 417.

Yiou, F., and Raisbeck, G. M., 1972, Phys. Rev. Lett. 29, 372.